SISSA **ISAS**

SCUOLA INTERNAZIONALE SUPERIORE DI STUDI AVANZATI
INTERNATIONAL SCHOOL FOR ADVANCED STUDIES

General Relativistic Magnetohydrodynamics: fundamental aspects and applications

Thesis submitted for the degree of
Doctor Philosophiæ

CANDIDATE:
Bruno Giacomazzo

SUPERVISORS:
Prof. Luciano Rezzolla

October 2006

Dedicated to my mother Adele
and my brother Mauro.

Table of Contents

Citations to Previously Published Works

Part of the contents of this Thesis has already appeared in the following papers:

Refereed Journals:

- *The Exact Solution of the Riemann Problem in Relativistic Magnetohydrodynamics*
  Giacomazzo B., Rezzolla L., 2006, Journal of Fluid Mechanics, **562**, 223-259.

In Preparation:

- *WhiskyMHD: a new numerical code for general relativistic magnetohydrodynamics.*
  Giacomazzo B., Rezzolla L.
  To be submitted to Phys. Rev. D
- *Gravitational wave emission from the collapse of differentially rotating neutron stars.*
  Giacomazzo B., Rezzolla L., Stergioulas N.
  To be submitted to Phys. Rev. D

Chapter 1

Introduction

In the near future a new window on the Universe will be opened thanks to the birth of gravitational-wave (GW) astronomy.

Gravitational waves are one of the last and more “exotic” predictions of Einstein theory of General relativity that still awaits direct verification. Although some relativists were initially skeptical about their existence (Eddington once said “Gravitational waves propagate at the speed of thought”) in 1993 the Nobel prize for physics was assigned to Hulse and Taylor for their experimental observations and subsequent interpretations of the evolution of the orbit of the binary pulsar PSR 1913+16 [75, 140], the decay of the binary orbit being consistent with angular momentum and energy being carried away from this system by gravitational waves [153].

Gravitational waves will give us the possibility to collect several information that cannot be obtained from direct observations by electromagnetic signals or by neutrinos. During gravitational collapse, for example, electromagnetic radiation interacts strongly with the matter and thus carries information only from lower density regions near the surface of the star, and it is weakened by absorption as it travels to the detector. On the contrary gravitational waves interact only weakly with matter and can travel directly to us from the high-density regions inside the star providing us useful information about those zones.

Measurements of the GW signal may also give direct proof of the existence of black holes [55, 56], will provide new information about the early universe (through the cosmic GW background radiation), will be used to test gravitational theories by the measure of GW speed (predicted to be equal to the light velocity by General Relativity but not by other theories [154]). It may also happen that new sources, not known at the moment, will be discovered as it happened for example with the first observations in the radio and γ frequencies.

It is then easy to understand the importance of the detection of this new kind of signal and why so much effort is being spent by several groups in the world in the development of new GW detectors both on earth and in space. The current progress in the field of GW detection will also require more realistic and detailed predictions about the expected signal in order to benefit of the use of matched filtering analysis techniques which increase considerably the amount of information that can be extracted from the observations. The first generation of ground based interferometric detectors (`LIGO` [96],`VIRGO` [151], `GEO600` [65], `TAMA300` [139]) is indeed beginning the search for GWs and in the next ten years `LIGO` and `VIRGO` will also complete a series of improvements that will increase their sensitivity. A space-based interferometric detector, `LISA` [97], is expected to be launched in 2015 or shortly thereafter. `LISA` is a space-based Michelson interferometer composed by three identical spacecrafts positioned 5 million kilometers apart in an equilateral triangle. The high sensitivity in the range of frequencies between 10^{-4}Hz and 10^{-1}Hz will permit the detection of GW originated from the formation and the coalescence of massive black holes and galactic binaries.

The most promising sources of gravitational waves for the detectors presently in operation are coalescing compact binary systems composed by two neutron stars (NS) or by a NS and a black hole (BH), binary black holes, gravitational collapses (to black-holes or neutron stars) and pulsars. Because all of these involve very compact objects, such as neutron stars and black holes, and strong gravitational fields, it is necessary to solve the full set of Einstein equations without approximations to obtain an accurate prediction on the GW signal.

Given the high non-linearity and complexity of these equations is then necessary to solve them through the use of parallel numerical codes and over the last years several groups in the world started the development of multipurpose numerical codes able to study the sources listed above, even if still not including all the physical process that may be present. One of these, the `Whisky` code [16], was developed to solve the full set of general relativistic hydrodynamics equations in 3 spatial dimensions. It made it possible the computation, for the first time and without approximations, of the GW signal coming from the collapse of uniformly rotating neutron stars [17]. It has also been recently applied to the study of the dynamical barmode instability [14], of the head-on collision of two NS or of a mixed system composed of a NS and a BH [98]. Even if the progress made with this code are increasing our understanding of different astrophysical systems, we are still limited by the use of non-realistic equations of state (even if some work in progress is being done in this direction), by the lack of a treatment of radiative processes and by the absence of magnetic fields, which are known to be present and to have a relevant influence in many situations.

Magnetic fields play, for example, a key role in phenomena like γ-ray bursts (GRB) which are thought to be associated to the collapse of the core of massive magnetized stars [73, 138] (these are the so called "long" GRB) or to the merger of NS [49, 26] (these are the so called "short" GRB), see ref. [103] for a review on GRB. GRB are an example of the importance of doing astrophysical observations in all the possible frequencies and they are also very good candidates for GW [149]. Furthermore it is not possible with the current observations to obtain direct information about the inner parts of the central engine powering the GRB. The electromagnetic signal is in fact emitted from regions far away from the center and so gravitational waves will be the only way to unveil the structure of the central part and to confirm the expected presence of a Kerr black hole. In addition, a coincidence between a GW signal and a γ-ray signal would be of great help with data analysis techniques in increasing significantly the signal to noise ratio (SNR) of the detectors in this case [54, 79].

Magnetic fields can also have an effect on the gravitational waves emitted by other sources affecting both the frequencies and the amplitude of the signals. It has been claimed that they can lower the amplitude even by an order of 10% in supernova core collapse [87] or that they can even suppress the r-mode instability in neutron stars [121, 102] or considerably lower the amplitude of the GW signal generated by this instability [119, 120].

In order to increase our theoretical understanding of all these objects we have developed `WhiskyMHD`, a new numerical code that solves the equations of general relativistic magnetohydrodynamics in three spatial dimensions on a generic and time-varying spacetime. Like the `Whisky` code, it is conceived as an astrophysical laboratory in which to investigate the physics of compact objects in presence of magnetic fields. Our main aim is then to extend all the work done so far with the `Whisky` code to include the effects of magnetic fields and also to study interesting astrophysical scenario that cannot be simulated with `Whisky`, such as the sources of γ-ray bursts in connection with gravitational waves emission.

This thesis is essentially composed of two parts. In the first we concentrate on the use of the `Whisky` code to study the collapse of differentially rotating neutron stars without magnetic fields. Differentially rotating NS are thought to be the results of the mergers of binary neutron stars and they have been proposed as candidates for short γ-ray burst. Here we start the study without the presence of a magnetic field in order to have a first description of the dynamics and of the gravitational waves emitted by them. We recall that this problem, *i.e.* the study of the GW emission from the collapse to BH of differentially rotating NS, has not been yet discussed in the literature and the results presented here represent the first steps in the investigation of this process. In particular, in Chapter 2 we describe the formulation adopted to solve Einstein equations in both the `Whisky` and the `WhiskyMHD` codes. In Chapter 3 we introduce the `Whisky` code and we give details about the equations of general relativistic hydrodynamics (GRHD) and their numerical implementation in a conservative formalism. Then in Chapter 4 we present new results from the collapse of strongly differentially rotating neutron-stars. We consider models with different values of J/M^2, where J is the angular momentum and M the mass of the system. We find that a black-hole forms only if $J/M^2 < 1$ and that the dynamics looks similar to what already observed for uniformly rotating stars. We studied the final fate of a star with $J/M^2 > 1$ when its collapse is caused by a large pressure depletion and we observe a very different dynamics with the development of nonaxisymmetric instabilities and the formation of a stable, differentially rotating NS. In all the cases we present also the gravitational wave signal emitted from these sources.

In the second part we focus on the development of our `WhiskyMHD` code. In Chapter 6 we describe the equations of general relativistic magnetohydrodynamics (GRMHD) and the formulation used to rewrite the system in a conservative form. The use of this formulation is particularly useful because it permits to extend to GRMHD the use of conservative schemes, such as the high resolution shock capturing methods, already used in GRHD codes like `Whisky`. Being these methods based on the solutions of Riemann problems, in Chapter 5 we discuss the procedure for the exact solution of the Riemann problem in special relativistic magnetohydrodynamics. We consider both initial states leading to a set of only three waves analogous to the ones in relativistic hydrodynamics, as well as generic initial states leading to the full set of seven MHD waves. This solution represents as important step towards a better understanding of the complex dynamics of nonlinear waves in relativistic MHD. Because of its generality, the solution presented here is now becoming a standard tool used by different groups in the world to test both special and general relativistic MHD codes. In Chapter 7 we give the details of our new numerical code `WhiskyMHD` and the results of the tests with some preliminary applications to the study of the oscillations of magnetized neutron stars. Finally, Chapter 8 will collect our conclusions and the prospects of future work.

Notation

We use a spacelike signature $(-,+,+,+)$ and a system of units in which $c = G = M_\odot = 1$. Greek indices are taken to run from 0 to 3, Latin indices from 1 to 3 and we adopt the standard convention for the summation over repeated indices. Finally we indicate 3-vectors with an arrow and use bold letters to denote 4-vectors and tensors.

Computational resources

All the numerical computations discussed in this thesis were performed on clusters *Albert100* and *Albert2* at the Physics Department of the University of Parma (Italy), on the cluster *CLX* at CINECA (Bologna, Italy) and on the cluster *Peyote* at AEI (Golm, Germany).

Chapter 2

Spacetime formulation

2.1 Introduction

In this chapter we describe the formulation adopted for the numerical solution of Einstein equations:

$$G_{\mu\nu} = R_{\mu\nu} - \frac{1}{2} g_{\mu\nu} R = 8\pi T_{\mu\nu} \ , \tag{2.1}$$

where $T_{\mu\nu}$ is the *stress energy tensor*, $G_{\mu\nu}$ is the *Einstein tensor*, $R \equiv R^{\mu}_{\mu}$ is the *Ricci scalar*, $R_{\mu\nu} \equiv R^{\rho}_{\mu\rho\nu}$ is the *Ricci tensor*,

$$R^{\sigma}_{\mu\rho\nu} \equiv \partial_\rho \Gamma^{\sigma}_{\mu\nu} - \partial_\nu \Gamma^{\sigma}_{\mu\rho} + \Gamma^{\sigma}_{\tau\rho}\Gamma^{\tau}_{\mu\nu} - \Gamma^{\sigma}_{\tau\nu}\Gamma^{\tau}_{\mu\rho} \ , \tag{2.2}$$

is the *Riemann tensor* and

$$\Gamma^{\sigma}_{\mu\rho} \equiv \frac{1}{2} g^{\sigma\tau} \left(\partial_\mu g_{\rho\tau} + \partial_\rho g_{\mu\tau} - \partial_\tau g_{\mu\rho} \right) \ , \tag{2.3}$$

are the *Christoffel symbols* expressed in terms of the metric $g_{\mu\nu}$. All these objects are 4-dimensional, that is they are defined on the 4-dimensional spacetime manifold $\mathcal{M}$.

The ability to perform long-term numerical simulations of self-gravitating systems in general relativity strongly depends on the formulation adopted for the Einstein equations (2.1).

Over the years, the standard approach has been mainly based upon the "3+1" formulation of the field equations, which was first introduced by Arnowitt, Deser and Misner (ADM) [13]. In the following section we will give an outline of this formalism, while in Section 2.3 we will present a better formulation which is implemented in the codes we use.

2.2 The Arnowitt Deser Misner "3+1" formalism

According to the ADM formalism, the spacetime manifold $\mathcal{M}$ is assumed to be globally hyperbolic and to admit a foliation by 3-dimensional spacelike hypersurfaces Σ_t parameterized by the parameter $t \in \mathcal{R}$: $\mathcal{M} = \mathcal{R} \times \Sigma_t$. The future-pointing 4-vector $\mathbf{n}$ orthonormal to Σ_t is then proportional to the gradient of t: $\mathbf{n} = -\alpha \boldsymbol{\nabla} t$, where α is chosen following the normalization $\mathbf{n} \cdot \mathbf{n} = -1$. Introducing a coordinate basis $\{\mathbf{e}_{(\mu)}\} = \{\mathbf{e}_{(0)}, \mathbf{e}_{(i)}\}$

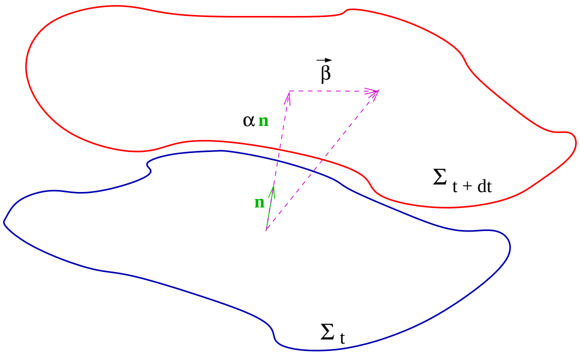

Figure 2.1 The foliation of spacetime according to the "3 + 1" formalism.

of 4-vectors and choosing the normalization of the timelike coordinate basis 4-vector $\mathbf{e}_{(0)}$ to be $\mathbf{e}_{(0)} \cdot \boldsymbol{\nabla} t = 1$, with the other three basis 4-vectors to be spacelike (*i.e.* tangent to the hypersurface: $\mathbf{n} \cdot \mathbf{e}_{(i)} = 0 \quad \forall i$), then the decomposition of $\mathbf{n}$ into the basis $\{\mathbf{e}_{(\mu)}\}$ is

$$\mathbf{n} = \frac{\mathbf{e}_{(0)}}{\alpha} + \frac{\boldsymbol{\beta}}{\alpha} \ , \tag{2.4}$$

where $\boldsymbol{\beta} = \beta^i \mathbf{e}_{(i)}$ is a purely spatial vector called the *shift* vector, since it describes how the spatial coordinates shift when moving from a slice Σ_t to another $\Sigma_{t'}$. The function α is called *lapse* and describes the rate of advance of time along the timelike unit-vector $\mathbf{n}$ normal to a spacelike hypersurface Σ_t (see figure 2.1). Defining $\gamma_{\mu\nu} \equiv g_{\mu\nu} + n_\mu n_\nu$ to be the spatial part of the 4-metric, so that $\boldsymbol{\gamma}$ is the projector orthogonal to $\mathbf{n}$ (*i.e.* $\boldsymbol{\gamma} \cdot \mathbf{n} = 0$) and γ_{ij} is the 3-metric of the hypersurfaces, the line element in the 3+1 splitting reads

$$\mathrm{d}s^2 = -(\alpha^2 - \beta^i \beta_i)\mathrm{d}t^2 + 2\beta_i \mathrm{d}x^i \mathrm{d}t + \gamma_{ij}\mathrm{d}x^i \mathrm{d}x^j \ . \tag{2.5}$$

The original ADM formulation [13] casts the Einstein equations into a first-order-in-time second-order-in-space quasi-linear system of equations [124] and a set of elliptic equations (the *constraint equations*). The dependent variables for which there is a time evolution are the 3-metric γ_{ij} and the extrinsic curvature

$$K_{ij} \equiv -\gamma_i^k \gamma_j^l \nabla_k n_l \ , \tag{2.6}$$

where ∇_i denotes the covariant derivative with respect to the 3-metric γ_{ij}. By construction, the extrinsic curvature is symmetric and purely spatial. The extrinsic curvature describes the embedding of the 3-dimensional spacelike hypersurfaces Σ_t in the 4-dimensional manifold $\mathcal{M}$. The first-order evolution equations are then given by

$$\mathcal{D}_t \gamma_{ij} = -2\alpha K_{ij} \ , \tag{2.7}$$

$$\mathcal{D}_t K_{ij} = -\nabla_i \nabla_j \alpha + \alpha \left[R_{ij} + K\ K_{ij} - 2K_{im}K_j^m - 8\pi \left(S_{ij} - \frac{1}{2}\gamma_{ij} S \right) - 4\pi\rho\gamma_{ij} \right] . \tag{2.8}$$

Here, $\mathcal{D}_t \equiv \partial_t - \mathcal{L}_{\boldsymbol{\beta}}$, $\mathcal{L}_{\boldsymbol{\beta}}$ is the Lie derivative[1] with respect to the vector $\boldsymbol{\beta}$, R_{ij} is the Ricci tensor of the 3-metric, $K \equiv \gamma^{ij}K_{ij}$ is the trace of the extrinsic curvature, $\rho \equiv n_\mu n_\nu T^{\mu\nu}$ is the total energy density as measured by a normal observer (*i.e.* the projection of the stress-energy tensor on the normal to the spatial hypersurface Σ_t), $S_{ij} \equiv \gamma_{i\mu}\gamma_{j\nu}T^{\mu\nu}$ is the projection of the stress-energy tensor onto the spacelike hypersurfaces and $S \equiv \gamma^{ij}S_{ij}$ (for a more detailed discussion, see ref. [162]). Equation (2.7) illustrates the intuitive interpretation of the extrinsic curvature as the "time derivative" of the spatial metric γ_{ij}. The spatial metric on two different slices may still differ by a coordinate transformation, of course. In this intuitive framework, equation (2.8) represents the "acceleration", *i.e.* the variation of the variations of the spatial metric.

In addition to the evolution equations, the Einstein equations also provide four constraint equations to be satisfied on each spacelike hypersurface. The first of these is the Hamiltonian constraint equation

$$R + K^2 - K_{ij}K^{ij} - 16\pi\rho = 0 \ , \tag{2.9}$$

where R denotes the Ricci scalar of the 3-metric. The other three constraint equations are the momentum constraint equations

$$\nabla_j K^{ij} - \gamma^{ij}\nabla_j K - 8\pi S^i = 0 \ , \tag{2.10}$$

where $S^i \equiv -\gamma^{i\mu}n^\nu T_{\mu\nu}$ is the momentum density as measured by an observer moving orthogonally to the spacelike hypersurfaces.

The system of equations (2.7)–(2.10) is not closed; in fact, we are free to specify additional *gauge* conditions to determine the coordinate system. These are usually imposed as equations on the lapse and the shift.

Finally, we give here the expressions of the total mass and of the total angular momentum as measured at infinity in an asymptotically-flat spacetime

$$\begin{aligned} M_{\rm ADM} &\equiv \frac{1}{16\pi}\int_{r=\infty} \sqrt{\gamma}\gamma^{im}\gamma^{jl}(\gamma_{ml,j} - \gamma_{jl,m})d^2\mathcal{S}_i \ , & (2.11)\\ (J_{\rm ADM})_i &\equiv \frac{1}{8\pi}\varepsilon_{ij}{}^{k}\int_{r=\infty} x^j K^m_k d^2\mathcal{S}_m \ , & (2.12) \end{aligned}$$

where $\mathcal{S}$ is a closed surface in an asymptotically-flat region and $\varepsilon_{ij}{}^{k}$ is the flat-space Levi-Civita tensor.

2.3 Conformal transverse traceless formulation

The ADM formalism was widely used in the past but it soon revealed to lack the stability properties necessary for long-term numerical simulations. At the end of the last

---

[1] For an arbitrary tensor $T^{s_1,\dots,s_u}_{t_1,\dots,t_w}$ and an arbitrary vector $\mathbf{v}$ the Lie derivative is defined as

$$\mathcal{L}_{\mathbf{v}}T^{s_1,\dots,s_u}_{t_1,\dots,t_w} \equiv v^r\nabla_r T^{s_1,\dots,s_u}_{t_1,\dots,t_w} - \sum_{n=1}^{u} T^{s_1,\dots,r,\dots,s_u}_{t_1,\dots,t_w}\nabla_r v^{s_n} + \sum_{n=1}^{w} T^{s_1,\dots,s_u}_{t_1,\dots,r,\dots,t_w}\nabla_{t_n} v^r \ .$$

century a new scheme based on a conformal traceless reformulation of the ADM system was developed by Nakamura, Oohara and Kojima [114] and successively improved in refs. [130, 24]. Its stability properties make this formulation the most used in numerical relativity and it is commonly known with the name of BSSN (or BSSNOK).

2.3.1 Evolution of the field equations

Here we briefly introduce the set of equations we use to solve Einstein equations (2.1), but more details on how this formulation is actually implemented in our numerical codes can be found in refs. [6, 4].

The conformal traceless reformulations of the ADM equations (2.7)–(2.10) make use of a conformal decomposition of the 3-metric and of the trace-free part of the extrinsic curvature. Here we follow the presentation made in ref. [6].

The conformal 3-metric $\tilde{\gamma}_{ij}$ is defined as

$$\tilde{\gamma}_{ij} \equiv e^{-4\phi}\gamma_{ij} \ , \tag{2.13}$$

with the conformal factor chosen to be

$$e^{4\phi} = \gamma^{1/3} \equiv \det(\gamma_{ij})^{1/3} \ . \tag{2.14}$$

In this way the determinant of $\tilde{\gamma}_{ij}$ is unity. The trace-free part of the extrinsic curvature K_{ij}, defined by

$$A_{ij} \equiv K_{ij} - \frac{1}{3}\gamma_{ij}K \ , \tag{2.15}$$

is also conformally decomposed:

$$\tilde{A}_{ij} = e^{-4\phi}A_{ij} \ . \tag{2.16}$$

The evolution equations for the conformal 3-metric $\tilde{\gamma}_{\ ij}$ and the related conformal factor ϕ are then written as

$$\begin{aligned} \mathcal{D}_t\tilde{\gamma}_{ij} &= -2\alpha\tilde{A}_{ij} \ , & (2.17)\\ \mathcal{D}_t\phi &= -\frac{1}{6}\alpha K \ . & (2.18)\end{aligned}$$

The evolution equation for the trace of the extrinsic curvature K can be found to be

$$\mathcal{D}_tK = -\gamma^{ij}\nabla_i\nabla_j\alpha + \alpha\left[\tilde{A}_{ij}\tilde{A}^{ij} + \frac{1}{3}K^2 + \frac{1}{2}(\rho + S)\right] \ , \tag{2.19}$$

where the Hamiltonian constraint was used to eliminate the Ricci scalar. For the evolution equation of the trace-free extrinsic curvature $\tilde{A}_{ij}$ there are many possibilities. A trivial manipulation of equation (2.8) yields:

$$\mathcal{D}_t\tilde{A}_{ij} = e^{-4\phi}\left[-\nabla_i\nabla_j\alpha + \alpha\left(R_{ij} - S_{ij}\right)\right]^{\rm TF} + \alpha\left(K\tilde{A}_{ij} - 2\tilde{A}_{il}\tilde{A}^l_j\right) \ , \tag{2.20}$$

where $[T_{ij}]^{\rm TF}$ refers to the trace-free part of a 3-dimensional second-rank tensor T_{ij}, *i.e.*, $[T_{ij}]^{\rm TF} \equiv T_{ij} - \gamma_{ij}T^k_k/3$. Note that, as shown in refs. [130, 24], there are many ways to write several of the terms of (2.20), especially those involving the Ricci tensor; the expression which proved more convenient for numerical simulations consists in conformally decomposing the Ricci tensor as

$$R_{ij} = \tilde{R}_{ij} + R^{\phi}_{ij} \ , \tag{2.21}$$

where the "conformal-factor" part R^{ϕ}_{ij} is given directly by straightforward computation of the spatial derivatives of ϕ:

$$R^{\phi}_{ij} \ = \ -2\tilde{\nabla}_i\tilde{\nabla}_j\phi - 2\tilde{\gamma}_{ij}\tilde{\nabla}^l\tilde{\nabla}_l\phi + 4\tilde{\nabla}_i\phi \ \tilde{\nabla}_j\phi - 4\tilde{\gamma}_{ij}\tilde{\nabla}^l\phi \ \tilde{\nabla}_l\phi \ , \tag{2.22}$$

while the "conformal" part $\tilde{R}_{ij}$ can be computed in the standard way from the conformal 3-metric $\tilde{\gamma}_{ij}$. To simplify the notation, it is convenient to define what Baumgarte *et al.* [24] call the "conformal connection functions"

$$\tilde{\Gamma}^i \equiv \tilde{\gamma}^{jk}\tilde{\Gamma}^i_{jk} = -\partial_j\tilde{\gamma}^{ij} \ , \tag{2.23}$$

where the last equality holds if the determinant of the conformal 3-metric $\tilde{\gamma}$ is unity (note that this may well not be true in numerical simulations). Using the conformal connection function, the Ricci tensor can be written as[2]

$$\tilde{R}_{ij} \ = \ -\frac{1}{2}\tilde{\gamma}^{lm}\partial_l\partial_m\tilde{\gamma}_{ij} + \tilde{\gamma}_{k(i}\partial_{j)}\tilde{\Gamma}^k + \tilde{\Gamma}^k\tilde{\Gamma}_{(ij)k} + \tilde{\gamma}^{lm}\left(2\tilde{\Gamma}^k_{l(i}\tilde{\Gamma}_{j)km} + \tilde{\Gamma}^k_{im}\tilde{\Gamma}_{klj}\right) \ .$$

Also in this case there are several different choices of how the terms involving the conformal connection functions $\tilde{\Gamma}^i$ are computed. A straightforward computation based on the Christoffel symbols could be used (as in standard ADM formulations), but this approach leads to derivatives of the 3-metric in no particular elliptic form. Alcubierre *et al.* [6] found that if the $\tilde{\Gamma}^i$ are promoted to independent variables, then the expression for the Ricci tensor retains an elliptic character, which is positive in the direction of bringing the system a step closer to being hyperbolic. The price to pay is that in this case one must evolve three additional quantities. This has, however, net numerical advantages, which will be discussed below.

Following this argument of promoting the $\tilde{\Gamma}^i$ to independent variables, it is straightforward to derive their evolution equation

$$\partial_t\tilde{\Gamma}^i \ = \ -\partial_j\left(2\alpha\tilde{A}^{ij} - 2\tilde{\gamma}^{m(j}\partial_m\beta^{i)} + \frac{2}{3}\tilde{\gamma}^{ij}\partial_l\beta^l + \beta^l\partial_l\tilde{\gamma}^{ij}\right) \ . \tag{2.24}$$

Here too, there are different possibilities for writing these evolution equations; as pointed out in ref. [24] it turns out that the above choice leads to an unstable system. Alcubierre *et al.* [6] found that a better choice can be obtained by eliminating the divergence of $\tilde{A}^{ij}$ with the help of the momentum constraint

$$\begin{aligned}\partial_t\tilde{\Gamma}^i \ = \ & -2\tilde{A}^{ij}\partial_j\alpha + 2\alpha\left(\tilde{\Gamma}^i_{jk}\tilde{A}^{kj} - \frac{2}{3}\tilde{\gamma}^{ij}\partial_j K - \tilde{\gamma}^{ij}S_j + 6\tilde{A}^{ij}\partial_j\phi\right) \\ & -\partial_j\left(\beta^l\partial_l\tilde{\gamma}^{ij} - 2\tilde{\gamma}^{m(j}\partial_m\beta^{i)} + \frac{2}{3}\tilde{\gamma}^{ij}\partial_l\beta^l\right) \ .\end{aligned} \tag{2.25}$$

---

[2] We define $T_{(ij)}$ as the symmetrized part of the tensor T_{ij}.

With this reformulation, in addition to the evolution equations for the conformal 3-metric $\tilde{\gamma}_{ij}$ (2.17) and the conformal traceless extrinsic curvature variables $\tilde{A}_{ij}$ (2.20), there are evolution equations for the conformal factor ϕ (2.18) and the trace K of the extrinsic curvature (2.19). If the $\tilde{\Gamma}^i$ are promoted to the status of fundamental variables, they can be evolved with (2.25). We note that, although the final first-order-in-time and second-order-in-space system for the 17 evolved variables $\left\{\phi, K, \tilde{\gamma}_{ij}, \tilde{A}_{ij}, \tilde{\Gamma}^i\right\}$ is not in any immediate sense hyperbolic, there is evidence showing that the formulation is at least equivalent to a hyperbolic system [128, 28, 113].

In references [6, 3] the improved properties of this conformal traceless formulation of the Einstein equations were compared to the ADM system. In particular, in ref. [6] a number of strongly gravitating systems were analyzed numerically with convergent *high-resolution shock-capturing* methods with *total-variation-diminishing* schemes using the equations described in ref. [59]. These included weak and strong gravitational waves, black holes, boson stars and relativistic stars. The results showed that this treatment led to a numerical evolution of the various strongly gravitating systems which did not show signs of numerical instabilities for sufficiently long times. However, it was also found that the conformal traceless formulation requires grid resolutions higher than the ones needed in the ADM formulation to achieve the same accuracy, when the foliation is made using the "K-driver" approach discussed in ref. [19]. Because in long-term evolutions a small error growth-rate is the most desirable property, we have adopted the conformal traceless formulation as our standard form for the evolution of the field equations.

In conclusion of this section, we report the expressions (2.11) and (2.12) of the total mass and of the total angular momentum as measured in an asymptotically-flat spacetime, expressed in the variables introduced in this formulation and transformed, using the Gauss law, in volume integrals, which are better suited to Cartesian numerical computations [159]:

$$M = \int_V \left[e^{5\phi}\left(\rho + \frac{1}{16\pi}\tilde{A}_{ij}\tilde{A}^{ij} - \frac{1}{24\pi}K^2\right) - \frac{1}{16\pi}\tilde{\Gamma}^{ijk}\tilde{\Gamma}_{jik} + \frac{1-e^{\phi}}{16\pi}\tilde{R}\right] d^3x \ , \quad (2.26)$$

$$J_i = \varepsilon_{ij}{}^{k}\int_V \left(\frac{1}{8\pi}\tilde{A}^j_k + x^j S_k \quad + \frac{1}{12\pi}x^j K_{,k} - \frac{1}{16\pi}x^j \tilde{\gamma}^{lm}{}_{,k}\tilde{A}_{lm}\right) e^{6\phi} d^3x \ . \quad (2.27)$$

2.3.2 Gauge choices

Here we give the details about the specific gauges used in the simulations reported in Chapter 4. In particular, we have used hyperbolic K-driver slicing conditions of the form

$$(\partial_t - \beta^i\partial_i)\alpha = -f(\alpha)\,\alpha^2(K - K_0) \ , \quad (2.28)$$

with $f(\alpha) > 0$ and $K_0 \equiv K(t = 0)$. This is a generalization of many well-known slicing conditions. For example, setting $f = 1$ we recover the "harmonic" slicing condition, while, by setting $f = q/\alpha$, with q an integer, we recover the generalized "1+log" slicing condition [29]. In particular, all of the simulations discussed in this thesis are done using condition (2.28) with $f = 2/\alpha$. This choice has been made mostly because of its computational efficiency, but we are aware that "gauge pathologies" could develop with the "1+log" slicings [2, 8].

As for the spatial-gauge, we use one of the "Gamma-driver" shift conditions proposed in ref. [7] (see also ref. [4]), that essentially act so as to drive the $\tilde{\Gamma}^i$ to be constant.

In this respect, the "Gamma-driver" shift conditions are similar to the "Gamma-freezing" condition $\partial_t \tilde{\Gamma}^k = 0$, which, in turn, is closely related to the well-known minimal distortion shift condition [136]. The differences between these two conditions involve the Christoffel symbols and, while the minimal distortion condition is covariant, the Gamma-freezing condition is not.

All of the results reported here have been obtained using the hyperbolic Gamma-driver condition,

$$\partial_t^2 \beta^i = F\, \partial_t \tilde{\Gamma}^i - \eta\, \partial_t \beta^i \ , \tag{2.29}$$

where F and η are, in general, positive functions of space and time. For the hyperbolic Gamma-driver conditions it is crucial to add a dissipation term with coefficient η to avoid strong oscillations in the shift. Experience has shown that by tuning the value of this dissipation coefficient it is possible to almost freeze the evolution of the system at late times. We typically choose $F = 3/4$ and $\eta = 3$ and do not vary them in time.

Chapter 3

The `Whisky` code

3.1 Introduction

As already pointed out in Chapter 1, in order to study the dynamics of compact objects, such as the collapse of neutron stars, and to accurately extract the gravitational wave signal emitted from different astrophysical sources, several European institutions (SISSA, AEI, University of Thessaloniki, University of Valencia) worked together to develop the `Whisky` code.

The `Whisky` code [15] solves the general relativistic hydrodynamics equations on a three dimensional (3D) numerical grid with Cartesian coordinates. The code makes use of the `Cactus` framework (see ref. [32] for details), developed at the Albert Einstein Institute (Golm, Germany) and at the Louisiana State University (Baton Rouge, USA). The `Cactus` code provides high-level facilities such as parallelization, input/output, portability on different platforms and several evolution schemes to solve general systems of partial differential equations. Clearly, special attention is dedicated to the solution of the Einstein equations, whose matter-terms in non-vacuum spacetimes are handled by the `Whisky` code.

In essence, while the `Cactus` code provides at each time step a solution of the Einstein equations [5]

$$G_{\mu\nu} = 8\pi T_{\mu\nu} \ , \tag{3.1}$$

where $G_{\mu\nu}$ is the Einstein tensor and $T_{\mu\nu}$ is the stress-energy tensor, the `Whisky` code provides the time evolution of the hydrodynamics equations, expressed through the conservation equations for the stress-energy tensor and for the matter current density J^{μ}

$$\begin{aligned} \nabla_{\mu} T^{\mu\nu} &= 0 \ , \\ \nabla_{\mu} J^{\mu} &= 0. \end{aligned} \tag{3.2}$$

For a perfect fluid, as the one considered in this thesis, the matter current density and the stress-energy tensor are

$$J^{\mu} = \rho u^{\mu} \tag{3.3}$$

$$T^{\mu\nu} = \rho h u^{\mu} u^{\nu} + p g^{\mu\nu} \tag{3.4}$$

where ρ is the rest-mass density, u^μ the four-velocity of the fluid, p the gas pressure, $h = 1 + \epsilon + p/\rho$ the specific relativistic enthalpy and ϵ the specific internal energy.

In what follows we discuss in more details the most important features of the code.

3.2 Quasi-linear hyperbolic systems

A system of partial differential equations is said to be in conservative form when it is written as:

$$\frac{\partial \mathbf{U}}{\partial t} + \frac{\partial \mathbf{F}}{\partial x} = 0 \tag{3.5}$$

where $\mathbf{U}$ is the set of conserved variables and $\mathbf{F}$ the fluxes. The system can then be easily rewritten in a quasi-linear form:

$$\frac{\partial \mathbf{U}}{\partial t} + \mathbf{A}\frac{\partial \mathbf{U}}{\partial x} = 0 \tag{3.6}$$

with $\mathbf{A}$ being the Jacobian of the flux vector, i.e. $\partial \mathbf{F}/\partial \mathbf{U}$.

A quasi-linear system of equations will be said to be *hyperbolic* if the matrix $\mathbf{A}^i$ has N real eigenvalues (where $N \times N$ is the dimension of the matrix) and admits a complete set of eigenvectors. The system is said to be *strictly hyperbolic* if the eigenvalues are all real and distinct.

To better appreciate the importance of having a quasi-linear hyperbolic system of equations let us start with the simplest conservative and hyperbolic equation, i.e. the linear advection equation:

$$\frac{\partial U}{\partial t} + a\frac{\partial U}{\partial x} = 0 \tag{3.7}$$

with initial conditions:

$$U(x, t = 0) = U_0(x) \tag{3.8}$$

The solution of this equation is easy to compute and it is simply

$$U(x, t) = U_0(x - at) \tag{3.9}$$

for $t \geq 0$. In other words the initial data simply propagates unchanged to the right (if $a > 0$) or to the left (if $a < 0$) with velocity a. The solution $U(x, t)$ is constant along each ray $x - at = x_0$, which are known as the *characteristics* of the equation. To see this we can differentiate $U(x, t)$ along one of the curves $x'(t) = \mathrm{d}x/\mathrm{d}t$ to obtain

$$\begin{aligned}
\frac{\mathrm{d}U(x(t), t)}{\mathrm{d}t} &= \frac{\partial U}{\partial t} + \frac{\partial U}{\partial x}x'(t) \\
&= \frac{\partial U}{\partial t} + a\frac{\partial U}{\partial x} \\
&= 0
\end{aligned} \tag{3.10}$$

confirming that U is constant along these characteristics.

This notation can be easily extended to system of equations like (3.6). If the system is hyperbolic it admits a full set of N right eigenvectors $\mathbf{R}^l$ with $l = (1, \ldots, N)$. If we indicate with $\mathbf{Q}$ the $N \times N$ matrix whose columns are $\mathbf{R}^l$, then

$$\mathbf{\Lambda} = \mathbf{Q}^{-1}\mathbf{A}\mathbf{Q} \tag{3.11}$$

where

$$\mathbf{\Lambda} = \mathrm{diag}(\lambda_1, \ldots, \lambda_N) \tag{3.12}$$

Introducing the *characteristic variables*

$$\mathbf{V} = \mathbf{Q}^{-1}\mathbf{U} \tag{3.13}$$

system (3.6) becomes

$$\frac{\partial \mathbf{V}}{\partial t} + \mathbf{\Lambda}\frac{\partial \mathbf{V}}{\partial x} = 0 \tag{3.14}$$

Since $\mathbf{\Lambda}$ is diagonal, this decouples into N independent scalar equations

$$\frac{\partial V_l}{\partial t} + \lambda_l \frac{\partial V_l}{\partial x} = 0 \quad l = 1, \ldots, N \tag{3.15}$$

whose solutions are given by

$$V_l(x,t) = V_l(x - \lambda_l t, 0) \tag{3.16}$$

The solution of the original system (3.6) can then be computed inverting equation (3.13), i.e. $\mathbf{U} = \mathbf{QV}$ or, in components,

$$\mathbf{U}(x,t) = \sum_{l=1}^{N} V_l(x - \lambda_l t, 0)\mathbf{Q}^l \tag{3.17}$$

We can then view the solution as being the superposition of N waves, each of which propagates undistorted with a speed given by the corresponding eigenvalue.

3.3 Equations of General Relativistic hydrodynamics

An important feature of the `Whisky` code is the implementation of a *conservative formulation* of the hydrodynamics equations [99, 22, 76], in which the set of equations (3.2) is written in the following hyperbolic, first-order and flux-conservative form:

$$\frac{1}{\sqrt{-g}}\{\partial_t[\sqrt{\gamma}\mathbf{F}^0(\mathbf{U})] + \partial_i[\sqrt{-g}\mathbf{F}^{(i)}(\mathbf{U})]\} = \mathbf{S}(\mathbf{U}) \ , \tag{3.18}$$

where $\mathbf{F}^{(i)}(\mathbf{U})$ and $\mathbf{S}(\mathbf{U})$ are the flux-vectors and source terms, respectively [57]. Note that the right-hand side of (3.18) depends only on the metric, and its first derivatives, and on the stress-energy tensor.

As shown in ref. [22], in order to write system (3.2) in the form of system (3.18), the *primitive* hydrodynamical variables $\mathbf{U} \equiv (\rho, v^i, \epsilon)$ are mapped to the so called *conserved* variables $\mathbf{F}^0(\mathbf{U}) \equiv (D, S_i, \tau)$ via the relations

$$\begin{aligned} D &\equiv \rho W \ , \\ S_i &\equiv \rho h W^2 v_i \ , \\ \tau &\equiv \rho h W^2 - p - D \ , \end{aligned} \tag{3.19}$$

where v^i is the fluid three-velocity (as measured by an Eulerian observer), ϵ is the specific internal energy and $W \equiv (1 - \gamma_{ij} v^i v^j)^{-1/2}$ is the Lorentz factor. The explicit expression for the fluxes and for the source terms are given by:

$$\begin{aligned} \mathbf{F}^{(i)} &= [D(v^i - \beta^i/\alpha), S_j(v^i - \beta^i/\alpha) + p\delta^i_j, \tau(v^i - \beta^i/\alpha) + pv^i]^T && (3.20) \\ \mathbf{S} &= [0, T^{\mu\nu}(\partial_\mu g_{\nu j} + \Gamma^\delta_{\mu\nu} g_{\delta j}), \alpha(T^{\mu 0}\partial_\mu \ln\alpha - T^{\mu\nu}\Gamma^0_{\nu\mu})]^T && (3.21) \end{aligned}$$

In order to close the system of equations for the hydrodynamics an equation of state (EOS) which relates the pressure to the rest-mass density and to the energy density must be specified. The code has been written to use any EOS, but all of the simulations so far have been performed using either an (isentropic) polytropic EOS

$$\begin{aligned} p &= K\rho^\Gamma \ , && (3.22) \\ e &= \rho + \frac{p}{\Gamma - 1} \ , && (3.23) \end{aligned}$$

or an "ideal-fluid" EOS

$$p = (\Gamma - 1)\rho\,\epsilon \ . \qquad (3.24)$$

Here, e is the energy density in the rest-frame of the fluid, K the polytropic constant and Γ the adiabatic exponent. In the case of the polytropic EOS (3.22), $\Gamma = 1 + 1/N$, where N is the polytropic index and the evolution equation for τ needs not be solved. In the case of the ideal-fluid EOS (3.24), on the other hand, non-isentropic changes can take place in the fluid and the evolution equation for τ needs to be solved.

Additional details of the formulation used for the hydrodynamics equations can be found in ref. [57]. We stress that an important feature of this formulation is that it has allowed to extend to a general relativistic context the powerful numerical methods developed in classical hydrodynamics, in particular high resolution shock-capturing (HRSC) schemes based on linearized Riemann solvers (see ref. [57]). Such schemes are essential for a correct representation of shocks, whose presence is expected in several astrophysical scenarios. Two important results corroborate this view. The first one, by Lax and Wendroff [90], states that if a stable conservative scheme converges, then it converges toward a weak solution of the hydrodynamical equations. The second one, by Hou and LeFloch [74], states that, in general, a non-conservative scheme will converge to the wrong weak solution in the presence of a shock, hence underlining the importance of flux-conservative formulations. In the following section we will give some details of HRSC schemes; for a full introduction to these methods the reader is also referred to refs. [89, 143, 94]

3.4 Numerical methods

Details about all the numerical methods implemented in the `Whisky` code can be found in refs. [15, 16]; here we summarize the most important ones.

3.4.1 High-Resolution Shock-Capturing methods

Having written the system of equations in the conservative form (3.5) we can use numerical schemes based on the characteristic structure of the system. It is demonstrated that if a numerical scheme written in conservative form converges, it automatically guarantees the correct Rankine-Hugoniot conditions across discontinuities, for example shocks [93, 143]. This means that the code is able to assure the conservation of quantities like mass, energy and momentum also in presence of strong shocks.

High-Resolution Shock-Capturing schemes are conservative numerical methods that consist in the numerical solution of equation (3.5) in its integral form, guaranteeing the conservation of the set of conserved variables (if the sources are zero).

First of all let us consider a single computational cell of our discretized spacetime and let Ω be a region of spacetime bounded by two space-like hypersurfaces Σ_t and $\Sigma_{t+\Delta t}$ and by six timelike surfaces $\Sigma_{x^i-\Delta x^i/2}$ and $\Sigma_{x^i+\Delta x^i/2}$. The integral form of equation (3.18) can then be expressed as

$$\int \partial_t(\sqrt{\gamma}\mathbf{F}^0)\mathrm{d}\Omega = -\int \partial_i(\sqrt{-g}\mathbf{F}^i)\mathrm{d}\Omega + \int \sqrt{-g}\mathbf{S}\mathrm{d}\Omega \tag{3.25}$$

where $\mathrm{d}\Omega \equiv dtdxdydz$. This equation can then be rewritten in the following conservation form:

$$\begin{aligned}(\Delta V\bar{\mathbf{F}}^0)\big|_{t+\Delta t} - (\Delta V\bar{\mathbf{F}}^0)\big|_t = & \\ & -\int_{\Sigma_{x+\Delta x/2}}(\sqrt{-g}\mathbf{F}^x)\mathrm{d}t\mathrm{d}y\mathrm{d}z + \int_{\Sigma_{x-\Delta x/2}}(\sqrt{-g}\mathbf{F}^x)\mathrm{d}t\mathrm{d}y\mathrm{d}z \\ & -\int_{\Sigma_{y+\Delta y/2}}(\sqrt{-g}\mathbf{F}^y)\mathrm{d}t\mathrm{d}x\mathrm{d}z + \int_{\Sigma_{y-\Delta y/2}}(\sqrt{-g}\mathbf{F}^y)\mathrm{d}t\mathrm{d}x\mathrm{d}z \\ & -\int_{\Sigma_{z+\Delta z/2}}(\sqrt{-g}\mathbf{F}^z)\mathrm{d}t\mathrm{d}x\mathrm{d}y + \int_{\Sigma_{z-\Delta z/2}}(\sqrt{-g}\mathbf{F}^z)\mathrm{d}t\mathrm{d}x\mathrm{d}y \\ & +\int \sqrt{-g}\mathbf{S}\mathrm{d}\Omega \end{aligned} \tag{3.26}$$

where $\bar{\mathbf{F}}^0$ is defined as

$$\bar{\mathbf{F}}^0 \equiv \frac{1}{\Delta V}\int_{\Delta V}\sqrt{\gamma}\mathbf{F}^0\mathrm{d}x\mathrm{d}y\mathrm{d}z \tag{3.27}$$

with

$$\Delta V \equiv \int_{x-\Delta x/2}^{x+\Delta x/2}\int_{y-\Delta y/2}^{y+\Delta y/2}\int_{z-\Delta z/2}^{z+\Delta z/2}\sqrt{\gamma}\mathrm{d}x\mathrm{d}y\mathrm{d}z \tag{3.28}$$

At this point we introduce the numerical fluxes defined at the boundaries between the numerical cells and defined as the time averages of the fluxes

$$\hat{\mathbf{F}}^i \equiv \frac{1}{\Delta t}\int_t^{t+\Delta t}\sqrt{-g}\mathbf{F}^i dt \tag{3.29}$$

If we now divide equation (3.26) by ΔV and ignore the source term we obtain

$$\frac{(\bar{\mathbf{F}}^0)\big|_{t+\Delta t} - (\bar{\mathbf{F}}^0)\big|_t}{\Delta t} = \sum_{i=1,3}\frac{\left(\hat{\mathbf{F}}^i\right)\Big|_{x^i-\Delta x^i/2} - \left(\hat{\mathbf{F}}^i\right)\Big|_{x^i+\Delta x^i/2}}{\Delta x^i} \tag{3.30}$$

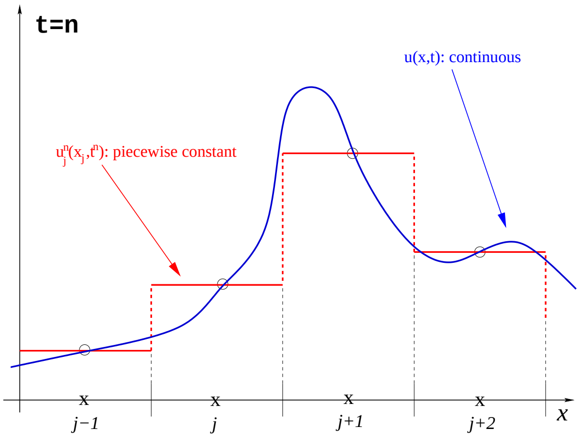

Figure 3.1 Schematic picture of the process of discretization. The continuous function $U(x,t)$ is approximate by a piecewise constant function U_j^n on the numerical grid. As a result, a series of Riemann problems is set up at each interface between the cells. (Figure courtesy of L. Rezzolla)

In order to compute the numerical fluxes used in equation (3.30), the primitive variables are *reconstructed* within each cell (see figures 3.1 and 3.2). This gives two values at the left and at the right of each cell boundary which define locally a Riemann problem whose solution is then used to compute the numerical flux.

3.4.2 Reconstruction methods

For the reconstruction procedure, the `Whisky` code implements several different approaches, including slope-limited TVD methods, the Piecewise Parabolic Method [34] and the Essentially Non-Oscillatory method [67]. By default we use PPM as this seems to be the best balance between accuracy and computational efficiency, as shown, for example, in ref. [60].

The PPM method of Colella and Woodward [34] is a composite reconstruction method that has special treatments for shocks, where the reconstruction is modified to retain monotonicity, and contact surfaces, where the reconstruction is modified to sharpen the jump. PPM contains a number of tunable parameters, but those suggested by Colella & Woodward [34] are always used. Another important characteristic of PPM is that it is third-order accurate for smooth flows.

3.4.3 Riemann solvers

Once the reconstruction procedure has provided data on either side of each cell boundary, this is then used to specify the initial states of the semi-infinite piecewise constant Riemann problems. The solution of a Riemann problem consists indeed of determining the evolution of a fluid which has two adjacent uniform states characterized by different values of velocity, density and pressure. Because of the complexity of the equations the solution

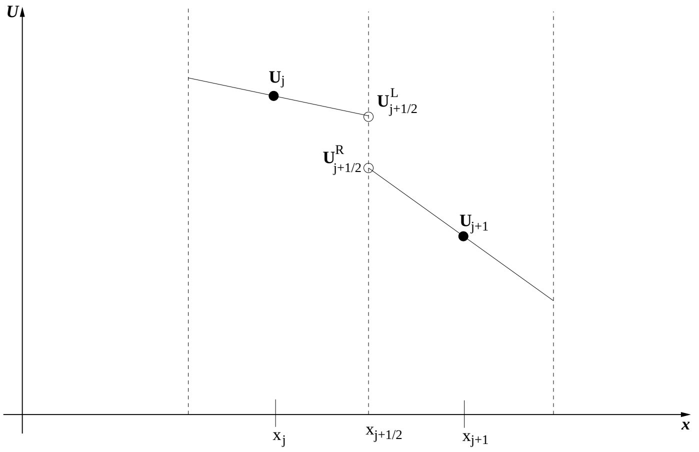

Figure 3.2 A schematic picture of the reconstruction procedure. The values at the left $U^L_{j+1/2}$ and at the right $U^R_{j+1/2}$ of the interface between cells j and $j+1$ define the initial left and right state of a Riemann problem whose solution gives the value of the fluxes at $j + 1/2$.

cannot be found in general analytically, but requires the numerical solution of a system of algebraic nonlinear equations.

The exact solution of the Riemann problem in relativistic hydrodynamics was found for the first time by Martí & Müller [100] when the velocity tangential to the initial discontinuity are zero and then extended to the more general case by Pons *et al.* [116]. These solutions were then extensively used to test special and general relativistic codes. Even if these exact solvers were recently improved incrementing their computational efficiency by Rezzolla *et al.* [122, 123], their computational cost remains still too high to be currently implemented in a numerical code. For this reason the computation of the fluxes in HRSC schemes is done using an approximate solution of the Riemann problems at the cell boundaries.

Whisky implements different approximate Riemann solvers but the one used by default to compute the numerical fluxes in our simulations is the Marquina flux formula [44, 43, 9]. This approximates the solution of the Riemann problem by only two waves with the intermediate state given by the conservation of the mass-flux; at possible sonic points a Lax-Friedrichs flux is used, ensuring that the solution does not contain rarefaction shocks.

The Marquina flux formula requires the computation of the eigenvalues and eigenvectors of the linearized Jacobian matrices $\mathbf{A}_L$ and $\mathbf{A}_R$ given by $\mathbf{F}_L = \mathbf{A}_L\mathbf{U}_L$ and $\mathbf{F}_R = \mathbf{A}_R\mathbf{U}_R$. The analytic expressions for the left eigenvectors [76] are implemented in the code, thus avoiding the computationally expensive inversion of the three 5×5 matrices of the right eigenvectors, associated to each spatial direction.

3.4.4 Time update: the method of lines

The reconstruction methods guarantee that a prescribed order of accuracy is retained for the discretized representation of a given spatial differential operator. However, the need to retain a high-order accuracy also in time can complicate considerably the evolution from a time-level to the following one. As a way to handle this efficiently, a method of line (MoL) approach [89, 143] is followed. Here, the continuum equations are considered to be discretized in space only. The resulting system of ordinary differential equations (ODEs) can then be solved numerically with any stable solver. This method minimizes the coupling between the spacetime and hydrodynamics solvers and allows for a transparent implementation of different evolution schemes.

In practice this is achieved by considering the numerical values of the conserved variables at each point of the numerical grid $\mathbf{F}^0_{i,j,k} \equiv \mathbf{F}^0(\mathbf{U}_{i,j,k})$ as the cell average $\bar{\mathbf{F}}^0_{i,j,k}$ defined in equation (3.27). We know already from the integral form of our equations, see equation (3.30), that the cell average $\bar{\mathbf{F}}^0$ evolves according to:

$$\frac{\mathrm{d}\mathbf{F}^0_{i,j,k}}{\mathrm{d}t} = \frac{\mathrm{d}\bar{\mathbf{F}}^0_{i,j,k}}{\mathrm{d}t} = \sum_{l=1,3} \frac{\left(\hat{\mathbf{F}}^l\right)\Big|_{x^l_{i,j,k}-\Delta x^l/2} - \left(\hat{\mathbf{F}}^l\right)\Big|_{x^l_{i,j,k}+\Delta x^l/2}}{\Delta x^l} + \mathbf{S}_{i,j,k} \tag{3.31}$$

where $\mathbf{S}_{i,j,k}$ are the sources computed from the primitive variables $\mathbf{U}_{i,j,k}$. The system written in this way is reduced to a set of ordinary differential equations (ODE) that can be now integrated with standard ODE solvers, such as the third-order TVD Runge-Kutta.

The calculation of the right hand side of equation (3.31) in the `Whisky` code splits into the following parts:

1. Calculation of the source terms $\mathbf{S}(\mathbf{U})$ at all the grid points.
2. For each direction x^l:
    - Reconstruction of the data $\mathbf{U}$ to both sides of a cell boundary. In this way, two values $\mathbf{U}_{L}$ and $\mathbf{U}_{R}$ of $\mathbf{U}_{x^l+\Delta x^l/2}$ are determined at the cell boundary.
    - Solution at cell boundary of the approximate Riemann problem having the values $\mathbf{U}_{L,R}$ as initial data.
    - Calculation of the inter-cell flux $\hat{\mathbf{F}}^l$, that is, of the flux across the interface.

After the conserved variables $\mathbf{F}^0(\mathbf{U})$ are evolved, the primitive variables are recovered and the stress-energy tensor is computed for use in the Einstein equations.

3.4.5 Treatment of the atmosphere

At least mathematically, the region outside the stellar models studied in Chapter 4 is assumed to be perfect vacuum. Independently of whether this represents a physically realistic description of a compact star, the vacuum represents a singular limit of the equations (3.18) and must be treated in a different way. `Whisky` adopts a standard approach in computational fluid-dynamics and a tenuous "atmosphere" is added filling the computational domain outside the star. The evolution of the hydrodynamic equations in grid zones where the atmosphere is present is the same as the one used in the bulk of the flow. Furthermore, when the rest mass in a grid zone falls below the threshold set by the atmosphere, that grid zone is simply not updated in time.

3.4.6 Hydrodynamical excision

Excision boundaries are usually based on the principle that a region of spacetime that is causally disconnected can be ignored without this affecting the solution in the remaining part of the spacetime. Although this is true for signals and perturbations traveling at physical speeds, numerical calculations may violate this assumption and disturbances, such as gauge waves[1], may travel at larger speeds thus leaving the physically disconnected regions.

A first naive implementation of an excision algorithm within a HRSC method could ensure that the data used to construct the flux at the excision boundary is extrapolated from data outside the excision region. This may appear to be a good idea since HRSC methods naturally change the stencils depending on the data locally. In general, however, this approach is not guaranteed to reduce the total variation of the solution and simple examples may be produced that fail with this boundary condition.

An effective solution, however, is not much more complicated and can be obtained by applying at the excision boundary the simplest outflow boundary condition (here, by outflow we mean flow into the excision region). In practice, a zeroth-order extrapolation is applied to all the variables at the boundary, *i.e.* a simple copy of the hydrodynamical variables across the excision boundary (see figure 3.3). If the reconstruction method requires more cells inside the excision region, the stencil is forced to consider only the data in the exterior and the first interior cell. Although the actual implementation of this excision technique may depend on the reconstruction method used, the working principle is always the same.

The location of the excision boundary itself is based on the determination of the apparent horizon which, within the `Cactus` code, is obtained using the fast apparent horizon finder of Thornburg [142]. More details on how the hydrodynamical excision is applied in practice, as well as tests showing that this method is stable, consistent and converges to the expected order can be found in ref. [69].

---

[1] Gauge waves are disturbances of the metric components which do not correspond to physical perturbations. These gauge waves are often the result of improper gauge conditions.

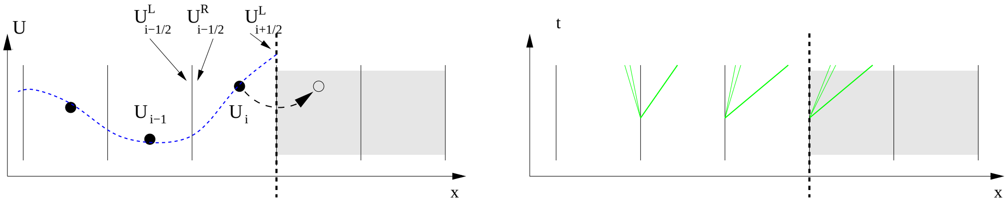

Copy to set up reconstruction.

Only fluxes for the boundaries of cells outside the excised region are required.

Figure 3.3 A schematic view of the excision algorithm. The excision boundary is represented by the vertical dotted line while the shaded gray region represents the excised cells. On the left panel is shown how the reconstruction method is modified. In the right panel the characteristic curves. (Figure courtesy of F. Löffler)

Chapter 4

Collapse of differentially rotating neutron stars

4.1 Introduction

In ref. [16] the case of the collapse of uniformly rotating neutron stars was studied, where a specific set of dynamically unstable models was constructed (D1 to D4) for a polytropic index of N=1.0. The region of instability to axisymmetric perturbations was found by constructing constant angular-momentum sequences and applying the turning point criterion of Friedman, Ipser and Sorkin [62]. Models D1 to D4 were then chosen to be near the line of marginal stability, but with somewhat larger central density, in order to ensure dynamical (and not just secular) instability (see Table 1 and Figure 1 of ref. [16]). Our main goal is to study the effect of differential rotation on the collapse of dynamically unstable rotating neutron stars. There are several reasons to believe this is an important step towards a more realistic description of this problem.

Differentially rotating neutron stars can be the results of several astrophysical scenarios such as core collapse or binary neutron stars mergers when the mass of the system is below a certain threshold depending on the equation of state (see refs. [135, 133, 134]). Because of their differential rotation these stars can support masses higher than uniformly rotating neutron stars (see ref. [25]) and they can reach very high values of J/M^2, even larger than 1, which was not possible in the case of uniform rotation (*e.g.* in ref. [16] the fastest uniformly rotating model D4 has $J/M^2 = 0.54$). These objects are particularly interesting because they can be related to events like short γ-ray burst, which are thought indeed to originate from the merger of two neutron stars, and can be powerful sources of gravitational radiation.

4.2 Initial stellar models

We construct our initial stellar models as isentropic, differentially rotating relativistic polytropes, satisfying the EOS (3.22). We further assume they are stationary and axisymmetric equilibrium models so that the spacetime geometry is described by a metric of the form

$$ds^2 = -e^{2\nu}dt^2 + e^{2\psi}(d\phi - \omega dt)^2 + e^{2\mu}(dr^2 + r^2 d\theta^2), \tag{4.1}$$

where ν, ψ, μ and ω are functions of the quasi-isotropic coordinates r and θ only. The degree of differential rotation as well as its variation within the star are essentially unknown and because of this we here employ the usual "$\jmath$-constant" law of differential rotation

$$A^2(\Omega_c - \Omega) = \frac{(\Omega - \omega)e^{2\psi}}{1 - (\Omega - \omega)e^{2\psi}}, \tag{4.2}$$

where A is a constant (with dimension of length) that represents the length scale over which the angular velocity changes. In the remainder of this Chapter, we will measure the degree of differential rotation by the rescaled quantity $\hat{A} \equiv A/r_e$, where r_e is the equatorial coordinate radius of the star. For $\hat{A} \to \infty$ uniform rotation is recovered while a low value of $\hat{A}$ indicates an high degree of differential rotation.

4.2.1 Supra-Kerr and Sub-Kerr models

When studying the collapse to a Kerr black hole, an interesting question is what happens to a configuration with $J/M^2 > 1$ (supra-Kerr). It is indeed expected that such models will not show a simple transition to Kerr black hole because they have to loose angular momentum in order to reduce the value of J/M^2 below 1. We recall in fact that Kerr black holes can not exist with values of J/M^2 greater than one. In previous studies [48], such initial configurations were constructed starting from a dynamically stable supra-Kerr model and then induced to collapse by dramatically depleting the pressure support. Here, we investigate the question whether dynamically unstable supra-Kerr models (as exact initial data) exist for a wide range of polytropic indices. We have constructed a large set of initial models for various values of the polytropic index N and degree of differential rotation $\hat{A}$, reaching close to the mass-shedding limit and spanning a wide range of central densities.

Figure 4.1 shows the value of J/M^2 as a function of central rest-mass density ρ_c for the three different EOSs with $N = 0.5$, $N = 0.75$ and $N = 1.0$. In these sequences the rotation law and the polar to equatorial axes ratio are fixed to $\hat{A} = 1.0$ and $r_p/r_e = 0.35$, respectively. The choice of $\hat{A} = 1.0$ is a typical one representing moderate differential rotation, while the axis ratio of 0.35 refers to very rapidly rotating models near the mass-shedding limit (when the limit exits). Along each sequence, we mark the model which roughly separates stable models (at lower central densities) from unstable models (at higher central densities) by a circle. As we do not know precisely what are the marginally stable models (no simple turning point criterion exists in the case of differential rotation) we use as a reference the stability limit of the non-rotating models and thus we mark with a circle the central rest-mass density of the non-rotating model having the maximum mass for each EOS. Stated differently, all models to the right of the circles are expected to be dynamically unstable or very close to the instability threshold.

As becomes clear from this figure, all unstable models we were able to construct are sub-Kerr (*i.e.* $J/M^2 < 1$). In fact, in order to find supra-Kerr models, one must reach very low densities, where equilibrium models are very stable against axisymmetric perturbations. The evidence that for the particular sequences we constructed the value of

J/M^2 in the unstable region becomes nearly constant for each EOS, is a strong indication that all unstable models are indeed sub-Kerr.

In order to investigate further the effect of the value of the differential-rotation-law parameter $\hat{A}$ and of the EOS on the above conclusion, we have investigated a large number of rapidly rotating models, spanning a wide range of values for $\hat{A}$ (between 0.6 and 1.8) and a wide range of polytropic indices (between 0.5 and 1.5). In all cases, we have computed the value of J/M^2 of the most rapidly rotating models we could construct with our numerical method (which was normally close to the mass-shedding limit, when it exists) for a central density equal to that of the maximum-mass non-rotating model (*i.e.* for the models marked by circles in fig. 4.1). Fig. 4.2 shows that all the models with a central density equal to the maximum-mass non-rotating stars have $J/M^2 < 1$ and we point that fig. 4.1 shows that all the unstable models (*i.e.* the ones with an higher central density) have a value of J/M^2 lower than the models shown in fig. 4.2. It is therefore evident that no combination of N and $\hat{A}$ could yield an unstable supra-Kerr model. This result, combined with the tendency of the lines in fig. 4.1 at densities larger than the central density of the maximum-mass non-rotating model, provide strong evidence that all supra-Kerr model found **are not** dynamically unstable.

It should be noted that because our numerical method does not reach exactly the mass-shedding limit for any degree of differential rotation (it is difficult to achieve convergence at very small values of the axes ratio r_p/r_e) and since the existence of a bifurcation between quasi-spheroidal and quasi-toroidal models with the same axes ratio[1] and central density has not been investigated yet, we cannot strictly exclude the existence of supra-Kerr unstable models.

The rapidly rotating models shown in fig. 4.2 are also shown in fig. 4.3 (dotted lines) in a diagram plotting their mass versus the maximum energy density. Since the most rapidly rotating models with differential rotation and small axes ratio are quasi-toroidal, the maximum energy density is larger than the central energy density within a factor of roughly two, depending on the degree of differential rotation. It is not yet known whether the value of the central energy density or of the off-center maximum energy density is more important in determining the stability to axisymmetric perturbations of quasi-toroidal models. Therefore, the models shown in figs. 4.2 and 4.3 could either be only marginally stable or unstable or strongly unstable. Nevertheless, the fact that the central density of models in fig. 4.1 with $J/M^2 > 1$ is at least a factor of three smaller than the central density of the corresponding maximum-mass non-rotating models, indicates that even if all models in fig.4.3 are well inside the dynamically unstable region, there should still be no supra-Kerr unstable models for the parameter range examined.

4.2.2 Initial data

We investigate the dynamics of differentially rotating collapsing compact stars by focusing on three (sub-Kerr) dynamically unstable models and one (supra-Kerr) artificially pressure-depleted model. All models are constructed for the polytropic EOS with N=K=1.

---

[1] We define quasi-spheroidal models those having the central and maximum rest-mass density being coincident, while we define quasi-toroidal models those having the maximum of ρ not located in the center.

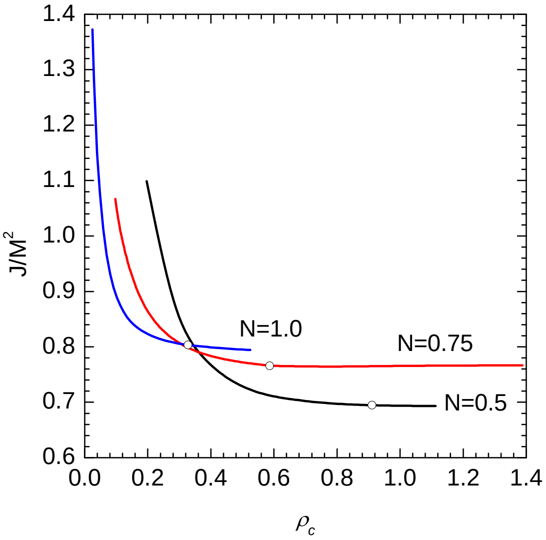

Figure 4.1 J/M^2 as a function of central rest-mass density ρ_c for $N = 0.5$, $N = 0.75$ and $N = 1.0$, when the rotation law and the polar to equatorial axes ratio are fixed to $\hat{A} = 1.0$ and $r_p/r_e = 0.35$, respectively. The circle denotes roughly the separation between stable (at the left of the circle) and unstable (at the right) models along each sequence. (Figure courtesy of N. Stergioulas)

Table 4.1. Initial data for the different stellar models

Model	ρ_c	r_p/r_e	$M/M_\odot$	R_e	Ω_c	$T/\|W\|$	J/M^2	$\hat{A}$
A1	0.30623	0.23	1.7626	0.62438	5.1891	0.18989	0.75004	0.6
A2	0.30623	0.33	2.2280	0.78684	2.1752	0.21705	0.81507	1.0
A3	0.30623	0.33	2.6127	1.07410	1.0859	0.23163	0.88474	1.4
B1	0.04630	0.39	1.9009	1.67630	0.3723	0.21509	1.08650	1.0

Note. — The different columns refer, respectively, to: the central rest-mass density ρ_c, the ratio of the polar to the equatorial coordinate radii r_p/r_e, the total mass M rescaled to $K = 100$ (see ref. [35] for scaling to arbitrary K), the circumferential equatorial radius R_e, the central angular velocity Ω_c, the ratio of rotational kinetic energy to gravitational binding energy $T/|W|$, the ratio J/M^2 where J is the angular momentum, the degree of differential rotation $\hat{A}$ where for $\hat{A} \to \infty$ uniform rotation is recovered. All the initial models have been computed with a polytropic EOS with $K = 1$ and $N = 1$.

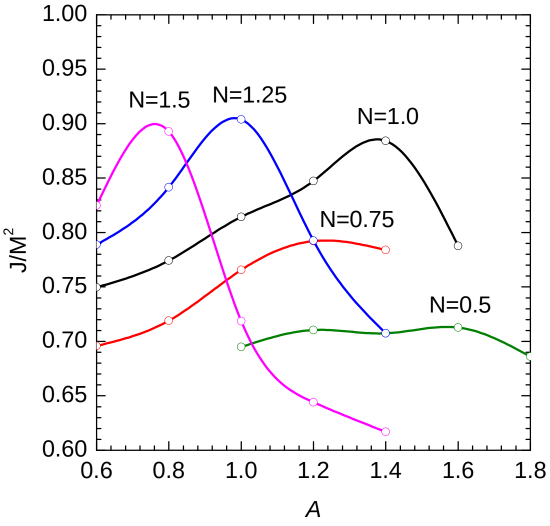

Figure 4.2 J/M^2 of the most rapidly rotating models with a central density equal to that of the maximum-mass non-rotating models(*i.e.* for the models marked with the circles in fig. 4.1) as a function of the rotation law parameter $\hat{A}$ and for different values of N. All models have $J/M^2 < 1$ indicating the difficulty of finding unstable supra-Kerr models. (Figure courtesy of N. Stergioulas)

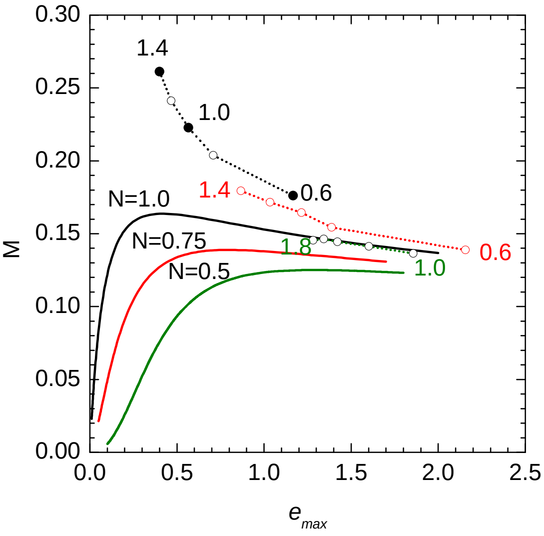

Figure 4.3 The dotted lines represent the total mass M of some of the unstable models shown in figure 4.2 as a function of the maximum energy density for $N = 0.5, 0.75, 1.0$; the different values of $\hat{A}$ are reported near each model. The solid lines instead show the mass of the non-rotating models for different values of N. (Figure courtesy of N. Stergioulas)

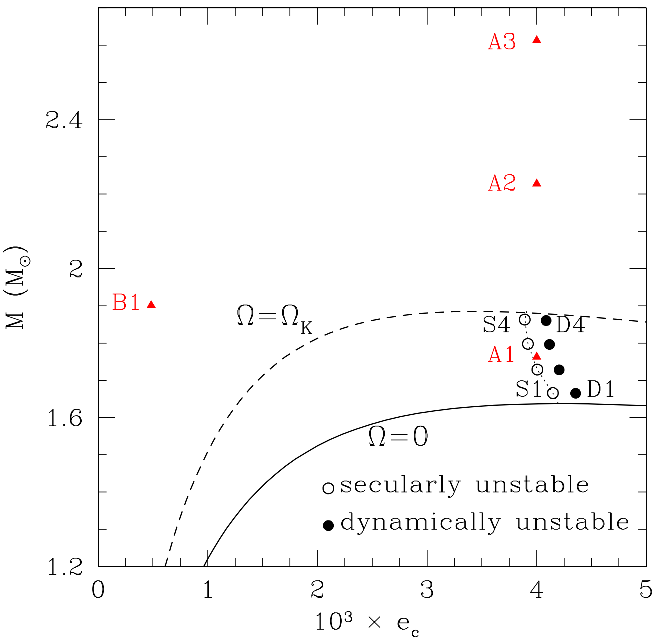

Figure 4.4 Comparison between our initial models (see table 4.1) and the uniformly rotating models studied in ref. [16]. Here we plot the gravitational mass M as a function of the central energy density e_c. Our initial models, marked with filled triangles, are rescaled to $K = 100$ (see ref. [35] for scaling to arbitrary K) for comparison with the others. The solid, dashed and dotted lines correspond to the sequence of non-rotating models, the sequence of models rotating at the mass shedding limit and the sequence of uniformly rotating models that are at the onset of the secular instability to axisymmetric perturbations. Also shown are the secularly (open circles) and dynamically unstable (filled circles) initial models used in ref. [16].

The three dynamically unstable models are labeled as $A1$ to $A3$ and are shown as filled dots in fig 4.3 while their detailed properties are displayed in table 4.1. The central rest mass density of the three models is chosen to be the same as the central rest mass density of the maximum mass non-rotating model for this EOS. The degree of differential rotation varies from $\hat{A} = 0.6$ to $\hat{A} = 1.4$. The maximum density increases with respect to the central density, as differential rotation becomes stronger (i.e. as the relative length scale $\hat{A}$ becomes smaller). All three models have comparable values of J/M^2 (0.75 to 0.88), $T/|W|$ (0.19 to 0.23) and M (0.18 to 0.26), while they differ significantly in radius (0.64 to 1.1) and central angular velocity (5.2 to 1.1). Even though the axisymmetric stability of these models could not be known from a turning-point method, our numerical simulations showed that these models are indeed dynamically unstable and collapse without the need of a pressure depletion.

The fourth model we studied (model $B1$ in table 4.1) is a stable supra-Kerr model, with comparable mass and $T/|W|$ as models $A1$ to $A3$, but with much smaller central density and $J/M^2 = 1.09$. As this model is far into the stable region, the only way to achieve a collapse is by artificial pressure depletion. This was already done for this particular model in ref. [48]. In spite of the fact that these initial data are unphysical (due to the large artificial pressure depletion) we chose to study this model in order to compare with the findings in ref. [48], who observed the onset of a non-axisymmetric instability towards the end of their simulation. Note that, to our knowledge, all previous studies of “supra-Kerr collapse” of compact stars were performed with artificially pressure-depleted stable models. However, it has not yet been demonstrated that the actual collapse of differentially rotating compact stars could follow a path that, through some physical effect, comes close to the initial data with strong pressure depletion.

In fig. 4.4 we also compare the gravitational mass M and central energy density e_c of our initial models with the uniformly rotating models studied in ref. [16].

4.3 Challenging excision

As already pointed in Section 3.4.6 the `Whisky` code implements an excision algorithm which consists essentially in ignoring a portion of the grid contained in the apparent horizon (AH) and applying suitable boundary conditions. This technique made possible the simulation of collapsing neutron stars to black holes but it has revealed to be not sufficiently strong or to be even the cause of possible instabilities.

In order to improve the duration of numerical simulations involving the formation of black holes, a new technique, not based on the excision mechanism described in Section 3.4.6, was implemented and tested in ref. [18]. Baiotti *et al.* [18] demonstrated indeed that the absence of an excised region improves dramatically the long-term stability in their simulations of the collapse of uniformly rotating NS, allowing for the calculation of the gravitational waveforms well beyond what previously possible and past the black-hole quasi-normal-mode (QNM) ringing.

Another important ingredient for the stable evolution of the Einstein equations in the absence of an excision algorithm is the introduction of an artificial dissipation of the Kreiss-Oliger type [88] on the right-hand-sides of the evolution equations for the field variables (no dissipation is introduced for the hydrodynamical variables). The dissipation is needed mostly because all the field variables develop very steep gradients in the region inside the AH. Under these conditions, small high-frequency oscillations (either produced by finite-differencing errors or by small reflections across the refinement boundaries) can easily be amplified, leave the region inside the AH and rapidly destroy the solution. In practice, for any time-evolved field variable u, the right-hand-side of the corresponding evolution equation is modified with the introduction of a term of the type $\mathcal{L}_{\rm diss}(u) = -\varepsilon \Delta x_i^3 \partial_{x_i}^4 u$, where ε is the dissipation coefficient, which is allowed to vary in space. In ref. [18] different configurations were used in which the coefficient was either constant over the whole domain or larger for the gridpoints inside the AH without noticing significant difference between these two cases.

In the results reported here for the collapse of sub-Kerr models A1, A2 and A3 a value of $\varepsilon = 0.01$ was used over all the domain except for few grid points inside the inner apparent horizon where ε was allowed to increase linearly with a slope equal to 2 up to a maximum value of 0.2. Other possible choices, such as the use of a constant value of ε over all the domain and with lower values are currently under investigation.

4.4 Dynamics of the collapse

Here we report the dynamics of the matter during the collapse of the initial stellar models described in the preceding section. All the models were studied with different resolutions but, because of the different dynamics, the sub-Kerr models (A1, A2, A3) were studied using progressive mesh refinement techniques in order to be able to extract gravitational-wave signal in a region of space sufficiently distant from the sources. The supra-Kerr model (B1) instead was studied using only one grid because the dynamics of this model is not limited to the central regions of the computational domain (the process follows several bounces and subsequent collapses) and so we have maintained a single refinement level and moved the outer boundaries at those distances that were computationally affordable. An ideal-fluid EOS (3.24) with $\Gamma = 2$ (*i.e.* $N = 1$) was used during the evolution of all the models.

4.4.1 Sub-Kerr Collapse

All the three sub-Kerr models considered (A1, A2, A3) show the same qualitative dynamics, with the gravitational collapse leading to a central black hole in vacuum. All of them were evolved in bitant and $\pi/2$ symmetry (*i.e.* we considered the region $\{x > 0, y > 0, z > 0\}$ applying reflection symmetry at $z = 0$, so that $\mathbf{U}(x, y, -z) = \mathbf{U}(x, y, z)$, and a rotating symmetry at $x = 0$ and $y = 0$) and they did not show the development of any nonaxisymmetric instability, in a way similar to the uniformly rotating models studied in ref. [16].

Because of the similar behavior we concentrate here on the description of model A2, which was studied both with fixed and progressive mesh refinement; in the former the region inside the apparent horizon was excised while in the latter we made use of the Kreiss-Oliger dissipation on the field components obtaining a longer and more stable simulation. The results showed here were produced with the latter on a grid with boundaries located at $[0, 86.2M] \times [0, 86.2M] \times [0, 86.2M]$ with a resolution ranging from $\Delta x^i = 1.4M$ on the coarsest grid to $\Delta x^i = 0.02M$ on the finest level. At the end of the run a total of seven refinement levels were active. Reflection symmetry was used on the equatorial plane and $\pi/2$ symmetry on $x = 0$ and $y = 0$. The collapse was triggered reducing the pressure by 2% as done in the case of uniformly rotating models in ref. [16].

As one can see in the first frame of figure 4.5, where we plot the isodensity contours in the equatorial and xz plane, the star has a toroidal shape due to its strong differential rotation. Its evolution is rather similar to what was already observed for the uniformly rotating models and especially for model D4 in ref. [16]. The collapse is axisymmetric and leads to the formation of a black hole. The apparent horizon (AH), represented by a dashed line in figure 4.6, is found at $t = 5.9P_{rot,c}$, where $P_{rot,c}$ is the initial rotational period at the center of the star and is equal to $13M$. It is important to stress that the AH may not coincide with the event horizon (not shown here) which has to be necessarily computed analyzing the data at the end of the simulation. At the time the apparent horizon is formed, the star has assumed the shape of a disk which rapidly accretes until no matter is left outside, as one can see from the last frame of figure 4.6. Even if an ideal-fluid equation of state is used we did not see the formation of strong shocks during the collapse. This can be also seen looking at fig. 4.7 where we plot the maximum of the rest-mass density and of the internal energy normalized at their initial values. In this figure the time at which the apparent horizon is found is denoted by a vertical dotted line. In fig. 4.8 we also plot the minimum of the lapse function α which "collapse" to 0 indicating the formation of a black hole. The simulation was halted at a time $t \approx 220M$ after there was no matter, except for the atmosphere (see Section 3.4.5), left outside the black hole. We stress again that these results were obtained without the use of the excision technique described in Section 3.4.6 but with the introduction of the Kreiss-Oliger dissipation on the field variables. This makes possible to have a longer simulation while the run done with the use of excision crashed after few iterations after the formation of the apparent horizon.

In fig. 4.9 we compare the total rest-mass and the total angular momentum of all the three models (A1,A2,A3) normalized to their initial values. Note that as expected models with a lower value of J/M^2 collapse earlier than the others.

4.4.2 Supra-Kerr Collapse

Model B1 has $J/M^2 = 1.1$ and shows a very different dynamics with respect to the sub-Kerr stars. Here we report the results obtained with a grid of $120 \times 240 \times 250$ points and boundaries located at $[0, 34M] \times [-34M, 34M] \times [0, 13.2M]$ where we used equatorial and π-symmetry (this means that we evolved only the region $\{x > 0, z > 0\}$ applying a rotational symmetry boundary condition at $x = 0$ and reflection symmetry at $z = 0$).

Model B1 is a very stable configuration so we had to force its collapse by reducing the initial pressure by 99% as done by Duez *et al.* [48]. Without its pressure support the star immediately flattens along the z-direction and collapses toward the center on the equatorial plane producing a strong shock. After a first bounce, due to the centrifugal barrier produced by the high angular momentum, a torus [2] forms which rapidly fragments

---

[2] For torus we mean a configuration in which the maximum of ρ is not located in the center and $\rho_c \ll \max(\rho)$ but still $\rho_c \neq 0$, where ρ_c is the value of the rest-mass density at the center.

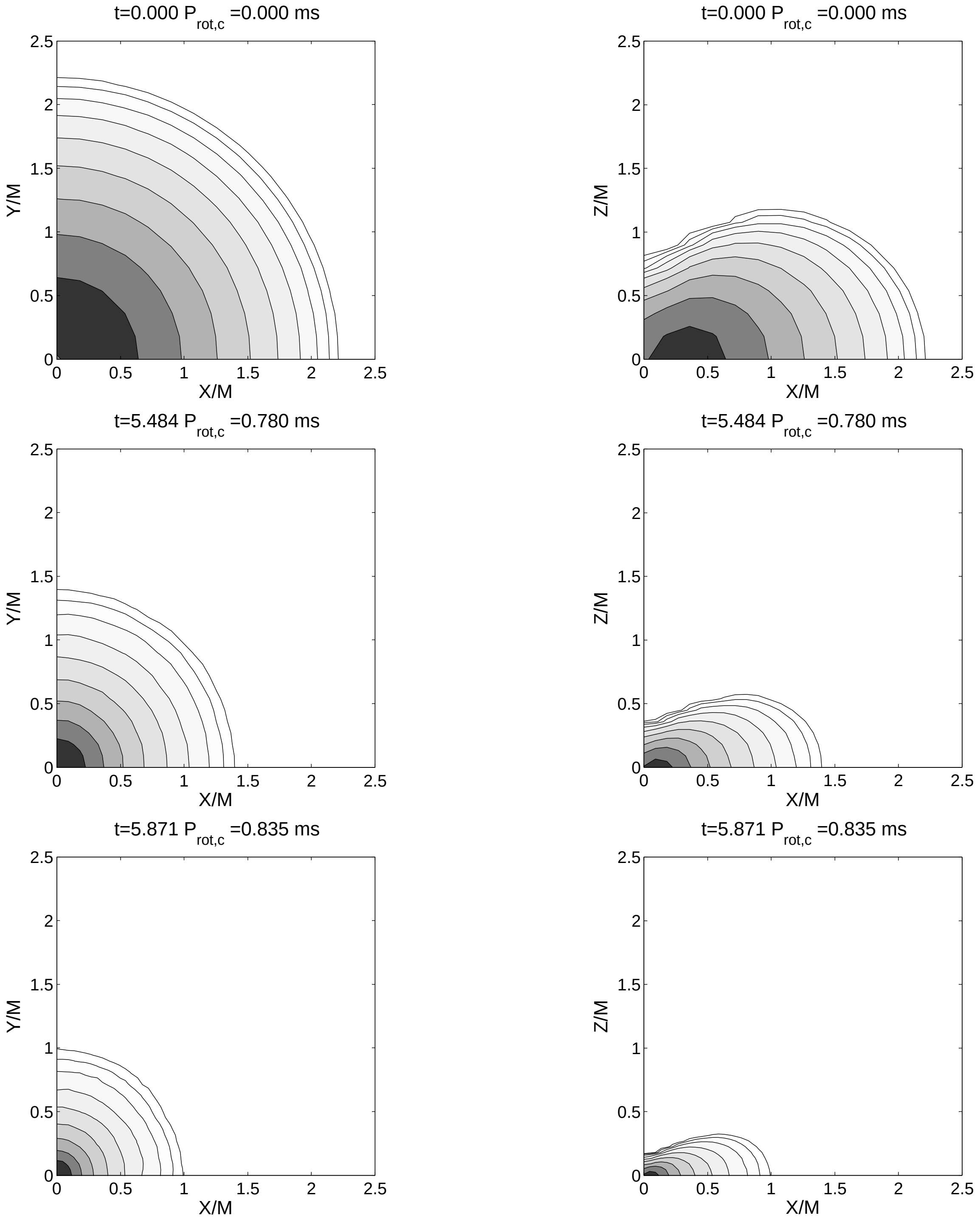

Figure 4.5 Snapshots of the rest-mass density ρ in the equatorial plane (left column) and in the xz plane (right column) for model A2. The contour lines are drawn for $\rho = 10^{-(0.2j+0.1)}\max(\rho)$ for $j = 0, 1, \ldots, 8$. Time is normalized to the initial central rotation period of the star, $P_{rot,c} = 13M$. Time in ms is rescaled to $K = 100$.

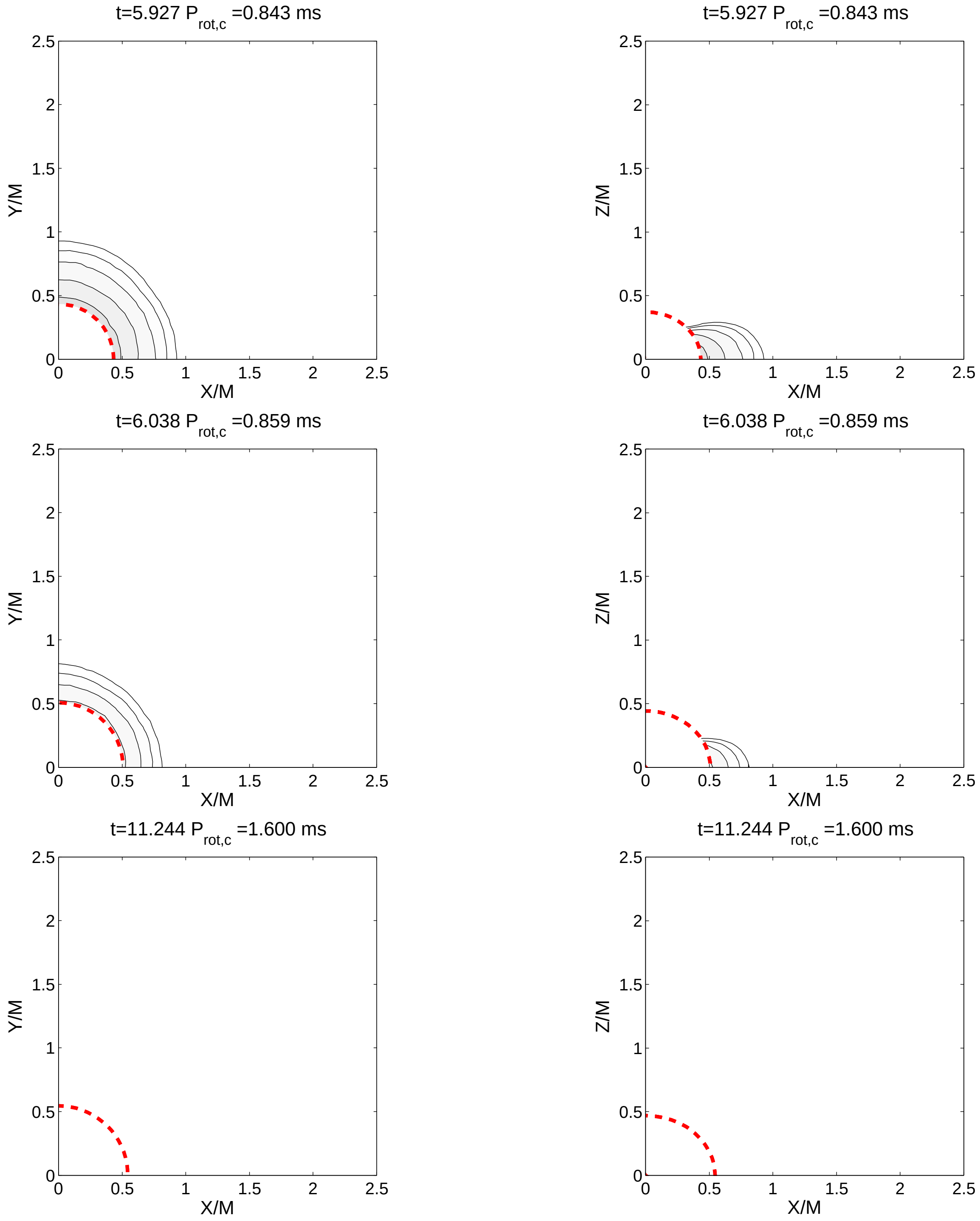

Figure 4.6 Snapshots of the rest-mass density ρ in the equatorial plane (left column) and xz plane (right column) for model A2 after an apparent horizon is found. The contour lines are drawn for $\rho = 10^{-(0.2j+0.1)}\rho_{\max}$ for $j = 0, 1, \ldots, 8$ where $\rho_{\max}$ is the maximum of ρ at time $t = 5.9P_{rot,c}$ when the apparent horizon (dashed line) is formed. Time is normalized to the initial central rotation period of the star, $P_{rot,c} = 13M$. Time in ms is rescaled to $K = 100$.

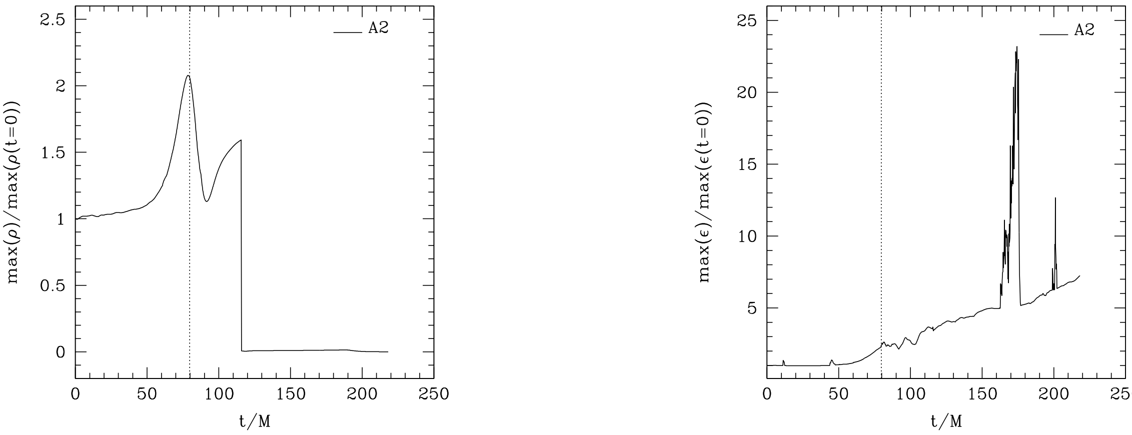

Figure 4.7 Maximum of the rest-mass density ρ and specific internal energy ϵ normalized to their initial values for model A2. The vertical dotted line denotes the time at which the apparent horizon is formed.

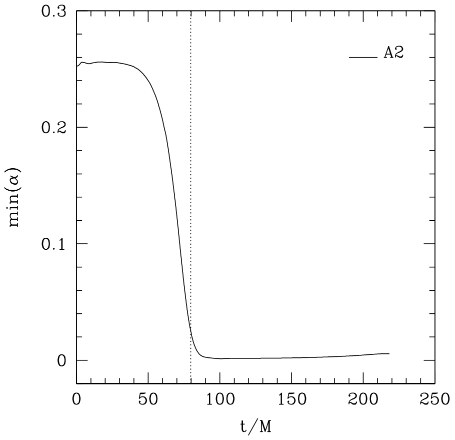

Figure 4.8 Minimum of the lapse function α for model A2. The vertical dotted line denotes the time at which the apparent horizon was found.

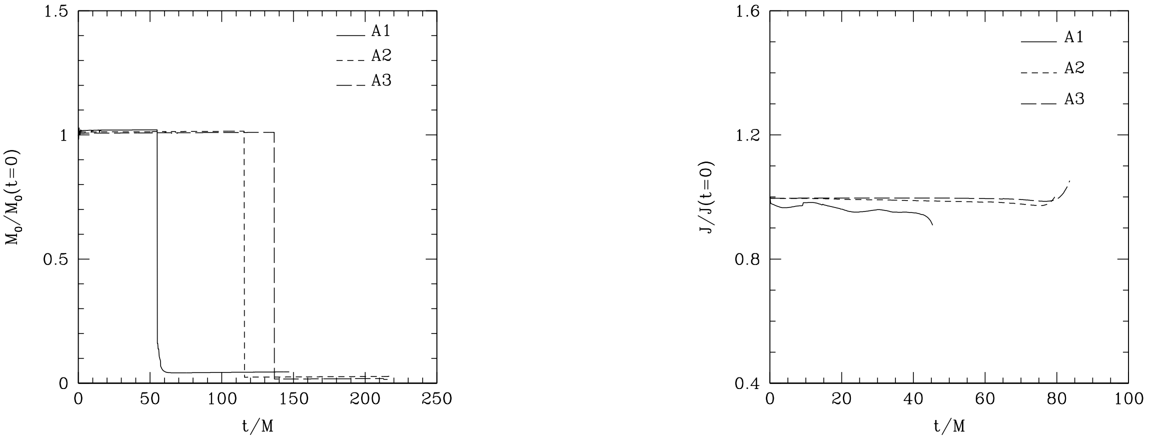

Figure 4.9 Total rest mass M_0 and angular momentum J normalized at $t = 0$ for the three different models A1 (solid line), A2 (short dashed line) and A3 (long dashed line). The angular momentum is shown until the formation of the AH.

into four small clumps (see the snapshot at time $t = 0.373P_{rot,c}$ in figure 4.10) whose formation was observed also in ref. [48]. We have also extracted the Fourier modes of the rest-mass density ρ by computing azimuthal averages using the numerical equivalent of

$$k_m \equiv \int_{z=0} \rho(\varpi\cos(\phi), \varpi\sin(\phi))e^{im\phi}d\phi \tag{4.3}$$

where $\varpi \equiv \sqrt{x^2 + y^2}$. The mode power P_m is then simply given by

$$P_m \equiv \frac{1}{\varpi_{out} - \varpi_{in}} \int_{\varpi_{in}}^{\varpi_{out}} |k_m| \mathrm{d}\varpi \tag{4.4}$$

where ϖ_{in} and ϖ_{out} are chosen to cover the whole domain (see also ref. [38]). The presence of a $m = 4$ mode at the beginning can be then seen looking also at the modes' power plotted in figure 4.11 but it is not clear at the moment whether the fragmentation has to be considered physical or simply related to the use of a Cartesian grid. Truelove *et al.* [148] have proved that spurious fragmentation can occur if the Jeans length is not well resolved, *i.e.* if the ratio $\Delta x/\lambda_J$ is greater than 0.25. The Jeans length λ_J is given by

$$\lambda_J \approx \sqrt{\left(\frac{\pi c_s^2}{\rho}\right)} \tag{4.5}$$

where c_s is the sound speed. Duez *et al.* [48] estimated the minimum of the Jeans length to be $\lambda_J \approx 1.3M$ for a model similar to our model B1 and using a polytropic EOS (for an ideal EOS, as the one used in our simulations, c_s^2 is larger). In their simulation the value of $\Delta x/\lambda_J$ was then lower than 0.25 (this is also true in our case) and so they claimed that this fragmentation is physical and it is due to physical nonaxisymmetric instabilities. In ref. [148] the "Jeans" condition $\Delta x/\lambda_J < 0.25$ was reported as necessary but not in general sufficient to avoid the formation of spurious fragmentation. Even if the resolutions used in our simulation and in the one reported in ref. [48] respect the "Jeans" condition, we think that the origin of this $m = 4$ mode is due to the use of a Cartesian grid. Further investigations with higher resolutions and different systems of coordinates will be necessary in order to verify this statement.

At time $t \approx 1.5P_{rot,c}$ the four fragments merge and a new collapse and bounce follows with the formation of a new torus. The effects of these bounces on the maximum of the rest-mass density ρ and specific internal energy ϵ are shown in figure 4.12. At $t \approx 1.6P_{rot,c}$ the torus collapses toward the center forming a new configuration which does not collapse further; even if at this time the loss of angular momentum is of the order of 10% (see figure 4.13), the star does not collapse to a black hole but starts to develop a barmode instability. At this point the model seems to have reached a new stable configuration as one can easily see from the world-line of the maximum of the rest-mass density ρ (fig. 4.14) and from its evolution (fig. 4.12, left panel).

The loss in the angular momentum cannot be accounted for by the emission of gravitational waves and it represents a numerical error probably related to the loss of mass through the external boundaries. What is interesting is that we were not able to force this model to collapse to a black-hole even if we reduced the pressure by 99% and the loss of angular momentum at the end is about 30%. This seems to confirm that supra-Kerr models are stable and cannot collapse to a black hole.

4.5 Gravitational-wave emission

We now concentrate on the emission of gravitational waves from the sub-Kerr and supra-Kerr models with the aim of comparing our results with those obtained in ref. [17] for the collapse of uniformly rotating neutron stars.

4.5.1 Sub-Kerr Models

While several different methods are possible for the extraction of the gravitational-radiation content in numerical spacetimes, we have adopted a gauge-invariant approach in which the spacetime is matched with the non-spherical perturbations of a Schwarzschild black hole (see refs. [126, 33] for applications to Cartesian coordinates grids). In practice, a set of "observers" is placed on 2-spheres of fixed coordinate radius $r_{\rm ex}$, where they extract the gauge-invariant, odd $Q^{(\rm o)}_{lm}$ and even-parity $\Psi^{(\rm e)}_{lm}$ metric perturbations [108, 111, 112].

In figure 4.15 we show the even and odd parity perturbation

$$Q^{+}_{lm} = \lambda\Psi^{(\rm e)}_{lm} \tag{4.6}$$

$$Q^{\times}_{lm} = \lambda Q^{(\rm o)}_{lm} \tag{4.7}$$

where $\lambda \equiv \sqrt{2(l+2)!/(l-2)!}$, for the $l = 2, 3, 4, 5$ modes extracted at a radius $r = 40.4M$ for model A2. Being the collapse essentially axisymmetric the modes with $m \neq 0$ are essentially zero and they are not shown here. In the first panel of figure 4.15 we also

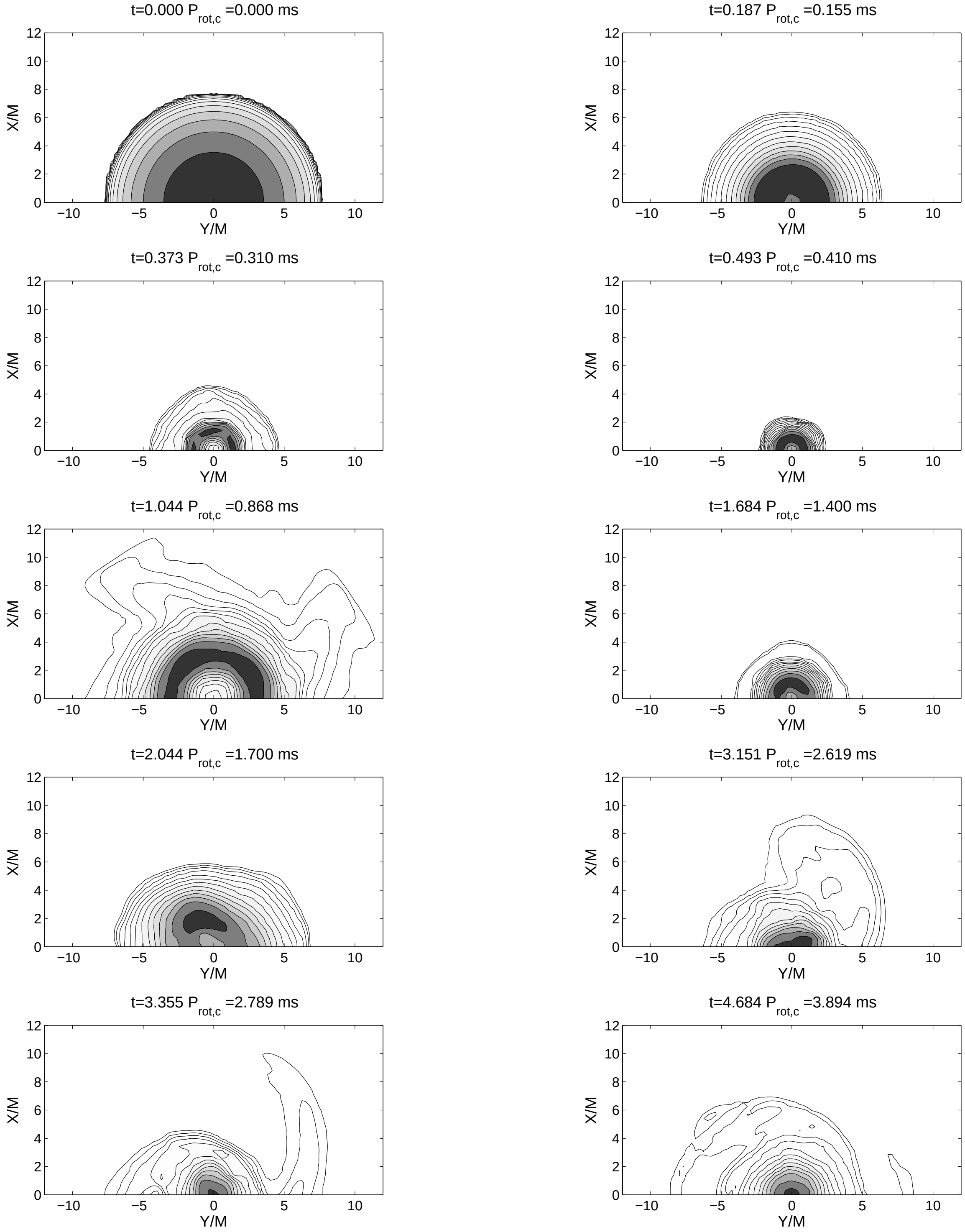

Figure 4.10 Snapshots of the rest-mass density ρ in the equatorial plane for model B1. The contour lines are drawn for $\rho = 10^{-(0.2j+0.1)}\max(\rho)$ for $j = 0, 1, \ldots, 12$. Time is normalized to the initial central rotation period of the star, $P_{rot,c} = 89M$. Time in ms is rescaled to $K = 100$.

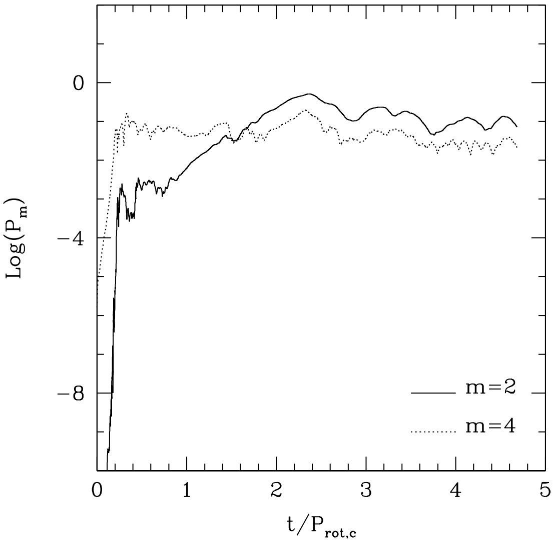

Figure 4.11 Logarithm of modes' power versus time for model B1. The modes not shown in this plot are zero during all the evolution.

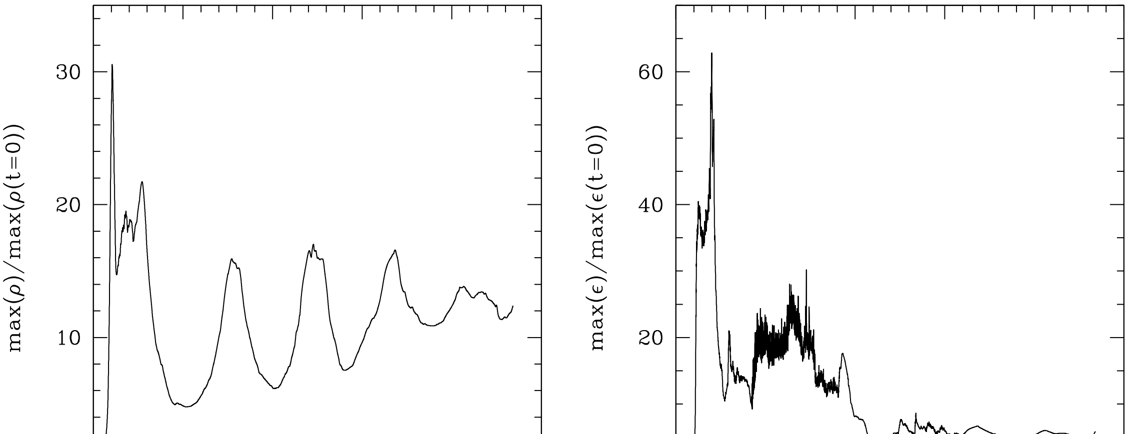

Figure 4.12 The maximum value of ρ and ϵ during the evolution of star B1.

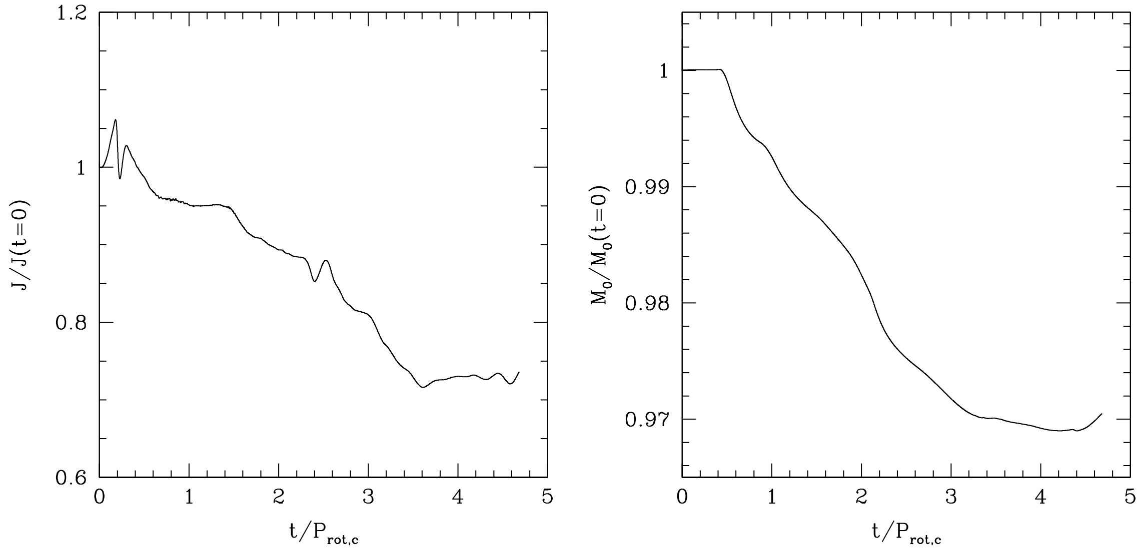

Figure 4.13 Total angular momentum J and total rest mass M_0 normalized at $t = 0$ for model B1.

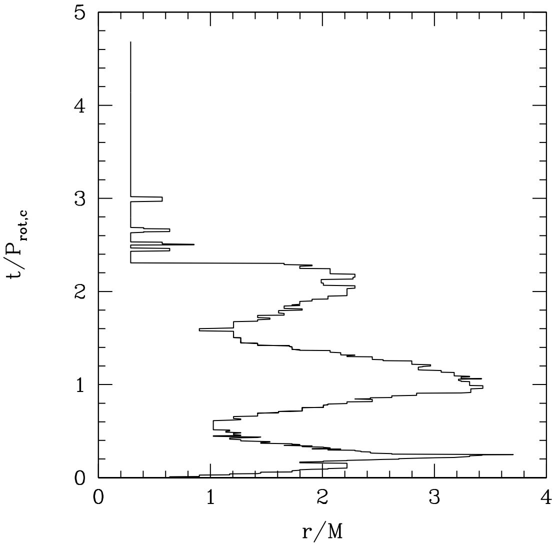

Figure 4.14 World-line of the maximum of the rest-mass density ρ for model B1. The final configuration has a maximum located at a radius smaller than the initial one. Note also the three bounces.

compare the signal obtained at different radii in order to verify that we are sufficiently far-away from the star, *i.e.* in the *wave zone*.

The same quantities are plotted also for the other two sub-Kerr models A1, in fig. 4.16, and A3, in fig. 4.17, while in fig. 4.18 we show all the data together. From these plots and especially from fig. 4.18 one can see how the amplitude of the gravitational-wave signal increases with the degree of differential rotation. For example between model A1 (first row of figure 4.18), which has $\hat{A} = 0.6$, to model A3 (last row of figure 4.18) the amplitude of mode $l = 2, m = 0$ decreases of one order of magnitude.

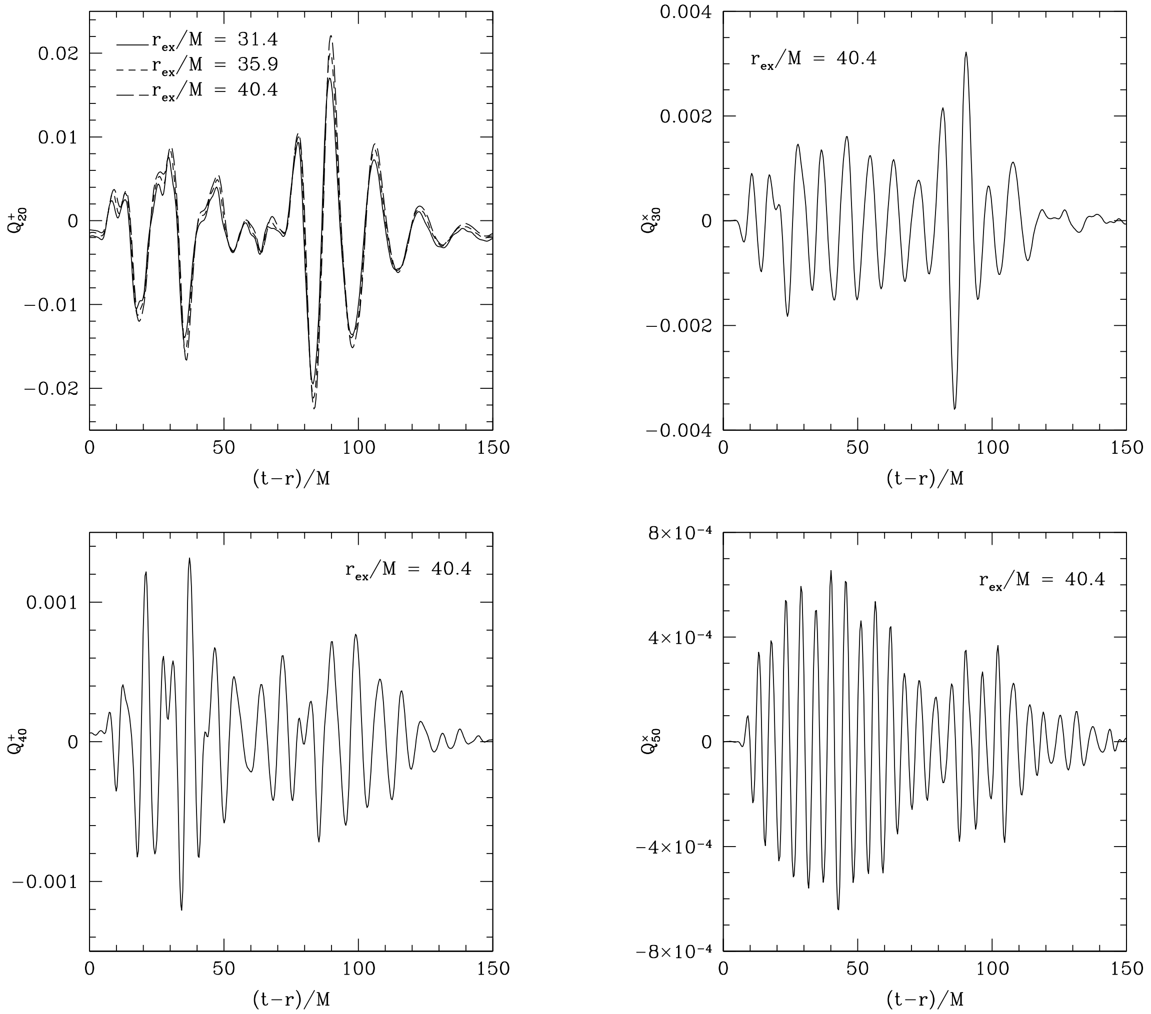

Figure 4.15 Even and odd parity perturbation for $l = 2$ (top left panel), $l = 3$ (top right), $l = 4$ (bottom left), $l = 5$ (bottom right) and $m = 0$ for model A2. In the top left panel different lines represent different detectors; the good agreement between all of them demonstrates that our extraction is done in the wave zone.

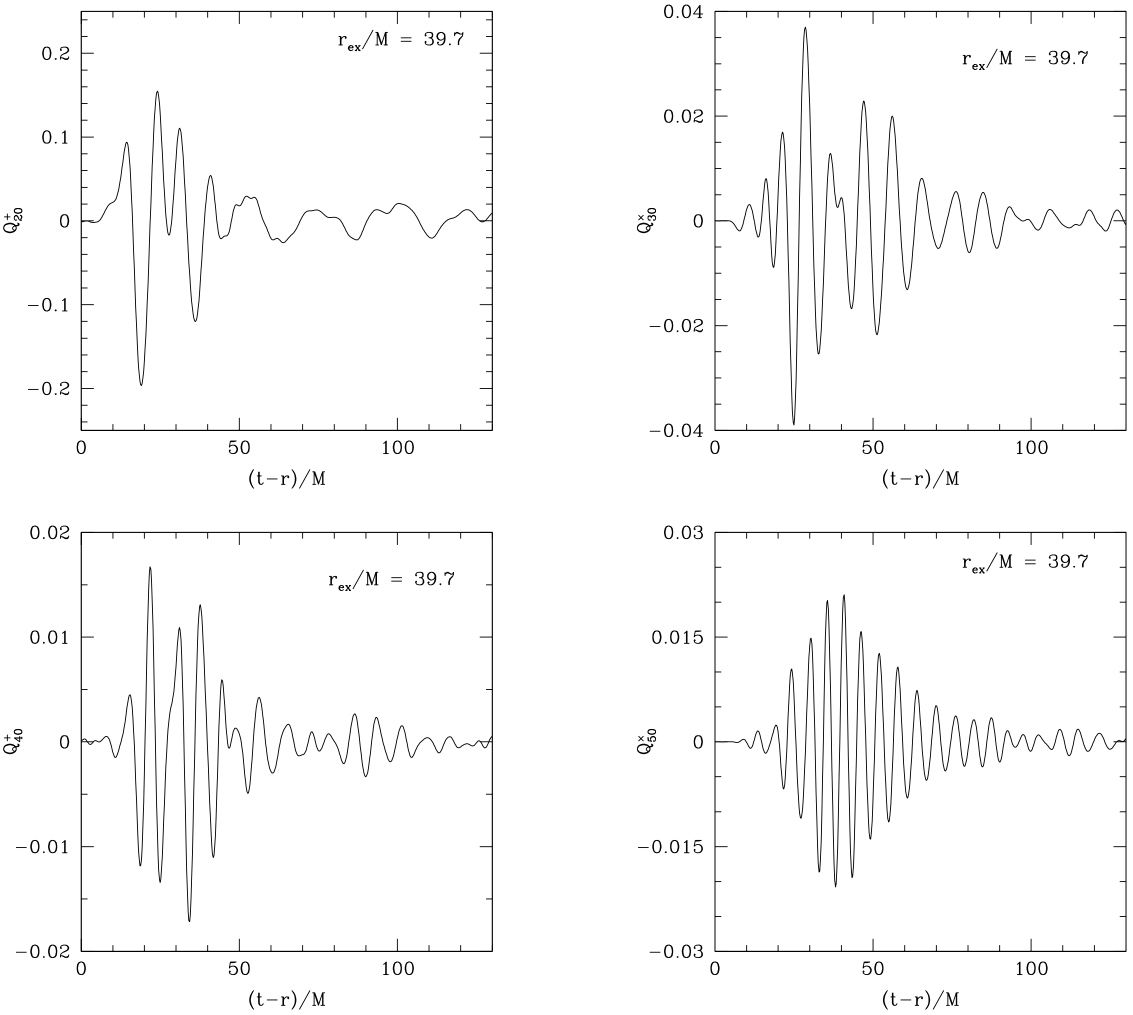

Figure 4.16 Even and odd parity perturbation for $l = 2, 3, 4, 5$ and $m = 0$ for model A1.

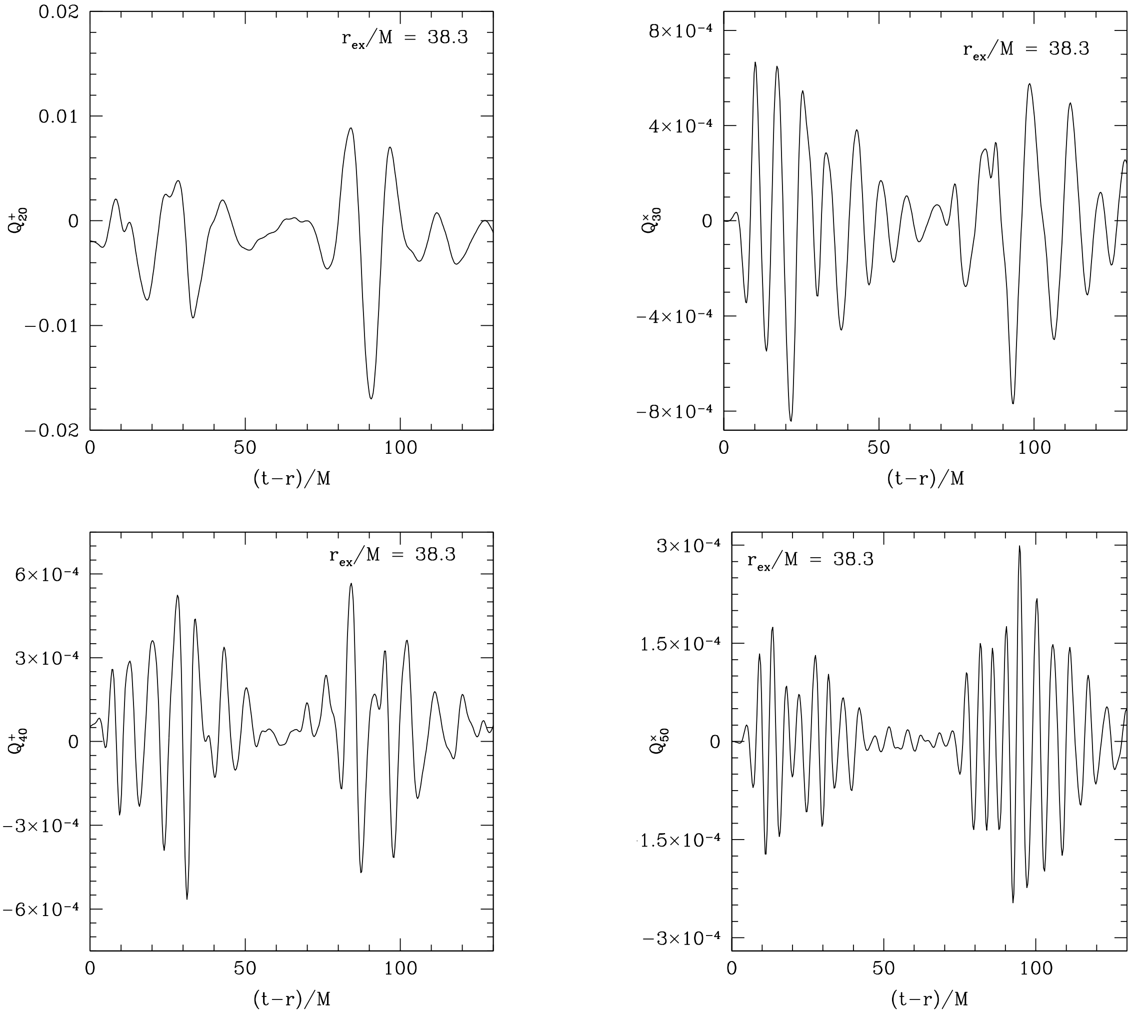

Figure 4.17 Even and odd parity perturbation for $l = 2, 3, 4, 5$ and $m = 0$ for model A3.

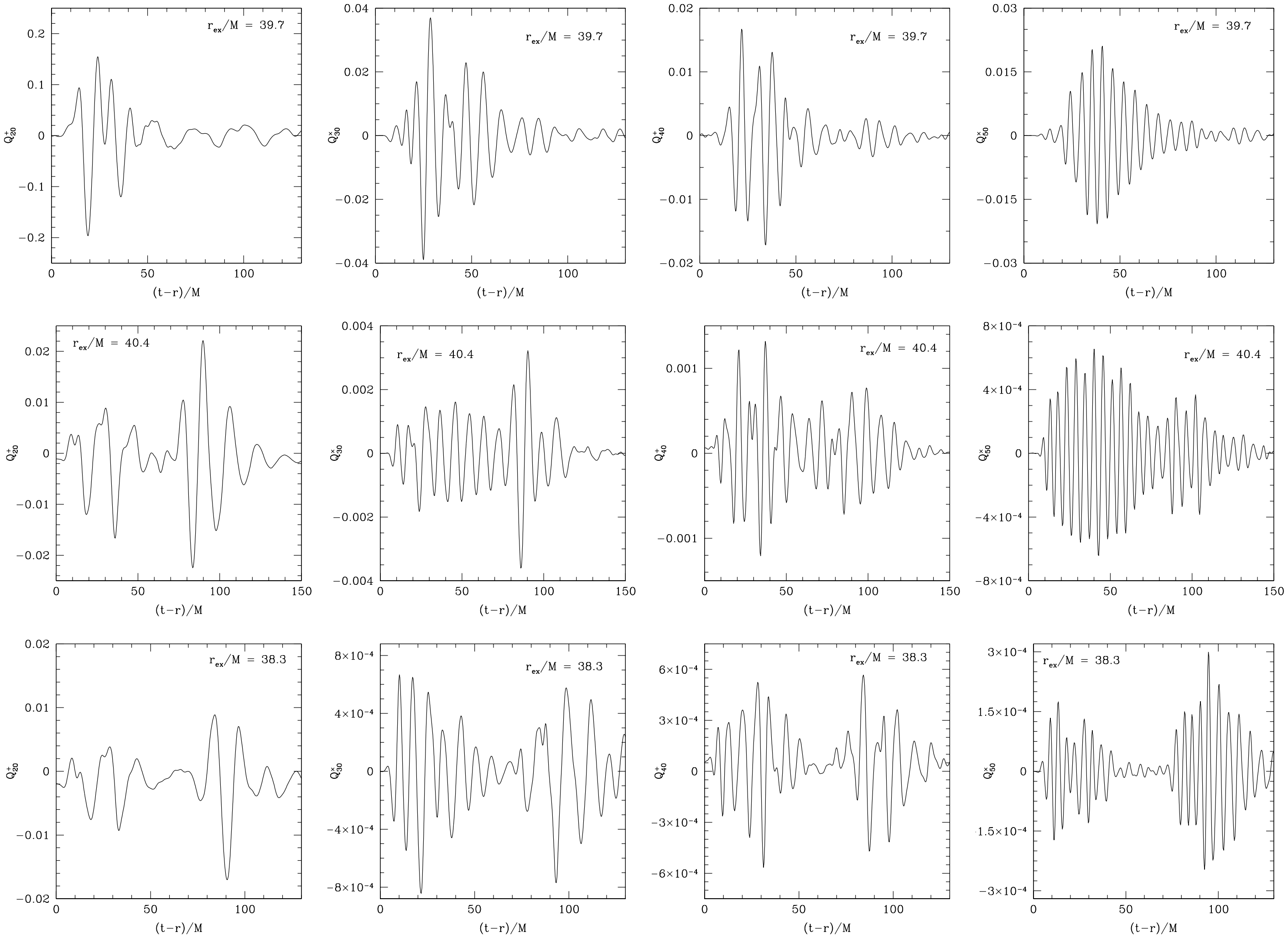

Figure 4.18 Even and odd parity perturbation for $l = 2, 3, 4, 5$ and $m = 0$ for all the sub-Kerr models. In the first row model A1, in the second one A2 and in the third one A3.

Using these quantities it is also possible to compute the gravitational-wave amplitudes in the two polarizations h_+ and $h_\times$ as

$$h_+ - \mathrm{i}h_\times = \frac{1}{2r}\sum_{l,m}\left(Q^+_{lm} - \mathrm{i}\int_{-\infty}^{t} Q^\times_{lm}(t')dt'\right) {}_{-2}Y^{lm}, \tag{4.8}$$

where ${}_{-2}Y^{lm}$ is the $s = -2$ spin-weighted spherical harmonic.

In fig. 4.19 we show h_+ and $h_\times$ for model A2 extracted at a distance $r = 40.4M = 11.4R_{eq}$, where R_{eq} is the equatorial radius of the star at $t = 0$. Comparing with the waveforms reported in ref. [17] we see that the amplitudes are higher by a factor 10. This was expected as the amplitude of gravitational waves seems to increase with the ratio of J/M^2. Also the energy carried away from the system by gravitational waves is higher: $\Delta E/M \approx 2.9 \times 10^{-4}$.

In figure 4.20 we plot the power spectrum density of the two polarizations; the h_+ shows two peaks, one at around 4.3kHz and the other one at around 5.7kHz. In order to compare these values with those obtained in ref. [17] we have rescaled these frequencies by the factor $1/\sqrt{K}$, where $K = 100$ is the value of the polytropic constant used in ref. [17], while we remind that we used $K = 1$ (polytropic units, see ref. [35] for scaling to arbitrary K) to build our initial models. Considering the optimal sensitivity of VIRGO we can also set an upper limit for the characteristic amplitude produced in the collapse of differentially rotating NS at 10kpc to be $h_c = 2.97 \times 10^{-19}(M/M_\odot)$ at a characteristic frequency $f_c = 5280$Hz. The signal-to-noise ratio is $S/N \approx 12.4$. In the case of LIGOI we obtain $h_c = 2.95 \times 10^{-19}(M/M_\odot)$ at $f_c = 5095$Hz with $S/N \approx 7.2$ while for advanced LIGO we have $h_c = 2.01 \times 10^{-19}(M/M_\odot)$ at $f_c = 3863$Hz with $S/N \approx 55.4$. Interestingly these amplitudes and SNR are $2-3$ order of magnitudes larger than the ones reported in ref. [17] for uniformly rotating stars. In fig. 4.21 we finally report the energy carried away by gravitational waves $\Delta E/M$ for all the three models as a function of $\hat{A}$ and of J/M^2.

4.5.2 Supra-Kerr Model

As the position of the boundary is still too close to the source, we were not able to extract the gravitational-wave signal in the wave zone as done in the previous section but we have simply computed some estimates using the standard quadrupole [106] formula. In this approximation the observed wave-form and amplitude for the two polarization for an observer situated at infinity along the z-axis are approximately given by

$$\begin{aligned} h_+ &= \frac{\ddot{I}^{xx}(t) - \ddot{I}^{yy}(t)}{r} \\ h_\times &= 2\,\frac{\ddot{I}^{xy}(t)}{r} \quad , \end{aligned} \tag{4.9}$$

where

$$I^{jk} = \int d^3x \; D \; x^j x^k \; . \tag{4.10}$$

is the quadrupole moment of the matter distribution. The results for the gravitational-wave amplitudes h_+ and $h_\times$ are finally reported in figure 4.22.

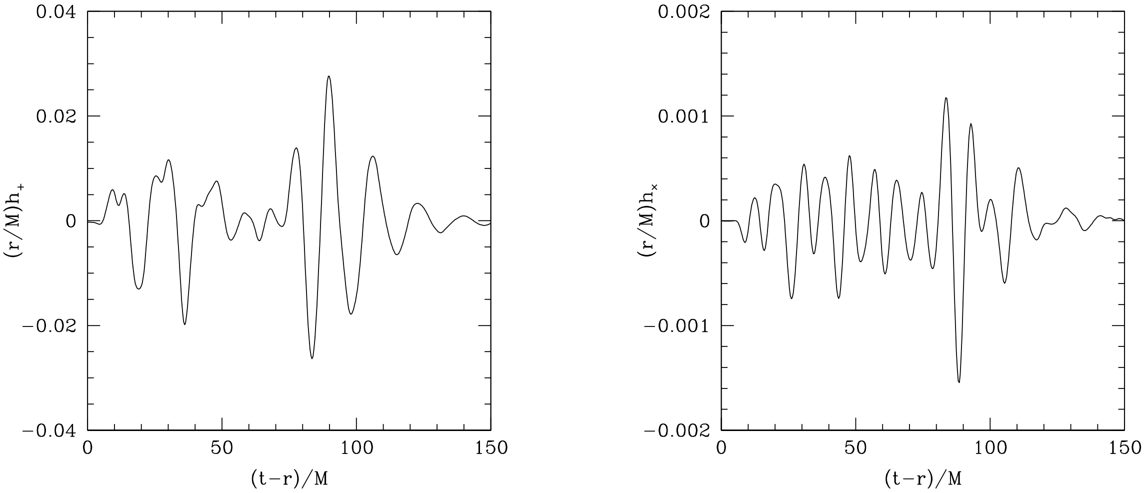

Figure 4.19 The gravitational-wave amplitudes h_+ and $h_\times$ for the collapse of model A2 extracted at a radius $r = 40.4M$.

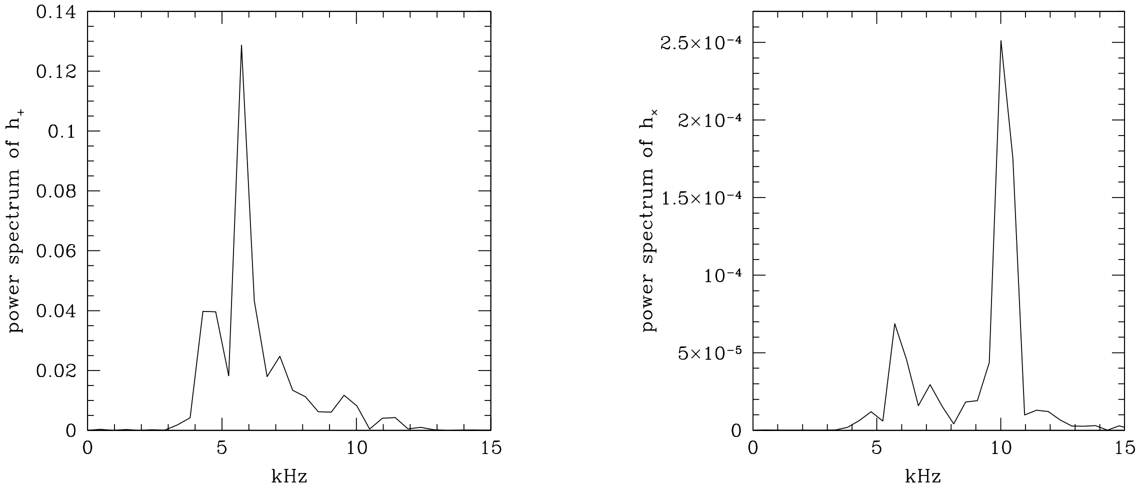

Figure 4.20 Power spectrum of h_+ (left panel) and $h_\times$ (right panel) for the collapse of model A2 extracted at a radius $r = 40.4M$. These quantities are rescaled by a factor $1/\sqrt{K}$, where $K = 100$ is the value of the polytropic constant used in ref [17] to build their initial models.

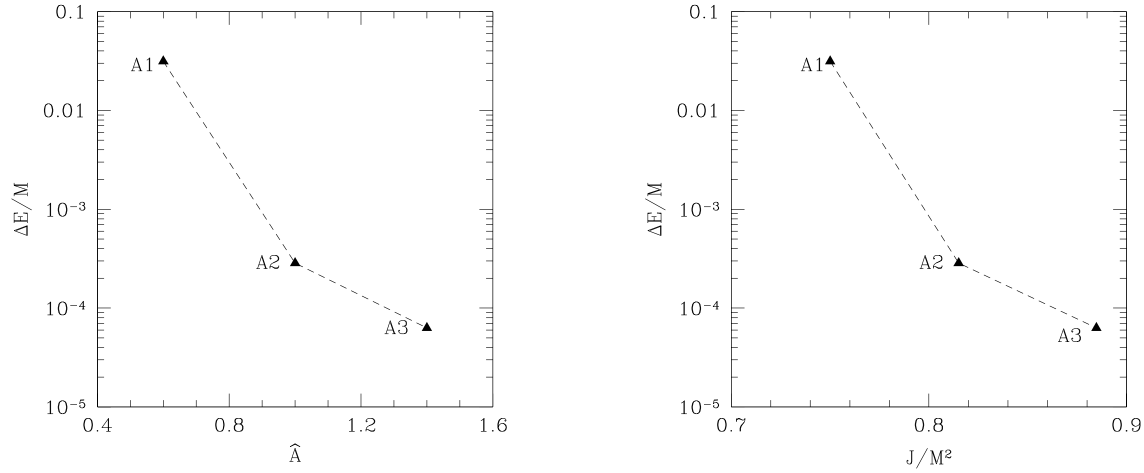

Figure 4.21 The energy $\Delta E/M$ carried away by gravitational waves during the collapse of the three sub-Kerr models as a function of the degree of differential rotation $\hat{A}$ (left panel) and of J/M^2 (right panel). We recall that for $\hat{A} \to \infty$ uniform rotation is recovered.

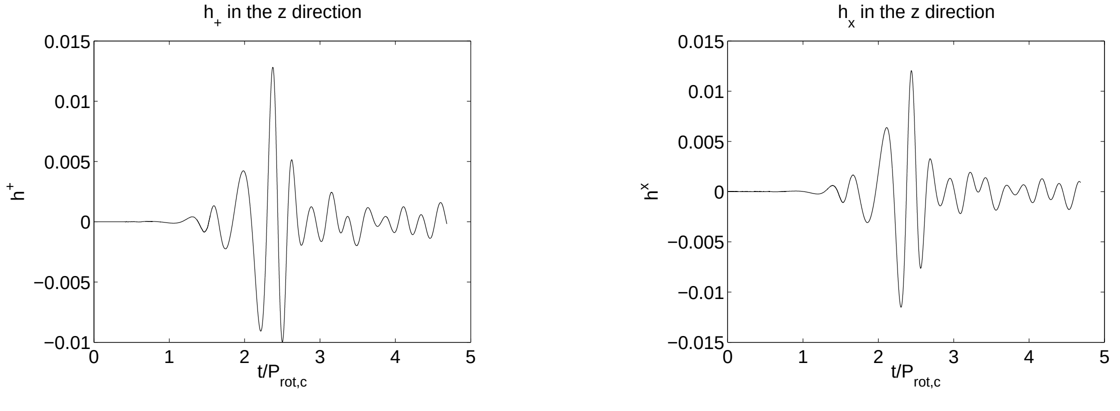

Figure 4.22 The gravitational-wave amplitudes h_+ and $h_\times$ for the collapse of model B1 computed with the quadrupole formula.

4.6 Summary

We have presented here new results about the collapse of differentially rotating neutron stars. We confirm that black holes are formed only in the collapse of sub-Kerr models and not for supra-Kerr. We especially performed a detailed study of the initial configurations in order to study the properties of the unstable models and we found that they are all sub-Kerr while we were not able to find supra-Kerr unstable models.

For the first time, thank to the use of the `Whisky` code and of fixed and progressive mesh refinement techniques, we were also able to extract the gravitational-wave signal from the sub-Kerr models that as expected revealed to be much stronger that the one emitted by uniformly rotating stars. We have indeed found that differential rotation can increase considerably the energy emitted making these sources much more interesting because detectable at large distances. For these reasons, we consider these models important sources for gravitational waves detectors even at their current sensitivity.

Anyway a more detailed study including more realistic equations of state and magnetic fields is necessary in order to predict a more realistic signal. Magnetic fields can indeed strongly affect the dynamics of these objects reducing the degree of differential rotation and so reducing the gravitational waves amplitudes.

Chapter 5

The exact solution of the Riemann problem in relativistic MHD

5.1 Introduction

As already pointed out in Chapter 3, high-resolution shock-capturing schemes are based on the numerical solution of Riemann problems at the interfaces between each numerical cell. It is then natural that Riemann problems have assumed an important role in the testing of numerical codes based on HRSC schemes. Clearly, to have an idea of the accuracy of a numerical algorithm one needs to compare the numerical results with the exact ones. In both Newtonian and relativistic hydrodynamics this was already possible and, for example, the exact solution of the Riemann problem in relativistic hydrodynamics was used to test the `Whisky` code [15]. In the case of magnetohydrodynamics however the exact solution was found only quite recently in the Newtonian case while no general solution was available in relativistic MHD when we started to think about the development of our `WhiskyMHD` code.

A direct and important consequence of the absence of an exact solution is that the validation of modern complex relativistic MHD codes for the most elementary and yet demanding tests has not been made in a quantitative manner for generic initial conditions. Rather, it has taken place through the qualitative comparison with the large set of test-problems in relativistic MHD meticulously collected over the years (see, for instance, ref. [84] and ref. [20]). It should be recognized, however, that for non-generic initial states it is sufficient to have exact solutions for MHD shocks and rarefactions as this covers all types of basic hyperbolic waves of the system and indeed exact solutions of this type were used by Komissarov [84] for quantitative testing.

On the other hand, the purpose of this work is to present the procedure for the exact solution of the Riemann problem in relativistic MHD with generic initial conditions. Our approach considers both initial states with a zero component of the magnetic field along the flow and leading to a set of only three waves analogous to the ones in relativistic hydrodynamics, as well as generic initial states leading to the full set of seven MHD waves. The approach discussed for the numerical solution is based on a "hybrid" approach which adopts different sets of equations according to the values of the normal magnetic field and that has turned out to be crucial for a successful solution.

The exact solution presented here is now a standard tool used by several groups in the world to test both special and general relativistic MHD codes. Even if the use of this solution inside numerical codes would improve their accuracy, it is still limited by its high computational cost.

5.2 A short review of the Riemann problem

As first formulated by Riemann more than a hundred years ago, the solution of the one-dimensional Riemann problem in hydrodynamics consists of determining the temporal evolution of a fluid which, at some initial time, has two adjacent uniform states characterized by different values of uniform velocity, pressure and density. These initial conditions completely determine the way in which the discontinuity will decay after removal of the barrier separating the initial "left" and "right" states.

In general, the Riemann problem requires the solution of a nonlinear algebraic system of equations written as a function of a single unknown quantity (*e.g.* the total pressure at the contact discontinuity in purely hydrodynamical problems). With the exception of few trivial initial configurations, the solution of the Riemann problem cannot be obtained analytically but requires a numerical approach. The solution found in this way is referred to as the *"exact"* solution of the Riemann problem, to distinguish it from the *"approximate"* solution of the Riemann problem, which is instead obtained when the system of equations is reduced to a locally-linear form (an exhaustive discussion of approximate Riemann solvers can be found in ref. [143]). It is therefore useful to stress that although named "exact", the solution of the Riemann problem is necessarily obtained with a small but nonzero truncation error.

The exact solution of the Riemann problem in relativistic hydrodynamics has been obtained only rather recently and was proposed by Martí *et al.* [100] for flows that are purely along the direction normal to the initial discontinuity. This work has then been extended to the case in which tangential velocities are present ([116]) and improved in efficiency by exploiting the relativistic invariant relative velocity between the two states to predict the wave pattern produced ([122] and [123]). The relevance of these calculations has not been restricted to fundamental issues of relativistic hydrodynamics. Quite the opposite, these solutions have been of great importance for the testing of complex multidimensional codes implementing High Resolution Shock Capturing methods, and that are based on the approximate or exact solution of Riemann problems at the interfaces between the numerical cells ([93]). These codes have then been used in various simulations in either fixed ([9, 58, 163]) or dynamical spacetimes ([48, 132, 16]).

This intense and recent development of numerical codes for the solution of the relativistic hydrodynamic equations has been accompanied by an equally intense development of codes solving the equations of magnetohydrodynamics in relativistic regimes. The reason behind this activity is the widespread expectation that strong magnetic fields are crucial in the study and explanation of several puzzling astrophysical phenomena such as relativistic jets or γ-ray bursts. As a result, and in the hope of clarifying issues in relativistic astrophysics which cannot be described satisfactorily through analytic techniques, several groups have recently constructed numerical codes solving the equations of relativistic MHD on either fixed spacetimes (see, for example, ref. [42] and ref. [84] for a flat background and refs. [64, 39, 86, 107, 61, 12] for a black-hole background) or in fully dynamical spacetimes ([47, 131]).

Just like their hydrodynamical counterparts, some of these codes are based on the solution of a local Riemann problem suitably formulated for a magnetized fluid, and all are meant to be used for ultrarelativistic flows. However, unlike their hydrodynamical counterparts, these codes cannot benefit from the comparison with the exact solution of the Riemann problem in relativistic MHD. The literature on the Riemann problem in MHD is, in fact, much more limited and a general exact solution was found rather recently and for a Newtonian fluid only ([127, 53]). The background knowledge in this area is even more scarce for a relativistic fluid and while no general exact solution has been proposed yet, recent work has been made to derive an exact solution in the particular case in which the magnetic field of the initial states is tangential to the discontinuity and orthogonal to the fluid velocity ([125]). Besides having a larger set of equations when compared to the corresponding problem in relativistic hydrodynamics, a considerable addition to the complexity of the Riemann problem in relativistic MHD is represented by the fact that the mathematical structure of the problem itself is modified and the system of equations is no longer strictly hyperbolic ([95]). The possibility of having coincident eigenvalues poses the question of the uniqueness of the solutions and this represents then a problem within the problem. As we will comment also later on, a lively debate on these issues is presently ongoing and progress is starting to be made, although first results are known in Newtonian MHD only (see ref. [145]). Because the focus of this work is the exact solution of the Riemann problem in relativistic MHD as an aid to the development of numerical codes, hereafter we will adopt the *working assumption* that the Riemann problems considered here have a solution and that this solution is unique. Clearly, this hypothesis avoids the issue rather than solving it, but it allows for a marked progress at least in those cases in which compound waves are not found in numerically approximate solutions.

5.3 Equations of Special Relativistic MHD

Consider an ideal magnetized relativistic fluid with an energy-momentum tensor given by

$$T^{\mu\nu} = (\rho + \rho\epsilon + p_{\rm g} + 2p_{\rm m})\, u^{\mu}u^{\nu} + (p_{\rm g} + p_{\rm m})\, \eta^{\mu\nu} - b^{\mu}b^{\nu} \ , \tag{5.1}$$

where ρ is the rest mass density, ϵ the specific internal energy, $p_{\rm g}$ the gas pressure [1], $p_{\rm m}$ the magnetic pressure, $u^{\mu} \equiv W(1, v^x, v^y, v^z)$ the four-velocity, $W \equiv 1/\sqrt{1 - v^i v_i} = 1/\sqrt{1 - v^2}$ the Lorentz factor and the 4-vector $\boldsymbol{b}$ has components

$$b^{\alpha} \equiv \left\{ W(\vec{v} \cdot \vec{B}), \frac{\vec{B}}{W} + W(\vec{v} \cdot \vec{B})\vec{v} \right\} \ . \tag{5.2}$$

---

[1] In this chapter, and only in this one, we will use p to denote the total pressure given by the sum of the gas pressure $p_{\rm g}$ and of the magnetic pressure $p_{\rm m}$.

Here $\vec{B}$ is the magnetic field 3-vector and

$$b^2 \equiv b^i b_i = \frac{B^2}{W^2} + (\vec{v}\cdot\vec{B})^2 = 2p_{\rm m} \ . \tag{5.3}$$

The equations of special relativistic MHD are then obtained after requiring the conservation of baryon number

$$\partial_\mu(\rho u^\mu) = 0 \ , \tag{5.4}$$

the conservation of energy and momentum

$$\partial_\mu T^{\mu\nu} = 0 \ , \tag{5.5}$$

together with the relevant pair of Maxwell equations. If the fluid is assumed to have an infinite electrical conductivity (*i.e.* ideal MHD limit), the Maxwell equations reduce to $\partial_{[\alpha}F_{\beta\gamma]} = 0$, where $\boldsymbol{F}$ is the Faraday tensor and the square brackets refer to antisymmetrised indices. Using the definition (5.2), the Maxwell equations can be written as

$$\partial_\mu(b^\mu u^\nu - u^\mu b^\nu) = 0 \ . \tag{5.6}$$

The system of equations (5.4)–(5.6) is completed with an equation of state relating the pressure to the rest-mass density and/or to the energy density. Although hereafter we will use an ideal-gas EOS, $p_{\rm g} = \rho\epsilon(\Gamma - 1)$, the procedure described for the solution of the Riemann problem is valid for a generic EOS.

We assume that the system (5.4)–(5.6) has a planar-symmetry, *i.e.* that in a Cartesian coordinate system (t, x, y, z) all the variables depend only on t and x. In this case, the complete set of MHD equations can be written as a set of first-order partial differential equations in a flux-conservative form

$$\frac{\partial \mathbf{U}}{\partial t} + \frac{\partial \mathbf{F}}{\partial x} = 0 \ , \tag{5.7}$$

where $\mathbf{U}$ and $\mathbf{F}$ are respectively the vectors of conserved quantities and fluxes, defined as

$$\mathbf{U} \equiv \begin{pmatrix} D \\ \tau - b^0 b^0 \\ S^x - b^0 b^x \\ S^y - b^0 b^y \\ S^z - b^0 b^z \\ B^y \\ B^z \end{pmatrix} , \qquad \mathbf{F} \equiv \begin{pmatrix} D v^x \\ S^x - b^0 b^x - D v^x \\ S^x v^x + p - b^x b^x \\ S^y v^x - b^x b^y \\ S^z v^x - b^x b^z \\ B^y v^x - B^x v^y \\ B^z v^x - B^x v^z \end{pmatrix} , \tag{5.8}$$

and where the following definitions have been used

$$\begin{aligned}
\tau &\equiv wW^2 - p - D \ , && (5.9)\\
D &\equiv \rho W \ , && (5.10)\\
S^j &\equiv \rho h W^2 v^j \ , && (5.11)\\
p &\equiv p_{\rm g} + p_{\rm m} = p_{\rm g} + \frac{1}{2}b^2 \ , && (5.12)\\
w &\equiv \rho h \ , && (5.13)\\
h &\equiv h_{\rm g} + \frac{b^2}{\rho} = 1 + \epsilon + \frac{p_{\rm g}}{\rho} + \frac{b^2}{\rho} \ , && (5.14)
\end{aligned}$$

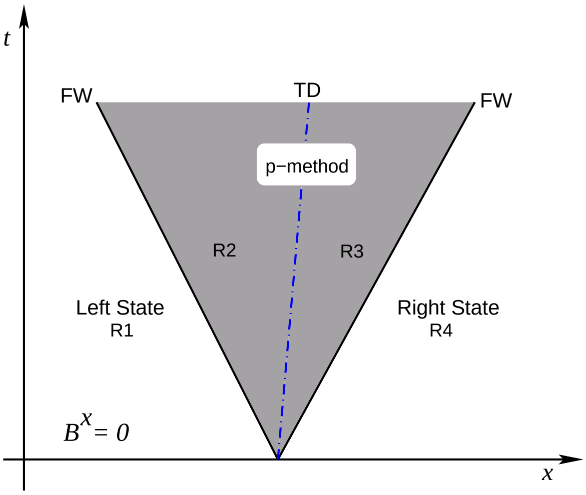

Figure 5.1 Spacetime structure of the MHD Riemann problem in the case in which the magnetic field has tangential components only, *i.e.* $B^x = 0$. The "Riemann-fan" in this case is composed of only two fast-waves (FW) and of a central tangential discontinuity (TD), thus resembling the structure of the Riemann problem in pure hydrodynamics. Indicated with R1–R4 are the 4 different regions into which the Riemann problem can be decomposed, each representing a different state.

where h is the total specific enthalpy and $h_{\rm g}$ the one of the gas only.

Note also that the divergence-free condition for the magnetic field and the Maxwell equation for the evolution of the x-component of the magnetic field imply that $\partial_t B^x = 0 = \partial_x B^x$, *i.e.* B^x is uniform in space, constant in time and thus always maintains its initial value.

5.4 Strategy of Solution

The general Riemann problem in relativistic MHD consists of a set of seven nonlinear waves: two *fast-waves* (FW), two *slow-waves* (SW), two *Alfvèn-waves* (AW), and a *contact discontinuity* (CD) at which only the density may be discontinuous. The fast and slow nonlinear waves can be either shocks or rarefaction waves, depending on the change in the pressure and in the norm of the magnetic field across the wave.

Building on the experience with relativistic hydrodynamics, our general strategy in the search for the solution consists of expressing all of the variables behind each wave as functions of the values of the same variables ahead of the wave and of an unknown variable behind the wave. When considering the Riemann problem in relativistic hydrodynamics, in fact, the solution is found after expressing all of the quantities behind the wave as functions of the value of the pressure at the contact discontinuity. In this way, the problem is reduced to the search for the value of the pressure that satisfies the jump conditions at the contact discontinuity.

When considering the Riemann problem in relativistic MHD, on the other hand, two different cases need to be distinguished. Assuming the initial discontinuity to have normal along the x-axis, the initial magnetic field in this direction can either be zero (*i.e.* $B^x = 0$) or not (*i.e.* $B^x \neq 0$). In the first case, the structure of the solution is very similar to the hydrodynamical one, with only two fast waves and a *tangential discontinuity* along which only the total pressure and the x component of the velocity are continuous. The spacetime structure of the Riemann problem in this case is sketched in Figure 5.1, where the "Riemann-fan" is shown to be composed of only two fast-waves (FW) and of a central tangential discontinuity (TD). Because of this analogy, the numerical solution of the Riemann problem when $B^x = 0$ follows the same procedure implemented in relativistic hydrodynamics. We refer to this as the "total-pressure approach" or simply, the *"p-method"*.

A detailed investigation of the exact solution of the Riemann problem with tangential magnetic fields and when the additional condition $\vec{v} \cdot \vec{B} = 0$ is imposed, has been recently proposed by Romero et al. [125]. Among the many points discussed, this work has shown that when $B^x = 0 = \vec{v} \cdot \vec{B}$ the Riemann problem in relativistic MHD can be assimilated to the one in relativistic hydrodynamics and that all of the corrections introduced by the magnetic field can be incorporated in the definition of a new, effective EOS.

In the second case, on the other hand, the Riemann problem is considerably more complex and all of the seven waves are allowed to form when the initial discontinuity is removed. The spacetime structure of the Riemann problem in this case is sketched in Figure 5.2, where the "Riemann-fan" is shown to be composed of two fast-waves (FW), of two Alfvèn waves (AW), of two slow-waves (SW) and of a central contact discontinuity (CD).

It is important to bear in mind that across the Alfvèn discontinuities only the total pressure, the gas pressure and the density are continuous, while there could be jumps in the other quantities. As a result, if the total pressure is used as unknown, there would be three different values for the total pressure (two between the fast and the slow-waves and one between the two slow-waves) but five conditions to be satisfied at the contact discontinuity: the continuity of the three components of the velocity and the continuity of the tangential components of the magnetic field. The resulting system of five equations in three unknowns is over-constrained and there is no guarantee that a global convergent solution is found at the contact discontinuity. Indeed, experience has shown that small numerical imprecisions at the level of round-off errors are in general sufficient to prevent the simultaneous solution of the five constraints.

To circumvent this difficulty and inspired by the procedure followed in the exact solution of the corresponding Riemann solver in nonrelativistic MHD ([127]), when $B^x \neq 0$ we have implemented a "hybrid" approach in which the total pressure is used as the unknown variable between the fast and the slow waves (*i.e.* in regions R2-R3, and R6-R7 of Figure 5.2), while the tangential components of the magnetic fields (B^y and B^z) are used between the slow waves (*i.e.* in regions R4-R5 of Figure 5.2). In this way, the continuity of the tangential components of the magnetic field B^y and B^z is automatically guaranteed through the contact discontinuity and only the continuity of the total pressure and of the three components of the velocity needs to be satisfied. The resulting system consists of four equations in four unknowns and, being closed, it can be solved numerically

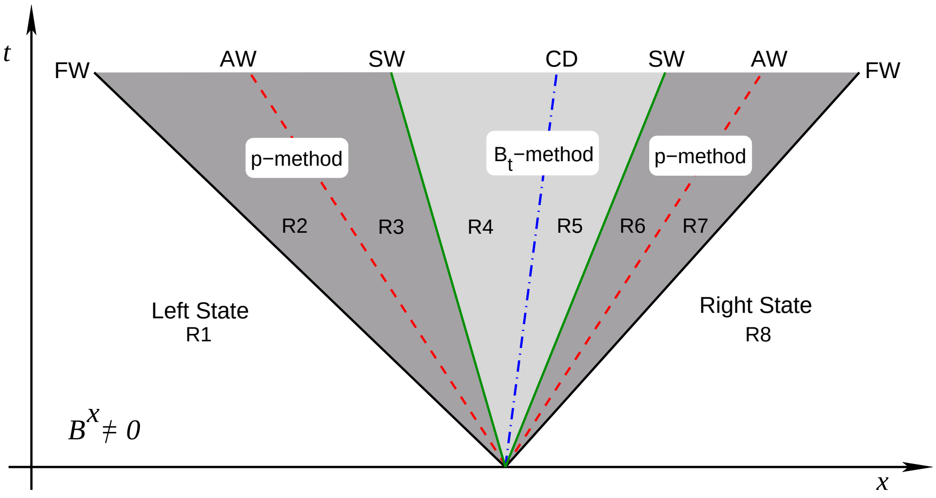

Figure 5.2 Spacetime structure of the MHD Riemann problem in the general case in which the magnetic field has also a normal component, *i.e.* $B^x \neq 0$. The "Riemann-fan" is here composed of two fast-waves (FW), of two Alfvèn waves (AW), of two slow-waves (SW) and of a central contact discontinuity (CD). Indicated with R1–R8 are the 8 different regions into which the Riemann problem can be decomposed, each representing a different state. Indicated are also the different methods used to compute the solutions in the different regions (*i.e.* B_t-method in regions R4 and R5 and p-method in regions R2-R3 and R6-R7).

through root-finding techniques for nonlinear system of equations (*e.g.* using a Newton-Raphson method). We refer to this as the "tangential magnetic field approach" or simply, the *"B_t-method"*.

As mentioned in Section 5.2, hereafter we will assume that the Riemann problem has a solution and that this is unique. As a result, we will not discuss in any detail compound waves which seem to develop in the numerical solution of some special initial states (one of these is shown in Section 5.7.2) and whose admissibility as solution of the Riemann problem is still debated.

5.5 Total-Pressure Approach: "$\boldsymbol{p}$-method"

In the following Sections we describe in detail the approach in which we calculate all of the variables in the Riemann fan using as unknown the total pressure, *i.e.* the p-method. Different set of equations will be derived according to whether the solution is across a shock or a rarefaction wave.

5.5.1 Solution across a shock front

Consider Σ to be a hypersurface in flat spacetime across which ρ, $\boldsymbol{u}$ and $\boldsymbol{T}$ are discontinuous. Let also $\boldsymbol{n}$ be the unit 4-vector normal to Σ so that the Rankine-Hugoniot conditions for relativistic MHD can be expressed as

$$\begin{aligned}
[[\rho u^\alpha]] n_\alpha &= 0 \ , && (5.15)\\
\left[\left[T^{\alpha\beta}\right]\right] n_\alpha &= 0 \ , && (5.16)\\
\left[\left[b^\alpha u^\beta - u^\alpha b^\beta\right]\right] n_\alpha &= 0 \ , && (5.17)
\end{aligned}$$

where we use the double-bracket notation to express the jump of a quantity F across the hypersurface Σ, *i.e.*

$$[[F]] \equiv F_a - F_b \ .$$

where F_a and F_b are respectively the values ahead (a) and behind (b) the shock.

In particular, if Σ is the 4-dimensional hypersurface describing the evolution of a shock wave normal to the x-axis, the unitary condition on $\boldsymbol{n}$ can be used to derive the components

$$n^\alpha = W_s(V_s, 1, 0, 0) \ , \qquad (5.18)$$

where V_s is the coordinate velocity of the shock, $W_s \equiv (1 - V_s^2)^{-1/2}$ its Lorentz factor, and we can rewrite equations (5.15)–(5.17) explicitly as

$$\begin{aligned}
[[J]] \equiv [[\rho W (V_s - v^x) W_s]] &= 0\ , && (5.19)\\
\left[\left[b^0 b^0 - \tau\right]\right] V_s + \left[\left[S^x - b^0 b^x - D v^x\right]\right] &= 0\ , && (5.20)\\
\left[\left[b^0 b^x - S^x\right]\right] V_s + [[S^x v^x + p - b^x b^x]] &= 0\ , && (5.21)\\
\left[\left[b^0 b^y - S^y\right]\right] V_s + [[S^y v^x - b^x b^y]] &= 0\ , && (5.22)\\
\left[\left[b^0 b^z - S^z\right]\right] V_s + [[S^z v^x - b^x b^z]] &= 0\ , && (5.23)\\
[[B^x]] &= 0\ , && (5.24)\\
[[B^y]]\, V_s + [[B^x v^y - v^x B^y]] &= 0\ , && (5.25)\\
[[B^z]]\, V_s + [[B^x v^z - v^x B^z]] &= 0\ , && (5.26)
\end{aligned}$$

where J is the (rest) mass flux across the shock.

After a number of tedious but otherwise straightforward algebraic manipulations, equations (5.19)–(5.26) can be recast as

$$\begin{aligned}
[[v^x]] + \frac{J}{W_s}\left[\left[\frac{1}{D}\right]\right] &= 0\ , && (5.27)\\
\frac{J}{W_s}\left[\left[\frac{W^2\eta^2}{D}\right]\right] - B^x\,[[\eta]] - \frac{J}{W_s}\left[\left[\frac{\tau}{D}\right]\right] + [[p v^x]] &= 0\ , && (5.28)\\
\frac{J B^x}{W_s}\left[\left[\frac{\eta}{D}\right]\right] - B^x[\eta v^x] + \frac{J}{W_s}\left[\left[\frac{W^2\eta^2 v^x}{D}\right]\right] - \left[\left[\frac{B_x^2}{W^2}\right]\right] - \frac{J}{W_s}\left[\left[\frac{S^x}{D}\right]\right] + [[p]] &= 0\ , && (5.29)\\
\frac{J}{W_s}\left[\left[\frac{\eta B^y}{D}\right]\right] + \frac{J}{W_s}\left[\left[\frac{W^2\eta^2 v^y}{D}\right]\right] - B^x\left[\left[\frac{B^y}{W^2}\right]\right] - B^x\,[[\eta v^y]] - \frac{J}{W_s}\left[\left[\frac{S^y}{D}\right]\right] &= 0\ , && (5.30)\\
\frac{J}{W_s}\left[\left[\frac{\eta B^z}{D}\right]\right] + \frac{J}{W_s}\left[\left[\frac{W^2\eta^2 v^z}{D}\right]\right] - B^x\left[\left[\frac{B^z}{W^2}\right]\right] - B^x\,[[\eta v^z]] - \frac{J}{W_s}\left[\left[\frac{S^z}{D}\right]\right] &= 0\ , && (5.31)\\
[[B^x]] &= 0\ , && (5.32)\\
\frac{J}{W_s}\left[\left[\frac{B^y}{D}\right]\right] + B^x\,[[v^y]] &= 0\ , && (5.33)\\
\frac{J}{W_s}\left[\left[\frac{B^z}{D}\right]\right] + B^x\,[[v^z]] &= 0\ , && (5.34)
\end{aligned}$$

where we have defined $\eta \equiv \vec{v}\cdot\vec{B}$ and exploited the property

$$[[F(V_s - v^x)]] = \frac{J}{W_s}\left[\left[\frac{F}{D}\right]\right]\ ,$$

valid for any scalar quantity F.

Next we express all of the variables as functions of J and p_b only. We start by using equation (5.27) to obtain

$$\frac{1}{D_b} = (v_a^x - v_b^x)\,\frac{W_s}{J} + \frac{1}{D_a}\ , \tag{5.35}$$

so that equation (5.28) yields

$$\frac{\tau_b}{D_b} = -\frac{W_a^2\eta_a^2}{D_a} + \frac{W_b^2\eta_b^2}{D_b} + \frac{W_s}{J}\left[B^x\left(\eta_a - \eta_b\right) - p_a v_a^x + p_b v_b^x\right] + \frac{\tau_a}{D_a}\ , \tag{5.36}$$

which depends on v_b^x, p_b but also on B_b^y, B_b^z, v_b^y, v_b^z. To remove the dependence from these latter quantities we employ equations (5.33) and (5.34) to obtain B_b^y and B_b^z as functions of v_b^x, v_b^y v_b^z and p_b, *i.e.*

$$\begin{aligned} B_b^y &= D_b\left(\frac{B_a^y}{D_a}+\frac{W_s}{J}B^x v_a^y-\frac{W_s}{J}B^x v_b^y\right)\ , \qquad (5.37)\\ B_b^z &= D_b\left(\frac{B_a^z}{D_a}+\frac{W_s}{J}B^x v_a^z-\frac{W_s}{J}B^x v_b^z\right)\ . \qquad (5.38)\end{aligned}$$

We can now solve equation (5.29) and finally obtain v_b^x as a function of v_b^y, v_b^z, p_b and J

$$\begin{aligned} v_b^x \;=\; & \frac{D_a\left\{B_x^2 W_s + W_a^2\left[W_s(p_b-p_a) - B_x^2 W_s(1-v_a^y v_b^y - v_a^z v_b^z) + v_a^x(J+B^x W_s\eta_a)\right]\right\}}{W_a^2\left\{D_a\left[J-W_s(B_x^2+p_a-p_b)v_a^x + B^x W_s \eta_a\right] - J(B_x^2 - p_b + W_a^2\eta_a^2 - \tau_a)\right\}} + \\ & \frac{J\left[B^x(B_a^y v_b^y + B_a^z v_b^z - \eta_a) + v_a^x(p_a - W_a^2\eta_a^2 + \tau_a)\right]}{D_a[J-W_s(B_x^2+p_a-p_b)v_a^x + B^x W_s\eta_a] - J(B_x^2 - p_b + W_a^2\eta_a^2 - \tau_a)}\ , \end{aligned} \qquad (5.39)$$

where it should be noted that equation (5.39) reduces to the corresponding hydrodynamical expression in the limit of $\vec{B}=0$ [*cf.* equation (4.12) of Pons *et al.* [116] or equation (3.13) of Rezzolla *et al.* [123]]. Note also that using equations (5.30) and (5.31) it is possible to obtain expressions for v_b^y and v_b^z in terms of the post-shock quantities p and J; the corresponding expressions are rather lengthy and uninspiring; for this reason we report them in Appendix A.

When all of the post-shock quantities are expressed as functions of only p_b and J (*i.e.* V_s), it is still necessary to express V_s as function of the post-shock pressure p_b. To do this we follow Pons *et al.* [116] and use the original jump conditions (5.15), (5.16) and (5.17) to obtain

$$\begin{aligned} [[p]] + J^2\left[\left[\frac{h_{\rm g}}{\rho}\right]\right] &= 0\ , \qquad (5.40)\\ [[h_{\rm g}^2]] - \left(\left(\frac{h_{\rm g}}{\rho}\right)\right)[[p]] - H\,[[b^2]] + 2\left[\left[b^2\frac{h_{\rm g}}{\rho}\right]\right] - 2J^2 H\left[\left[\frac{h_{\rm g}}{\rho}\right]\right] &= 0\ , \qquad (5.41)\end{aligned}$$

where $((F)) \equiv F_a + F_b$ and $H \equiv B_n^2/J^2 - b^2/\rho^2$ is a shock invariant quantity (*i.e.* $[[H]]=0$, [11]). Note that B_n is not just the normal component of the magnetic field but, rather, the projection of $\boldsymbol{b}$ along $\boldsymbol{n}$, *i.e.*

$$B_n \equiv b^\mu n_\mu = -\frac{\eta}{\rho}J + \frac{W_s}{W}B^x\ . \qquad (5.42)$$

Equation (5.41) is also known as the *Lichnerowicz adiabat*, and represents the relativistic MHD counterpart of the *Hugoniot adiabat.*

A couple of remarks should be made. Firstly, equations (5.40)–(5.41) can be used for fast and slow shocks but not for an Alfvèn discontinuity. In this case, in fact, $[[h/\rho]]=0$, equations (5.40)–(5.41) are simple identities and the shock velocity V_s is trivially given by the local Alfvèn velocity V_A. Secondly, for purely hydrodynamical shocks it is possible to find an analytic expression for V_s as a function of the post-shock pressure [*cf.* equation (4.14) of Pons *et al.* [116]]. In relativistic MHD, however, the corresponding analytic expression has not been found and equation (5.40) needs to be solved numerically using a standard root-finding algorithm, which increases the computational costs considerably. To guarantee that we are using the right shock velocity, the root is searched in the appropriate physical interval, i.e. $|V_s| \in (|V_A|, 1)$ for fast shocks and $|V_s| \in (|v^x|, |V_A|)$ for slow shocks.

5.5.2 Solution across a rarefaction wave

Rarefaction waves are self-similar solutions of the flow equations, *i.e.* equations in which all of the fluid quantities depend on x and t through the combination $\xi \equiv x/t$. Using ξ as the independent variable, the set of partial differential MHD equations can be rewritten as the following set of ordinary differential equations (ODEs)

$$\xi\frac{\mathrm{d}D}{\mathrm{d}\xi} - \frac{\mathrm{d}(Dv^x)}{\mathrm{d}\xi} = 0\ , \tag{5.43}$$

$$\xi\frac{\mathrm{d}(\tau - b^0b^0)}{\mathrm{d}\xi} - \frac{\mathrm{d}(S^x - b^0b^x - Dv^x)}{\mathrm{d}\xi} = 0\ , \tag{5.44}$$

$$\xi\frac{\mathrm{d}(S^x - b^0b^x)}{\mathrm{d}\xi} - \frac{\mathrm{d}(S^xv^x + p - b^xb^x)}{\mathrm{d}\xi} = 0\ , \tag{5.45}$$

$$\xi\frac{\mathrm{d}(S^y - b^0b^y)}{\mathrm{d}\xi} - \frac{\mathrm{d}(S^yv^x - b^xb^y)}{\mathrm{d}\xi} = 0\ , \tag{5.46}$$

$$\xi\frac{\mathrm{d}(S^z - b^0b^z)}{\mathrm{d}\xi} - \frac{\mathrm{d}(S^zv^x - b^xb^z)}{\mathrm{d}\xi} = 0\ , \tag{5.47}$$

$$\xi\frac{\mathrm{d}B^x}{\mathrm{d}\xi} = 0\ , \tag{5.48}$$

$$\xi\frac{\mathrm{d}B^y}{\mathrm{d}\xi} - \frac{\mathrm{d}(B^yv^x - B^xv^y)}{\mathrm{d}\xi} = 0\ , \tag{5.49}$$

$$\xi\frac{\mathrm{d}B^z}{\mathrm{d}\xi} - \frac{\mathrm{d}(B^zv^x - B^xv^z)}{\mathrm{d}\xi} = 0\ . \tag{5.50}$$

Equation (5.43) can be further decomposed as

$$(v^x - \xi)\frac{\mathrm{d}\rho}{\mathrm{d}\xi} + \rho\left[(v^x - \xi)W^2v^x + 1\right]\frac{\mathrm{d}v^x}{\mathrm{d}\xi} + (v^x - \xi)\rho W^2v^y\frac{\mathrm{d}v^y}{\mathrm{d}\xi} + (v^x - \xi)\rho W^2v^z\frac{\mathrm{d}v^z}{\mathrm{d}\xi} = 0\ , \tag{5.51}$$

while combining equation (5.44) with equations (5.45)–(5.47) provides us with the relations

$$wW^2(v^x-\xi)\frac{\mathrm{d}v^x}{\mathrm{d}\xi}+(1-\xi v^x)\frac{\mathrm{d}p}{\mathrm{d}\xi}-v^x\xi\frac{\mathrm{d}(b^0b^0)}{\mathrm{d}\xi}+(v^x+\xi)\frac{\mathrm{d}(b^0b^x)}{\mathrm{d}\xi}-\frac{\mathrm{d}(b^xb^x)}{\mathrm{d}\xi} = 0\ , \tag{5.52}$$

$$wW^2(v^x-\xi)\frac{\mathrm{d}v^y}{\mathrm{d}\xi}-\xi v^y\frac{\mathrm{d}p}{\mathrm{d}\xi}-\xi v^y\frac{\mathrm{d}(b^0b^0)}{\mathrm{d}\xi}+v^y\frac{\mathrm{d}(b^0b^x)}{\mathrm{d}\xi}+\xi\frac{\mathrm{d}(b^0b^y)}{\mathrm{d}\xi}-\frac{\mathrm{d}(b^xb^y)}{\mathrm{d}\xi} = 0\ , \tag{5.53}$$

$$wW^2(v^x-\xi)\frac{\mathrm{d}v^z}{\mathrm{d}\xi}-\xi v^z\frac{\mathrm{d}p}{\mathrm{d}\xi}-\xi v^z\frac{\mathrm{d}(b^0b^0)}{\mathrm{d}\xi}+v^z\frac{\mathrm{d}(b^0b^x)}{\mathrm{d}\xi}+\xi\frac{\mathrm{d}(b^0b^z)}{\mathrm{d}\xi}-\frac{\mathrm{d}(b^xb^z)}{\mathrm{d}\xi} = 0\ . \tag{5.54}$$

Finally, rewriting the definition of the local sound speed

$$c_s^2 \equiv \frac{1}{h_g}\left.\frac{\partial p_{\mathrm{g}}}{\partial\rho}\right|_s\ , \tag{5.55}$$

where s is the specific entropy, in terms of the self-similar variable

$$\frac{\mathrm{d}p_{\mathrm{g}}}{\mathrm{d}\xi} = h_g c_s^2\frac{\mathrm{d}\rho}{\mathrm{d}\xi}\ , \tag{5.56}$$

and collecting the different terms in equations (5.43)–(5.50), we obtain the following system of seven ODEs in the seven variables $\rho, p, v^x, v^y, v^z, B^y, B^z$, fully determining the solution across a rarefaction wave

$$0 = (v^x - \xi)\frac{\mathrm{d}\rho}{\mathrm{d}\xi} + \rho\left[(v^x - \xi)W^2 v^x + 1\right]\frac{\mathrm{d}v^x}{\mathrm{d}\xi} + (v^x - \xi)\rho W^2 v^y \frac{\mathrm{d}v^y}{\mathrm{d}\xi} + (v^x - \xi)\rho W^2 v^z \frac{\mathrm{d}v^z}{\mathrm{d}\xi}\ , \tag{5.57}$$

$$\begin{aligned} 0 = \frac{\mathrm{d}p}{\mathrm{d}\xi} - h_g c_s^2 \frac{\mathrm{d}\rho}{\mathrm{d}\xi} + \left(B^2 v^x - B^x\eta\right)\frac{\mathrm{d}v^x}{\mathrm{d}\xi} + \left(B^2 v^y - B^y\eta\right)\frac{\mathrm{d}v^y}{\mathrm{d}\xi} + \left(B^2 v^z - B^z\eta\right)\frac{\mathrm{d}v^z}{\mathrm{d}\xi} - \\ \left(\frac{B^y}{W^2} + v^y\eta\right)\frac{\mathrm{d}B^y}{\mathrm{d}\xi} - \left(\frac{B^z}{W^2} + v^z\eta\right)\frac{\mathrm{d}B^z}{\mathrm{d}\xi}\ , \end{aligned} \tag{5.58}$$

$$\begin{aligned} &0 = (1 - v^x\xi)\frac{\mathrm{d}p}{\mathrm{d}\xi} + \left[B_x^2(v^x + \xi) - 2B^x\eta + W^2(v^x - \xi)(w - \eta^2)\right]\frac{\mathrm{d}v^x}{\mathrm{d}\xi} + \\ &2B_x^2\left\{\left[v^y + \frac{B^y(\xi - v^x)}{2B^x}\right]\frac{\mathrm{d}v^y}{\mathrm{d}\xi} + \left[v^z + \frac{B^z(\xi - v^x)}{2B^x}\right]\frac{\mathrm{d}v^z}{\mathrm{d}\xi} - \frac{(v^x - \xi)}{2B^x}\left[v^y\frac{\mathrm{d}B^y}{\mathrm{d}\xi} + v^z\frac{\mathrm{d}B^z}{\mathrm{d}\xi}\right]\right\}\ , \end{aligned} \tag{5.59}$$

$$\begin{aligned} &0 = \xi v^y \frac{\mathrm{d}p}{\mathrm{d}\xi} - \\ &B^x B^y\left\{\left[(v^x + \xi) - \frac{\eta}{B^x}\right]\frac{\mathrm{d}v^x}{\mathrm{d}\xi} + \left[2v^y + \frac{B^y(\xi - v^x)}{B^x} + \frac{W^2(v^x - \xi)(w - \eta^2)}{B^x B^y} - \frac{\eta}{B^y}\right]\frac{\mathrm{d}v^y}{\mathrm{d}\xi}\right\} - \\ &B^y[2B^x v^z + B^z(\xi - v^x)]\frac{\mathrm{d}v^z}{\mathrm{d}\xi} + \left[\frac{B^x + W^2(v^x - \xi)(B^y v^y + \eta)}{W^2}\right]\frac{\mathrm{d}B^y}{\mathrm{d}\xi} + B^y v^z(v^x - \xi)\frac{\mathrm{d}B^z}{\mathrm{d}\xi}\ , \end{aligned} \tag{5.60}$$

$$\begin{aligned} &0 = \xi v^z \frac{\mathrm{d}p}{\mathrm{d}\xi} - \\ &B^x B^z\left\{\left[(v^x + \xi) - \frac{\eta}{B^x}\right]\frac{\mathrm{d}v^x}{\mathrm{d}\xi} + \left[2v^z + \frac{B^z(\xi - v^x)}{B^x} + \frac{W^2(v^x - \xi)(w - \eta^2)}{B^x B^z} - \frac{\eta}{B^z}\right]\frac{\mathrm{d}v^z}{\mathrm{d}\xi}\right\} - \\ &B^z[2B^x v^y + B^y(\xi - v^x)]\frac{\mathrm{d}v^y}{\mathrm{d}\xi} + B^z v^y(v^x - \xi)\frac{\mathrm{d}B^y}{\mathrm{d}\xi} + \left[\frac{B^x + W^2(v^x - \xi)(B^z v^z + \eta)}{W^2}\right]\frac{\mathrm{d}B^z}{\mathrm{d}\xi}\ , \end{aligned} \tag{5.61}$$

$$0 = B^y\frac{\mathrm{d}v^x}{\mathrm{d}\xi} - B^x\frac{\mathrm{d}v^y}{\mathrm{d}\xi} + (v^x - \xi)\frac{\mathrm{d}B^y}{\mathrm{d}\xi}, \tag{5.62}$$

$$0 = B^z\frac{\mathrm{d}v^x}{\mathrm{d}\xi} - B^x\frac{\mathrm{d}v^z}{\mathrm{d}\xi} + (v^x - \xi)\frac{\mathrm{d}B^z}{\mathrm{d}\xi}\ . \tag{5.63}$$

The system of equations (5.57)–(5.63) can be recast into a simple matrix form and non-trivial similarity solutions exist only if the determinant of the matrix of coefficients is zero. This condition leads to a quartic equation in the self-similar variable ξ

$$\begin{aligned}\tilde{b}_x^2 c_s^2 - \zeta^2 v_x^2 W^2 - (\zeta^2-1)v_x^4 W^4 + \left[2\zeta^2 v_x W^2 - 2\tilde{b}^0\tilde{b}_x c_s^2 + 4(\zeta^2-1)v_x^3 W^4\right]\xi &\quad + \\ \left[(\tilde{b}^0-\tilde{b}_x)(\tilde{b}^0+\tilde{b}_x)c_s^2 + \zeta^2(v_x^2-1)W^2 - 6(\zeta^2-1)v_x^2 W^4\right]\xi^2 &\quad + \\ \left[2\tilde{b}^0\tilde{b}_x c_s^2 - 2\zeta^2 v_x W^2 + 4(\zeta^2-1)v_x W^4\right]\xi^3 + \left[W^4 + W^2\zeta^2\left(1-W^2\right) - (\tilde{b}^0)^2 c_s^2\right]\xi^4 &\quad = \quad 0\ ,\end{aligned} \tag{5.64}$$

where

$$\tilde{b} \equiv \frac{b}{\sqrt{w}}\ , \qquad\qquad \text{and} \qquad\qquad \zeta^2 \equiv c_s^2 + \tilde{b}^2(1-c_s^2)\ , \tag{5.65}$$

and whose roots coincide with the eigenvalues of the original system of equations (5.7). When $B^x = 0$, equation (5.64) reduces to a second-order equation whose roots provide the velocities of the left and right-going fast-waves. In the more general case when $B^x \neq 0$, however, the quartic cannot be recast as the product of two quadratic equations (as it is the case in Newtonian hydrodynamics) and the solution must be found numerically. The corresponding roots provide the velocities of the left and right-going slow and fast magnetosonic rarefaction waves, respectively.

Using the appropriate root for ξ, the system of ODEs (5.57)–(5.63) can be rewritten in terms of the total pressure to obtain a new system of six ODEs to be integrated from the value of pressure ahead the rarefaction to the one behind it[2]. The explicit expressions of these equations are rather lengthy and do not provide any important information; for this reason we report them in Appendix B.

5.5.3 Solution across an Alfvèn discontinuity

The solution across Alfvèn discontinuities is found by imposing the continuity of ρ and p and then solving the system of equations (5.29)-(5.31) and (5.33)-(5.34), using $V_s = V_A$, where $V_A \equiv v_x + B_x/[W^2(\eta \mp \sqrt{w})]$ is the Alfvèn velocity for left ($-$) and right ($+$) going waves, respectively. Since ρ and p are continuous across the Alfvèn discontinuity, a solution needs to be found only for the three components of $\vec{v}$ and for the tangential components of the magnetic field B_y and B_z. In general, and because no analytic solution was found, we solve the corresponding system of equations (5.29)-(5.31), (5.33)-(5.34) numerically with a Newton-Raphson scheme. No major difficulties have been found in determining an accurate solution provided that the waves are all well separated and that a sufficiently accurate initial guess is provided (*cf.* solution in Figure 5.12). For the latter we have used an approximate Riemann solver based on the Harten-Lax-van Leer-Einfeldt (HLLE) algorithm ([68, 50]) and a moderate truncation error (*i.e.* using about 800 gridpoints for the tests reported here). However, considerable difficulties have been encountered if the waves are very close to each other. This is the case, for instance, of test number 5 of Balsara [20], in which the left-going Alfvèn discontinuity and the left-going slow rarefaction wave have very similar propagation velocities (*cf.* solution in Figure 5.11). The exact solution found in this case

---

[2] The number of equations to be solved reduces from seven to six because when using the total pressure as the self-similar variable one equation becomes then trivial, *i.e.* $dp/dp = 1$.

has a truncation error which is small, but larger that those reached in the other tests (*cf.* data in table 5.11).

5.6 Tangential Magnetic Field Approach: "B_t-method"

As done in Sect. 5.5, in what follows we describe in detail the approach referred to as the B_t-method, in which we calculate all of the variables in the Riemann fan using as unknowns the values of the tangential components of the magnetic field, *i.e.* B^y and B^z. As already mentioned, much of the inspiration in the development and use of this method comes from the corresponding approach developed by Ryu and Jones [127] in nonrelativistic MHD. However, important differences are also present.

In particular, in Newtonian MHD the problem can be solved using the norm of the tangential component of the magnetic field $B_t \equiv \sqrt{B_y^2 + B_z^2}$ and the rotation angle $\psi \equiv \arctan(B^z/B^y)$ across Alfvèn discontinuities. This is because B_t is conserved across Alfvèn discontinuities and ψ is constant across fast and slow-waves (see ref. [77]). As a result, the relevant system of equations is solved using as unknowns the values of B_t in regions R2-R3, R4-R5, R6-R7 of the Riemann fan in Figure 5.2 and the angle ψ in regions R3-R6. At the contact discontinuity it is then necessary to solve a system of four equations, given by the continuity of $\vec{v}$ and of p, in the same four unknowns. This can be solved using root-finding techniques such as the Newton-Raphson method. Finally, when $B_x = 0$, the presence of only two fast waves and a tangential discontinuity makes the solution of the problem even simpler (see ref. [127] for details).

In relativistic MHD, on the other hand, the value of B_t can be discontinuous across Alfvèn waves and the angle ψ can vary across fast and slow-waves; it is then not possible to solve the system using the same method. Note also that the equations reported below both for shock and rarefactions waves are strictly valid only if $B^x \neq 0$ and indeed should be used only in regions R4 and R5 of the Riemann fan shown in Figure 5.2. In these regions, only slow-waves are present and these do not appear when $B^x = 0$.

5.6.1 Solution across a shock front

To calculate the solution across a shock front within the B_t-method we start by considering the same system of equations in Section 5.5.1, but we solve equations (5.15)–(5.17) considering B^y and B^z as the unknown quantities. From equations (5.33) and (5.34) we express the post-shock values of v^y and v^z:

$$v_b^y = \frac{1}{B^x}\left[B_a^y \frac{J}{W_s D_a} - B_b^y \left(\frac{J}{W_s D_a} + v_a^x - v_b^x\right) + B^x v_a^y\right] , \tag{5.66}$$

$$v_b^z = \frac{1}{B^x}\left[B_a^z \frac{J}{W_s D_a} - B_b^z \left(\frac{J}{W_s D_a} + v_a^x - v_b^x\right) + B^x v_a^z\right] . \tag{5.67}$$

Using now equation (5.27) to obtain the post-shock value of D

$$D_b = \frac{D_a J}{J + D_a W_s \left(v_a^x - v_b^x\right)} , \tag{5.68}$$

and calculating the post-shock value of the total pressure using the invariance of $h_g B_n$, *i.e.* $[[h_g B_n]] = 0$ (see ref [11]), we can express all of the quantities as a function of the post-shock values of v^x, B^y, B^z, and of the shock-velocity V_s. An analytic solution for the post-shock value of v^x in terms of the other post-shock quantities was sought but not found, forcing to the numerical solution of one of the equations (5.29)–(5.31). Furthermore, in analogy with what done in the p-method, we calculate the value of the shock velocity by solving numerically equation (5.40).

Finally, it may be useful to point out that the numerical solution of equation (5.40) is at times complicated by the existence of two acceptable roots in the interval of velocities in which the value of the slow shock velocity has to be found (*i.e.* between the value of v^x and the value of the Alfvèn velocity). Because only one of these two roots will lead to a convergent exact solution, a careful selection needs to be made. The existence of these two roots could be related to a known problem in Newtonian MHD where the use of the tangential components of the magnetic field as the post-shock independent variables can lead to the presence of more than one solution (*cf.*, for instance, ref. [78]). This problem seems to be present also in relativistic MHD ([85]), but it has not represented a serious drawback for the approach followed here. More work is needed to determine whether the use of the tangential components of the magnetic field as the post-shock independent variables is really optimal or whether different choices are preferable.

5.6.2 Solution across a rarefaction wave

To calculate the solution across a rarefaction wave within the B_t-method we use the same set of ODEs (5.43)–(5.50) discussed in Section 5.5.2, with the only but important difference that we do not use ξ as self-similar variable but, rather, the norm of the tangential components of the magnetic field B_t. More specifically, we use equations (5.43)–(5.45) together with equations (5.49)–(5.50) and substitute the derivative with respect to ξ with the one with respect to B_t. In addition to these equations, which provide a solution for variables ρ, p, v^x, v^y and v^z, we express explicitly the relation between the norm and the tangential components in terms of the angle ψ

$$B^y = \cos\psi B_t \ , \tag{5.69}$$

$$B^z = \sin\psi B_t \ , \tag{5.70}$$

and rewrite them as ODEs having B_t as the self-similar variable

$$\frac{\mathrm{d}B^y}{\mathrm{d}B_t} = \cos\psi \ , \tag{5.71}$$

$$\frac{\mathrm{d}B^z}{\mathrm{d}B_t} = \sin\psi \ . \tag{5.72}$$

Note that in deriving equations (5.71)–(5.72), an implicit assumption has been made: *i.e.* that the angle ψ is constant across the rarefaction wave and thus that the tangential magnetic field does not rotate across the rarefaction wave. With the use of the supplementary equations (5.71)–(5.72), the resulting system of ODEs is complete and can be solved numerically using standard techniques for the solution of a system of coupled ODEs. In practice, the integration is started ahead of the rarefaction and is progressed toward the contact discontinuity, where B_t is given by the values of B^y and B^z chosen at the contact discontinuity. In all of the tests reported here (with the exception of test number 5 of Balsara [20]; see Section 5.7.2 for a discussion), the assumption $\psi = \text{const.}$ is valid. This is probably related to the choice of the initial conditions used in these tests and in particular to the fact that $v^y_A = v^z_A$, $B^y_A = B^z_A$, or $v^z_A = B^z_A = 0$, where $A = (\textit{left}, \textit{right})$, so that the initial states are essentially invariant after the exchange of y with z or the z components of v and B remain equal to zero in all the regions.

It should be noted that also in relativistic hydrodynamics the velocity components tangential to a nonlinear wave can change their norm across the wave, in contrast with what happens in Newtonian hydrodynamics. Considering for simplicity the case for a shock wave in the limit of zero magnetic field, equations (5.30)–(5.31) reduce to $[[S^y/D]] = 0 = [[S^z/D]]$, indicating that the ratio v^y/v^z remains unchanged through shocks so that the tangential velocity 3-vector can change its norm but does not rotate. This property, which applies also across rarefaction waves, is not present across Newtonian nonlinear waves, in which the tangential 3-velocity vector does not rotate, nor changes its norm: $[[v^y]] = 0 = [[v^z]]$.

Although the condition $\psi = \text{const.}$ is exact in nonrelativistic MHD, it may not be valid in relativistic regimes, where the tangential magnetic field is instead free to rotate across the slow rarefaction. In this case, a new strategy needs to be implemented and the simplest one consists of using the angle ψ as the self-similar variable so that the system of equations (5.43)–(5.50) can be expressed in terms of this new integration variable. In addition, the supplementary differential equation for one of the components of the tangential magnetic field can be obtained through the algebraic relation

$$B^y = \frac{\cos\psi}{\sin\psi} B^z \ , \tag{5.73}$$

and its derivative with respect to ψ

$$\frac{\mathrm{d}B^y}{\mathrm{d}\psi} = \frac{\cos\psi}{\sin\psi}\frac{\mathrm{d}B^z}{\mathrm{d}\psi} - \frac{1}{\sin^2\psi} B^z \ . \tag{5.74}$$

The integration of the system of ODEs is done starting from the value of ψ given by the ratio of the tangential components of the magnetic field ahead of the rarefaction wave, up to the value given by the amplitudes of B^y and B^z at the contact discontinuity. Furthermore, as for the p-method, also within the B_t-method the values of the variable ξ are obtained from the quartic equation (5.64).

A representative example of this effect is shown in Figure 5.13, where we plot the exact solution of the generic Alfvèn test at time $t = 1.5$ (*cf.* Table 5.4 for the initial conditions of this test). In particular, the left panel of Figure 5.13 shows the norm of the tangential magnetic field B_t, while the right panel the angle $\psi \equiv \arctan(B^z/B^y)$. Note how both quantities vary across all the fast, slow and Alfvèn waves.

5.7 Numerical Implementation and Representative Results

Since the properties of the magnetic field components in the initial states lead to considerably different Riemann problems (*cf.* the two Riemann fans in Figures 5.1 and 5.2), we will discuss separately the numerical solution in the cases in which $B^x = 0$ and $B^x \neq 0$, emphasizing the properties of some of the most representative tests.

5.7.1 Tangential Initial Magnetic Field: $B^x = 0$

As discussed in Section 5.4, when $B^x = 0$ the Riemann problem consists of only two fast-waves and of a tangential discontinuity across which only v^x and p are continuous (*cf.* Figure 5.1). It should be noted that the condition of continuity of the total pressure across the tangential discontinuity does not necessarily extend also to the gas pressure and, indeed, the latter is in general discontinuous (*cf.* Figures 5.3 and 5.4). In essence, the numerical solution of the Riemann problem when $B^x = 0$ proceeds as follows: given the initial left and right states (*i.e.* regions R1 and R4 of Figure 5.1), we follow the procedure used in relativistic hydrodynamics and determine two unknown states as function of the common total pressure in regions R2 and R3 (p-method). The jump in the normal component of the velocity at the tangential discontinuity is then checked and a new guess for the total pressure found. This procedure is iterated until the solution is found with the desired accuracy. The numerical approach used is a combination of Newton-Raphson and bisection methods, starting from a value for the total pressure which is the average of the initial left and right states. Furthermore, to decide whether the wave considered is a shock or a rarefaction, we compare the values of the total pressure ahead of and behind the wave, solving the set of equations across a shock if the guessed value is larger than the total pressure ahead of the wave and thus in the initial state. We note that this procedure could be improved if an approach similar to the one discussed by Rezzolla *et al.* [122, 123] is implemented, which would exploit the values of the initial relative velocity to predict the wave-pattern produced.

It is also worth noting that even though the numerical strategy discussed so far is very similar to the one used in relativistic hydrodynamics, the equations to be solved in MHD are much more complex and, more importantly, their computational cost is markedly larger. This is essentially because an analytic expression for the shock velocity was not found, so that the latter must be determined numerically.

Representative Tests for $B^x = 0$

Because initial states with a zero normal magnetic field lead to a Riemann problem that is comparatively much simpler to solve, an independent numerical code has been built for this case and it has been tested to reproduce known results in relativistic hydrodynamics, as well as a test proposed by Komissarov [84] (this is referred to as the "shock-tube" test 2). We have also considered an additional, more generic shock-tube test in which all of the quantities in the initial states are nonzero and in which $\vec{v} \cdot \vec{B} \neq 0$ (this is referred to as the

Table 5.1. Initial conditions for the tests of the exact Riemann solver when the magnetic field has zero normal component, *i.e.* $B^x = 0$.

Test type	ρ	$p_{\rm g}$	v^x	v^y	v^z	B^x	B^y	B^z
Komissarov: Shock-Tube 2 ($\Gamma = 4/3$)								
left state	1.0	30.0	0.0	0.0	0.0	0.0	20.0	0.0
right state	0.1	1.0	0.0	0.0	0.0	0.0	0.0	0.0
Generic Shock-Tube ($\Gamma = 5/3$)								
left state	1.0	0.01	0.1	0.3	0.4	0.0	6.0	2.0
right state	0.01	5000	0.5	0.4	0.3	0.0	5.0	20.0

Table 5.2. First significant digits for the exact solution of the test shock-tube 2 of Komissarov [84] computed with an accuracy of 10^{-12}. The left column indicates the regions in which the solution is computed (*cf.* Fig. 5.1).

	ρ	p	v^x	v^y	v^z	B^y	B^z
R1	0.1000E+01	0.2300E+03	0.0000	0.0000	0.0000	0.2000E+02	0.0000
R2	0.2410	0.1611E+02	0.8497	0.0000	0.0000	0.9141E+01	0.0000
R3	0.6426	0.1611E+02	0.8497	0.0000	0.0000	0.0000	0.0000
R4	0.1000	0.1000E+01	0.0000	0.0000	0.0000	0.0000	0.0000

Table 5.3. The same as Table 5.2 but for the generic shock-tube test computed with an accuracy of 10^{-11}.

	ρ	p	v^x	v^y	v^z	B^y	B^z
R1	0.1000E+01	0.1819E+02	0.1000	0.3000	0.4000	0.6000E+01	0.2000E+01
R2	0.1581E+01	0.4459E+02	-0.3073	0.3082	0.2927	0.9582E+01	0.3194E+01
R3	0.5489E-03	0.4459E+02	-0.3073	0.7488	0.5556	0.1023E+01	0.4092E+01
R4	0.1000E-01	0.5138E+04	0.5000	0.4000	0.3000	0.5000E+01	0.2000E+02

"generic shock-tube" test)[3].

Because the procedure for calculating the solution in this case is particularly simple and well tested from relativistic hydrodynamics, the algorithm employed has shown to be very robust and no failures were encountered in the calculation of any quantity. We list in Table 5.1 the set of initial conditions used in the tests solved, while we report in Tables 5.2 and 5.3 the first significant digits for the exact solution of the same tests, reporting in all cases the accuracy obtained (which usually is $\lesssim 10^{-11}$). Finally, the full solutions in space of the various Riemann problems listed in Table 5.1 and for the quantities ρ, v^x, $p_{\rm g}$, p, v^y, v^z, B^y, and B^z are shown in Figures 5.3 and 5.4 at the indicated representative times.

5.7.2 Generic Initial Magnetic field: $B^x \neq 0$

As discussed in Section 5.4, when $B^x \neq 0$ the Riemann problem consists of seven different waves: two fast-waves, two slow-waves, two Alfvèn discontinuities and a central contact discontinuity across which only the density can be discontinuous (*cf.* Figure 5.2). In essence, the numerical solution of the Riemann problem when $B^x \neq 0$ proceeds as follows: starting from the initial left and right states (*i.e.* regions R1 and R8 of Figure 5.2), we compute the states after the fast-waves (regions R2 and R7), then we determine the jumps across the Alfvèn discontinuities (regions R3 and R6) and finally we solve the equations for the slow-waves (regions R4 and R5). As a result of this sequence, the jump conditions in all the physical variables in the two states across the contact discontinuity are computed and if the solution obtained in this way does not reach the desired accuracy, the procedure is iterated.

We also recall that when $B^x \neq 0$, the numerical solution is found using a hybrid method which adopts different sets of equations according to the region in which the Riemann problem has to be solved. In particular, to compute the states after the fast-waves and across the Alfvèn discontinuities we use as unknown the total pressure (p-method; Section 5.5) and to discriminate between shocks and rarefaction waves we evaluate the jump in the total pressure in a way similar to the case when $B^x = 0$. To compute the states after the slow-waves, on the other hand, we use the the tangential components of the magnetic field (B_t-method; Section 5.6) and to decide whether a wave is a shock or a rarefaction we evaluate the jump in the norm of the magnetic field bearing in mind that it must decrease across slow shocks and increase otherwise. Then at the contact discontinuity we compute the jumps in the total pressure and in the components of three-velocity and if they are above a certain accuracy we iterate by changing the values of the total pressure, used in regions R2-R3 and R6-R7, and of the tangential components of the magnetic field, used in regions R4-R5.

It is worth underlining that the solution of the Riemann problem with generic initial states is considerably more demanding than when $B^x = 0$ and not only because of the more numerous waves present. Indeed, the most severe difficulty is due to the fact that the set of equations to be solved becomes particularly stiff near the solution. A careful investigation of the several cases considered has in fact revealed that, in general,

---

[3] We note that a Riemann problem with $B^x = 0$, but with $\vec{v} \cdot \vec{B} \neq 0$ cannot be solved with the exact solution recently proposed by Romero et al. [125]

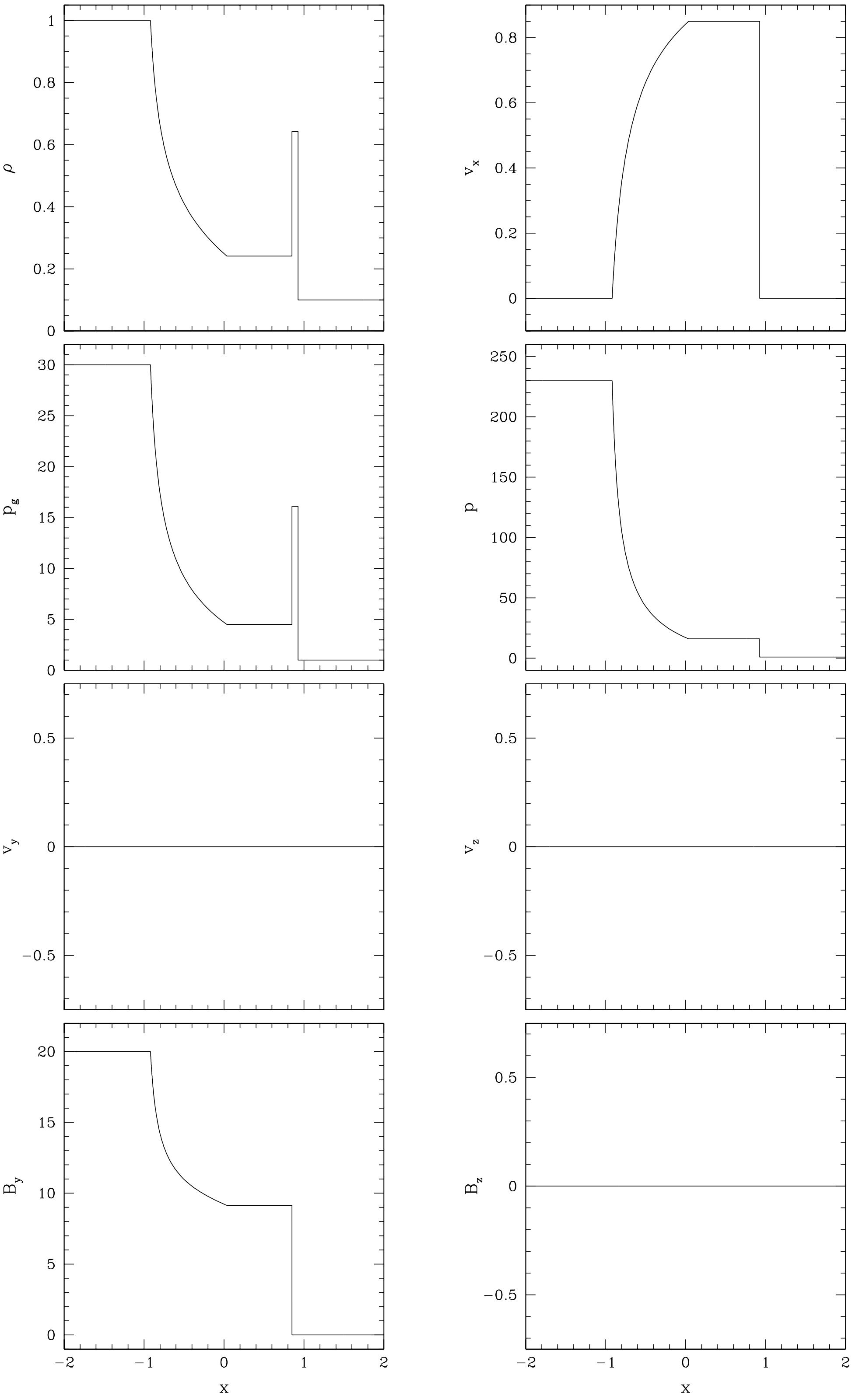

Figure 5.3 Exact solution of the test shock-tube 2 of Komissarov [84] at time $t = 1.0$. The solution is composed of a left-going rarefaction wave, a tangential discontinuity and a right-going shock.

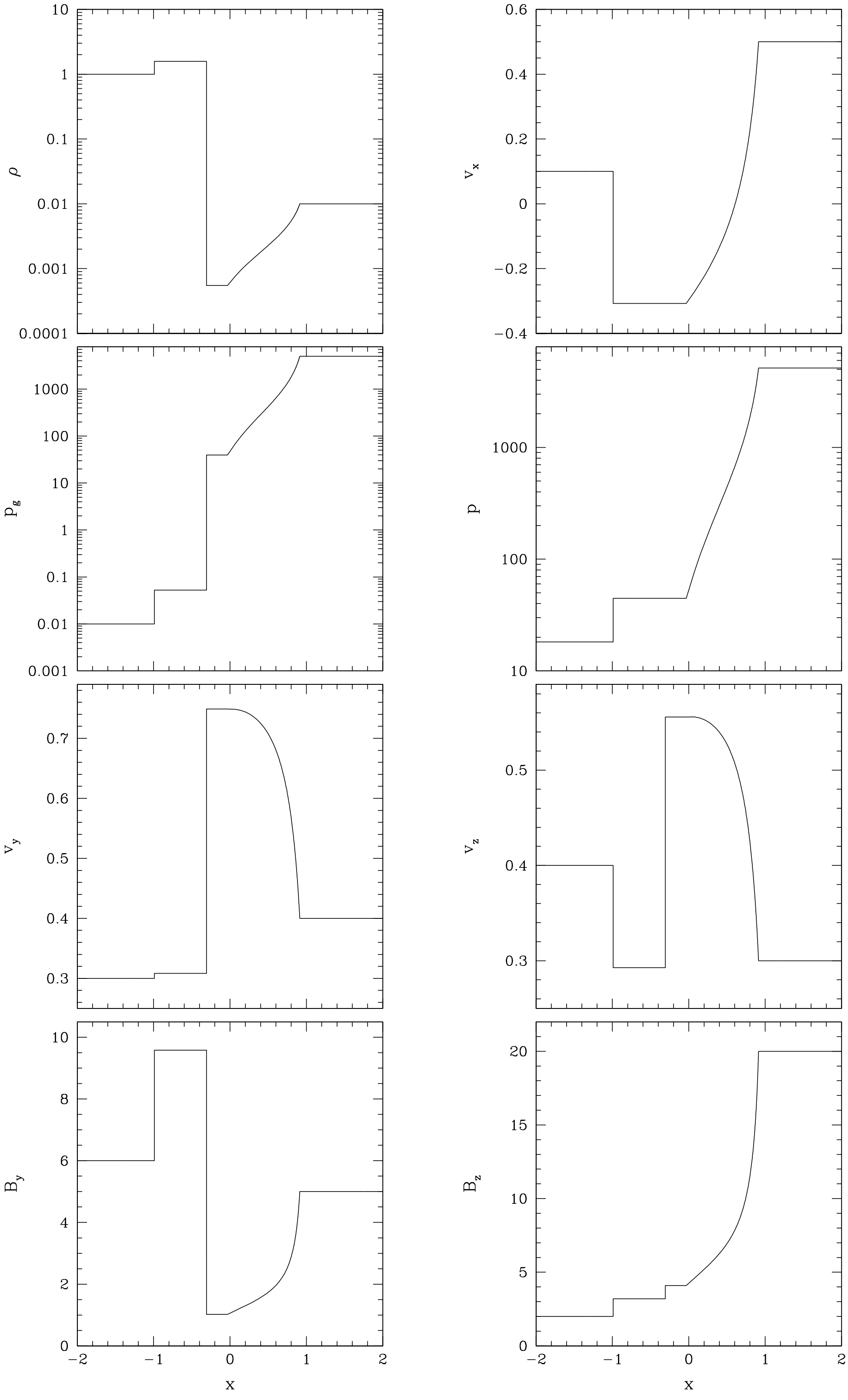

Figure 5.4 Exact solution of the generic shock-tube test at time $t = 1.0$. The solution is composed of a left-going shock, a tangential discontinuity and a right-going rarefaction wave

the functional behavior of the quantities whose roots are sought, changes very rapidly near the roots, stretching the ability of standard root-finding algorithms. As a result, it is not uncommon that the solution cannot be found if the iteration for the search of the root starts from a guess which is not sufficiently close to the exact solution. To avoid such failures and to provide a first guess which is reasonably accurate, we have used as a guide the solution provided by the HLLE approximate Riemann solver[4]. In practice, the approximate solution should be accurate to a few percent in the regions away from the waves, where the states are almost constant (very close to the waves the errors are of course much larger). Using this guess has proved to be sufficient to obtain a solution in all of the cases considered, but of course there is no guarantee that a solution will be straightforwardly found for all of the possible initial states. Our experience when the solution could not be immediately obtained is that an increase in the accuracy of the approximate Riemann solver is in general sufficient to yield a convergent and accurate solution.

Representative Tests for $B^x \neq 0$

Although the numerical code developed for the exact solution of the Riemann problem in relativistic MHD could in principle be used for generic initial data, we have used it in particular to calculate the exact solutions of those less trivial initial states that over the years have become standard references (*e.g.* ref. [84], or ref. [20]). Table 5.4 collects the set of initial conditions used in the tests solved, while we report in Tables 5.5–5.12 the first significant digits for the exact solution of the same tests, reporting in all cases the accuracy obtained (which usually is $\sim 10^{-10}$). Finally, the full solutions in space of the various Riemann problems listed in Table 5.4 and for the quantities ρ, v^x, $p_{\rm g}$, p, v^y, v^z, B^y, and B^z are shown in Figures 5.5–5.12 at the indicated representative times. In addition, Figure 5.13 offers a quantitative view of the changes in the tangential magnetic field B_t and of the rotation angle ψ across the fast, slow and Alfvèn waves in the case of a generic Alfvèn test.

In all of the tests reported in Table 5.4, the HLLE solver with about 800 gridpoints was able to track rather well the exact solution in all of its waves. The only exception to this has been test number 1 of Balsara [20] which represents the relativistic version of the test proposed by Brio and Wu [31] in Newtonian hydrodynamics ([150]). The approximate numerical solution of this test, in fact, shows the development of a left-going slow compound-wave, that is a wave composed by a slow shock adjacent to a slow rarefaction. Since we assume that a slow or fast-wave can either be a pure rarefaction or a pure shock, compound structures of this type cannot be found by construction and thus are not present in the exact solution found (*cf.* Table 5.7 and Figure 5.7). We remark that it is not yet clear whether compound waves have to be considered acceptable physical solutions of the ideal MHD equations and a debate on this is still ongoing (see, for instance, refs. [109, 110, 52, 144, 145, 146]). We here prefer to adopt the standpoint of Ryu and Jones [127] in the development of their exact Riemann solver in nonrelativistic hydrodynamics and not comment further on this until a commonly accepted view has emerged.

---

[4] Note that this is not necessary when $B^x = 0$ since in this case the solution can also be quite far from the exact one and yet the iterative scheme does not show problems in converging to it.

Table 5.4. Initial conditions for the tests of the exact Riemann solver when the magnetic field has nonzero normal component, *i.e.* $B^x \neq 0$.

Test type	ρ	$p_{\rm g}$	v^x	v^y	v^z	B^x	B^y	B^z
Komissarov: **Shock-Tube Test 1** $(\Gamma = 4/3)$								
left state	1.0	1000.0	0.0	0.0	0.0	1.0	0.0	0.0
right state	0.1	1.0	0.0	0.0	0.0	1.0	0.0	0.0
Komissarov: **Collision Test** $(\Gamma = 4/3)$								
left state	1.0	1.0	$5/\sqrt{26}$	0.0	0.0	10.0	10.0	0.0
right state	1.0	1.0	$-5/\sqrt{26}$	0.0	0.0	10.0	-10.0	0.0
Balsara Test 1 $(\Gamma = 2)$								
left state	1.000	1.0	0.0	0.0	0.0	0.5	1.0	0.0
right state	0.125	0.1	0.0	0.0	0.0	0.5	-1.0	0.0
Balsara Test 2 $(\Gamma = 5/3)$								
left state	1.0	30.0	0.0	0.0	0.0	5.0	6.0	6.0
right state	1.0	1.0	0.0	0.0	0.0	5.0	0.7	0.7
Balsara Test 3 $(\Gamma = 5/3)$								
left state	1.0	1000.0	0.0	0.0	0.0	10.0	7.0	7.0
right state	1.0	0.1	0.0	0.0	0.0	10.0	0.7	0.7
Balsara Test 4 $(\Gamma = 5/3)$								
left state	1.0	0.1	0.999	0.0	0.0	10.0	7.0	7.0
right state	1.0	0.1	-0.999	0.0	0.0	10.0	-7.0	-7.0
Balsara Test 5 $(\Gamma = 5/3)$								
left state	1.08	0.95	0.40	0.3	0.2	2.0	0.3	0.3
right state	1.00	1.0	-0.45	-0.2	0.2	2.0	-0.7	0.5
Generic Alfvèn Test $(\Gamma = 5/3)$								
left state	1.0	5.0	0.0	0.3	0.4	1.0	6.0	2.0
right state	0.9	5.3	0.0	0.0	0.0	1.0	5.0	2.0

Table 5.5. First significant digits for the exact solution of the test shock-tube 1 of Komissarov [84] computed with an accuracy of 10^{-10}. The left column indicates the regions in which the solution is computed (*cf.* Fig. 5.2).

	ρ	p	v^x	v^y	v^z	B^y	B^z
R1	0.1000E+01	0.1001E+04	0.0000	0.0000	0.0000	0.0000	0.0000
R2	0.6984E-01	0.2927E+02	0.9115	0.0000	0.0000	0.0000	0.0000
R3	0.6984E-01	0.2927E+02	0.9115	0.0000	0.0000	0.0000	0.0000
R4	0.6984E-01	0.2927E+02	0.9115	0.0000	0.0000	0.0000	0.0000
R5	0.8846	0.2927E+02	0.9115	0.0000	0.0000	0.0000	0.0000
R6	0.8846	0.2927E+02	0.9115	0.0000	0.0000	0.0000	0.0000
R7	0.8846	0.2927E+02	0.9115	0.0000	0.0000	0.0000	0.0000
R8	0.1000	0.1500E+01	0.0000	0.0000	0.0000	0.0000	0.0000

Table 5.6. The same as Table 5.5 but for the exact solution of the test Collision of Komissarov [84] computed with an accuracy of 10^{-6}.

	ρ	p	v^x	v^y	v^z	B^y	B^z
R1	0.1000E+01	0.5292E+02	0.9806	0.0000	0.0000	0.1000E+02	0.0000
R2	0.6331E+01	0.2571E+03	0.4380	0.4069	0.0000	0.1960E+02	0.0000
R3	0.6331E+01	0.2571E+03	0.4380	0.4069	0.0000	0.1960E+02	0.0000
R4	0.2742E+02	0.2819E+03	0.2453E-07	-0.6811	0.0000	0.2250E-06	0.0000
R5	0.2742E+02	0.2819E+03	-0.2810E-07	-0.6811	0.0000	0.2250E-06	0.0000
R6	0.6331E+01	0.2571E+03	-0.4380	0.4069	0.0000	-0.1960E+02	0.0000
R7	0.6331E+01	0.2571E+03	-0.4380	0.4069	0.0000	-0.1960E+02	0.0000
R8	0.1000E+01	0.5292E+02	-0.9806	0.0000	0.0000	-0.1000E+02	0.0000

Another test which deserves a special comment is test number 5 of Balsara [20], in which the left-going Alfvèn discontinuity and the left-going slow rarefaction wave have very similar propagation velocities. Indeed they are so close to each other that not even the HLLE approximate Riemann solver with 40000 gridpoints was able to capture the precise location of the discontinuity. As a consequence, the initial guess for the jumps across the left-going Alfvèn discontinuity was sufficiently good to yield a convergent solution, but not good enough to provide an exact solution with a truncation error comparable with the one reached in all of the other tests (*cf.* data in Table 5.11). In addition, another distinctive feature of this test and which has not been found in any of the others, is the rotation of the angle ψ across the left-going slow rarefaction. To handle this we have followed the procedure discussed in Section 5.6.2 and used equation (5.74) to compute the changes in the tangential magnetic field across the rarefaction wave.

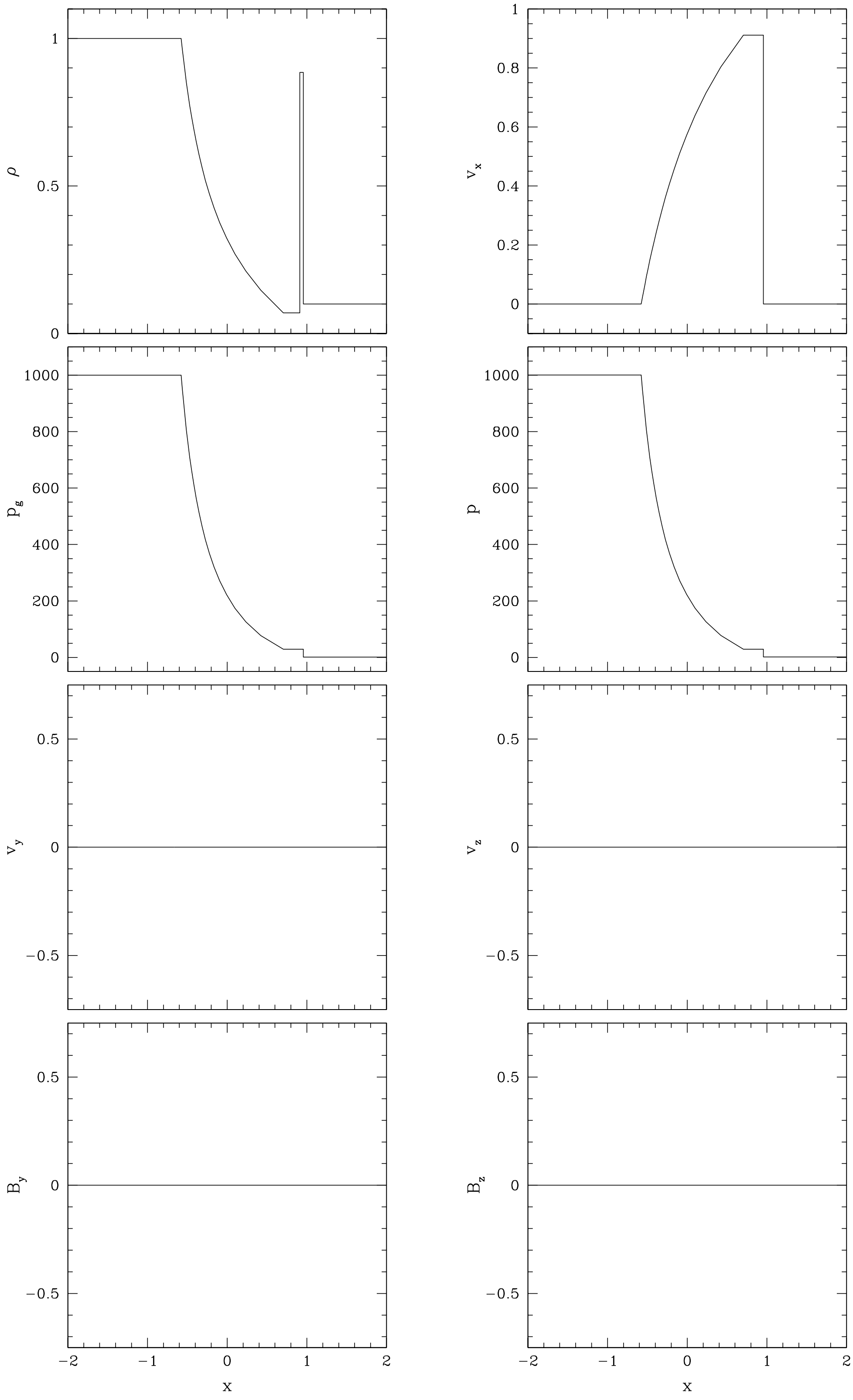

Figure 5.5 Exact solution of the test shock-tube 1 of Komissarov [84] at time $t = 1.0$. The solution is composed of a left-going fast rarefaction, of a contact discontinuity and of a right-going fast shock.

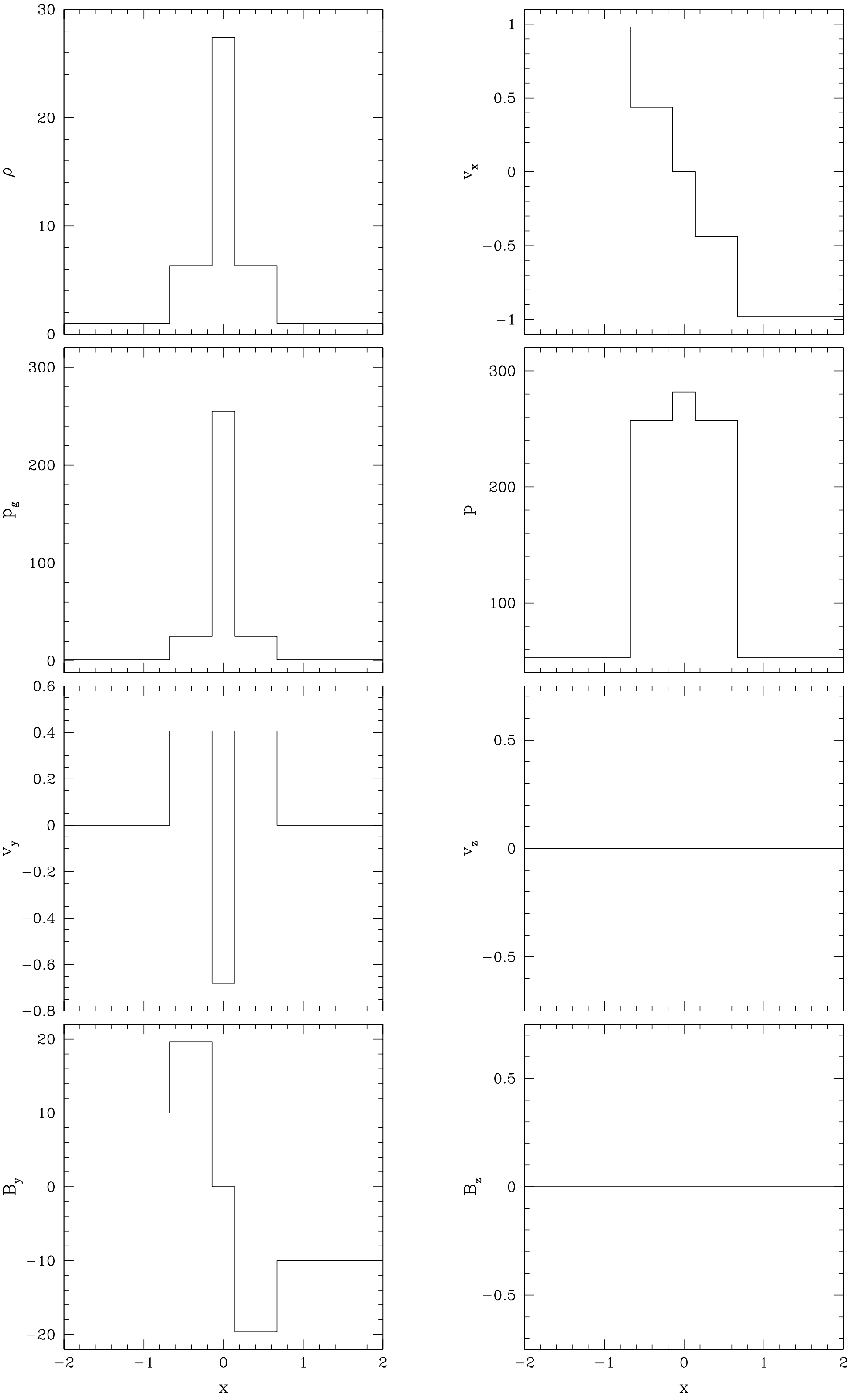

Figure 5.6 Exact solution of the collision test of Komissarov [84] at time $t = 1.22$. The solution is composed of a left-going fast shock, of a left-going slow shock, a right-going slow shock and of a right-going fast shock.

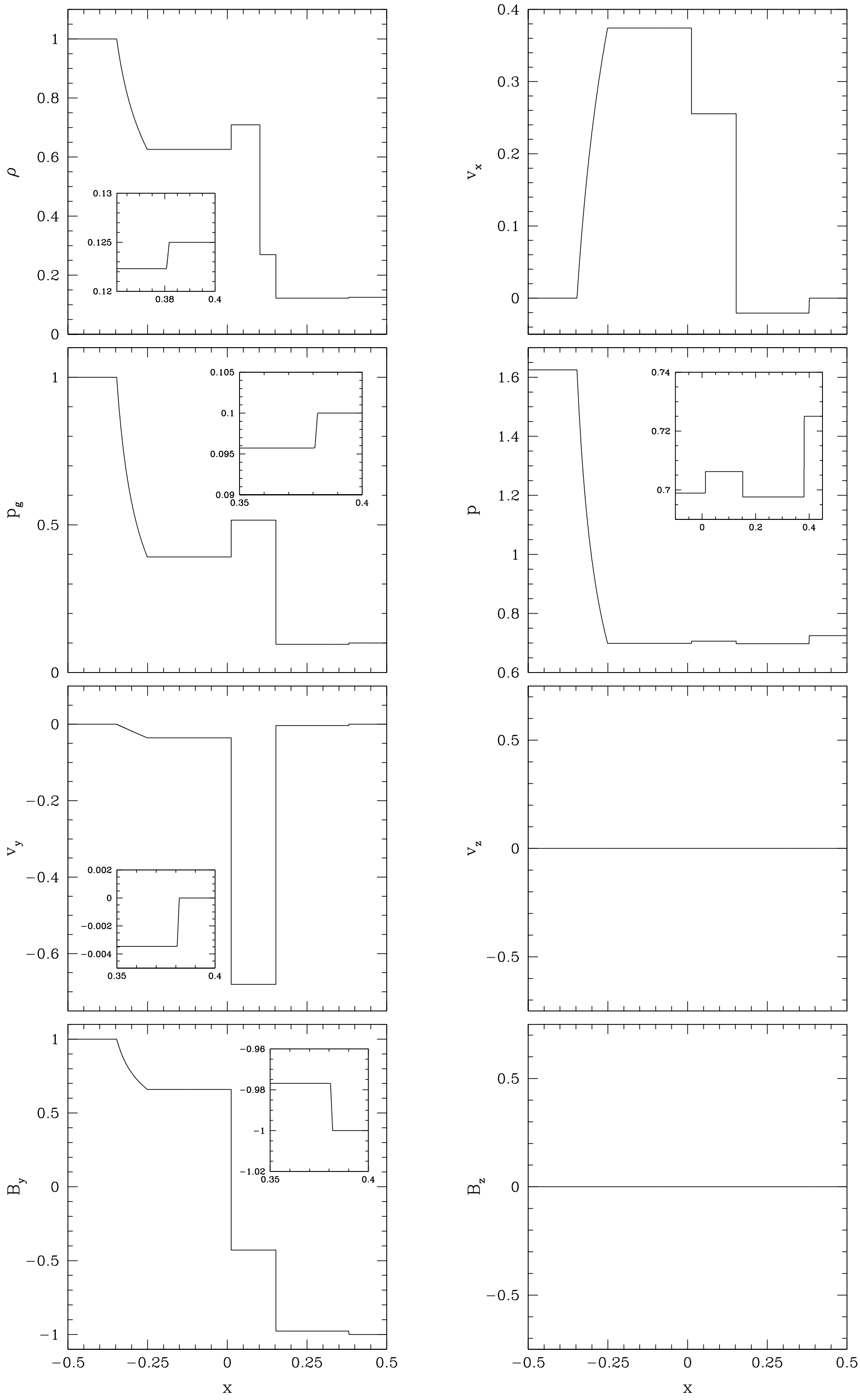

Figure 5.7 Exact solution of the test number 1 of Balsara [20] at time $t = 0.4$ and which represents the relativistic version of the Brio-Wu test [31]. The solution is composed of a left-going fast rarefaction, of a left-going slow shock, of a contact discontinuity, of a right-going slow shock and of a right-going fast rarefaction. Note the absence of a slow compound-wave which cannot be found by construction in our exact solver, but that appears in the solution of the HLLE approximate Riemann solver (not shown).

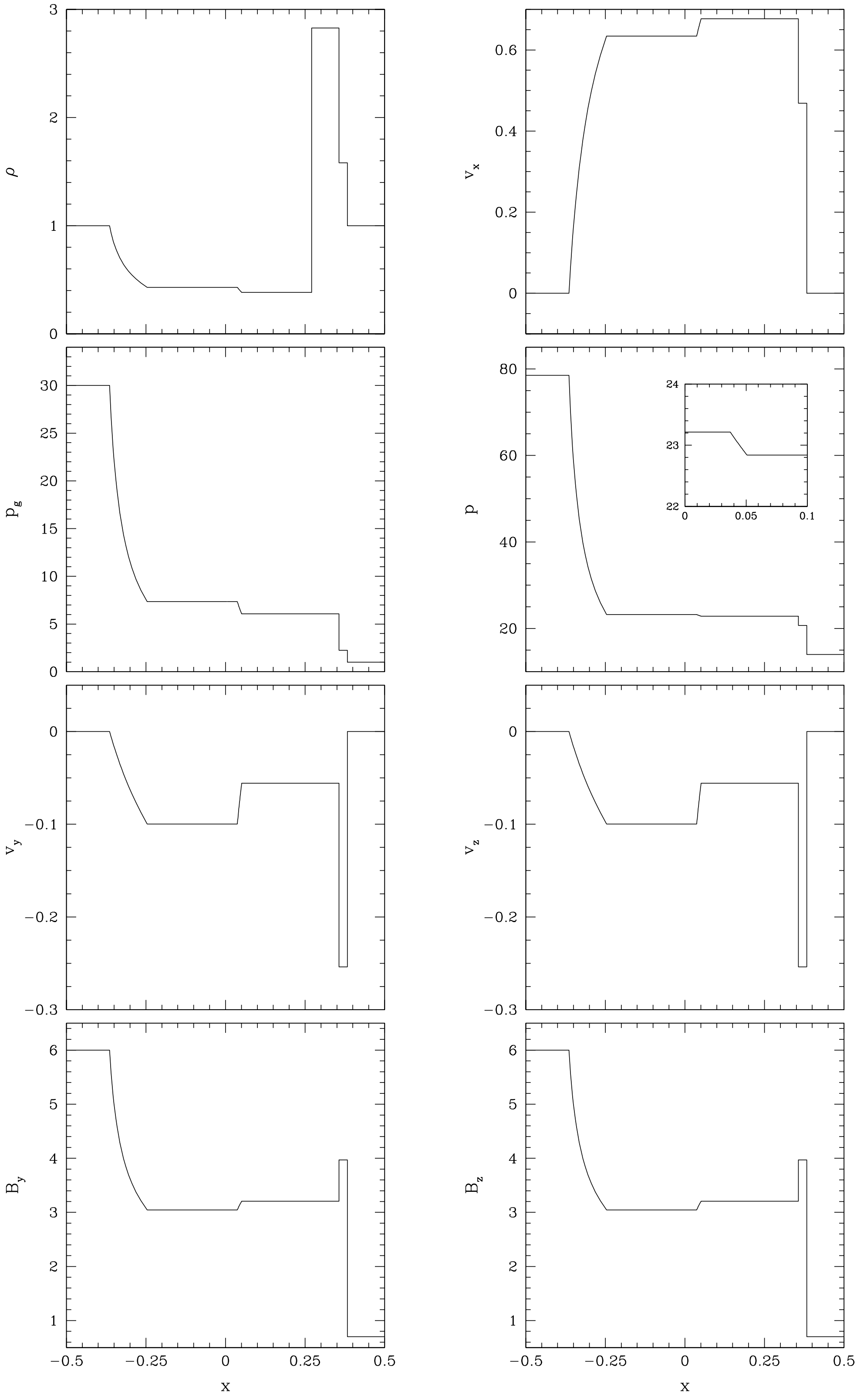

Figure 5.8 Exact solution of the test number 2 of Balsara [20] at time $t = 0.4$. The solution is composed of two left-going fast and slow rarefactions, of a contact discontinuity and of two right-going fast and slow shocks.

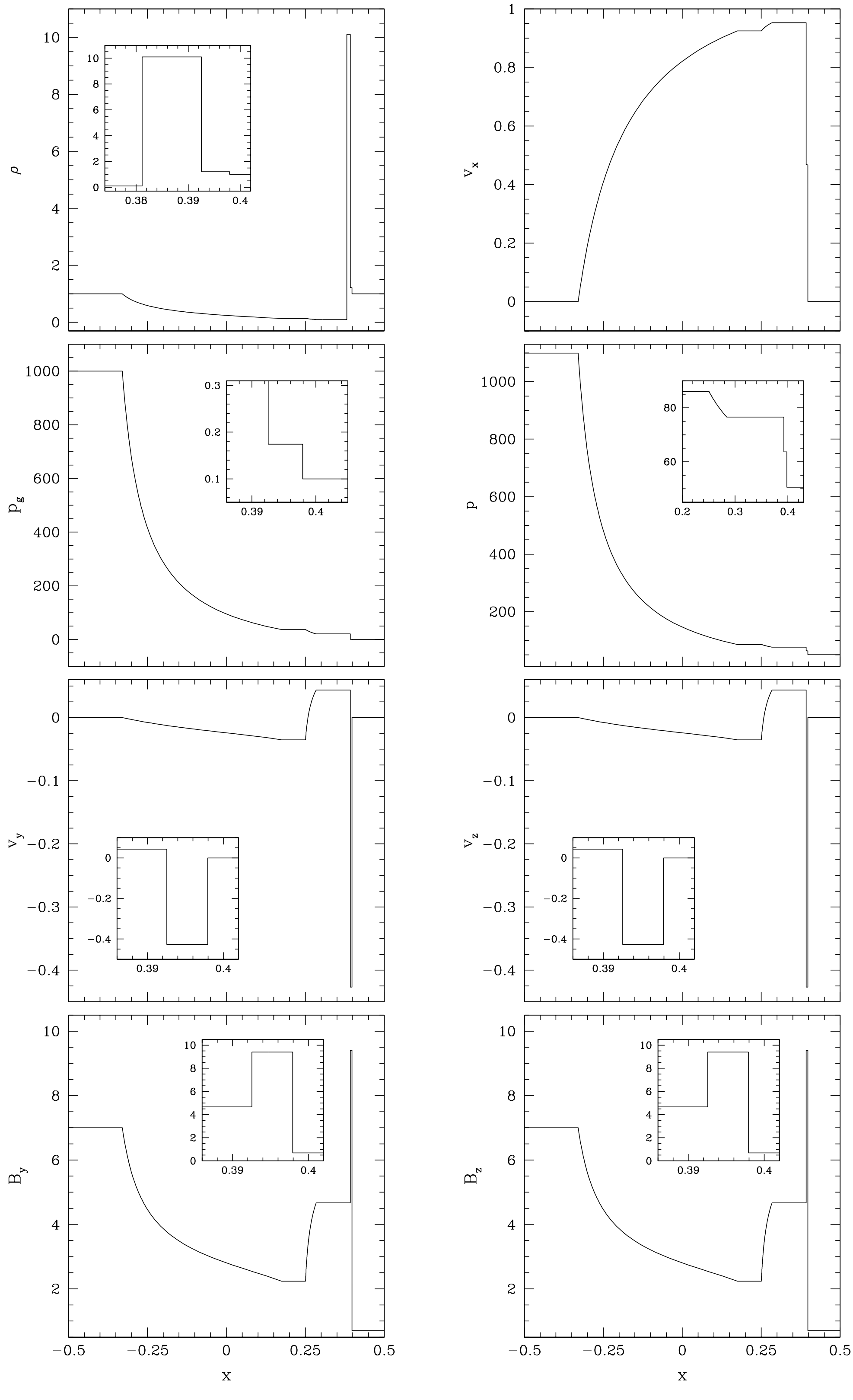

Figure 5.9 Exact solution of the test number 3 of Balsara [20] at time $t = 0.4$. The solution is composed of two left-going fast and slow rarefactions, of a contact discontinuity and of two right-going fast and slow shocks.

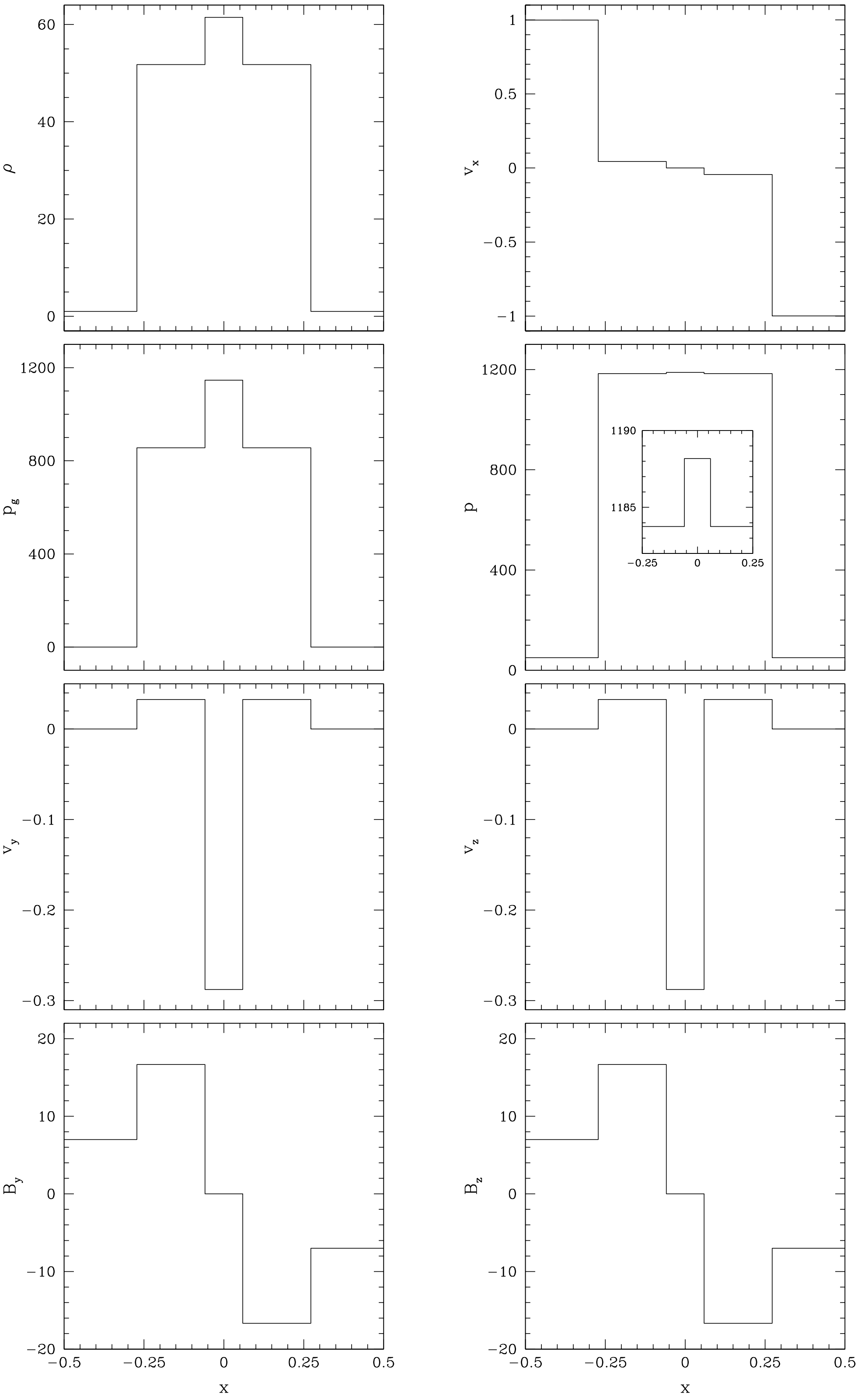

Figure 5.10 Exact solution of the test number 4 of Balsara [20] at time $t = 0.4$. The solution is composed of two left-going fast and slow shocks and of two right-going fast and slow shocks.

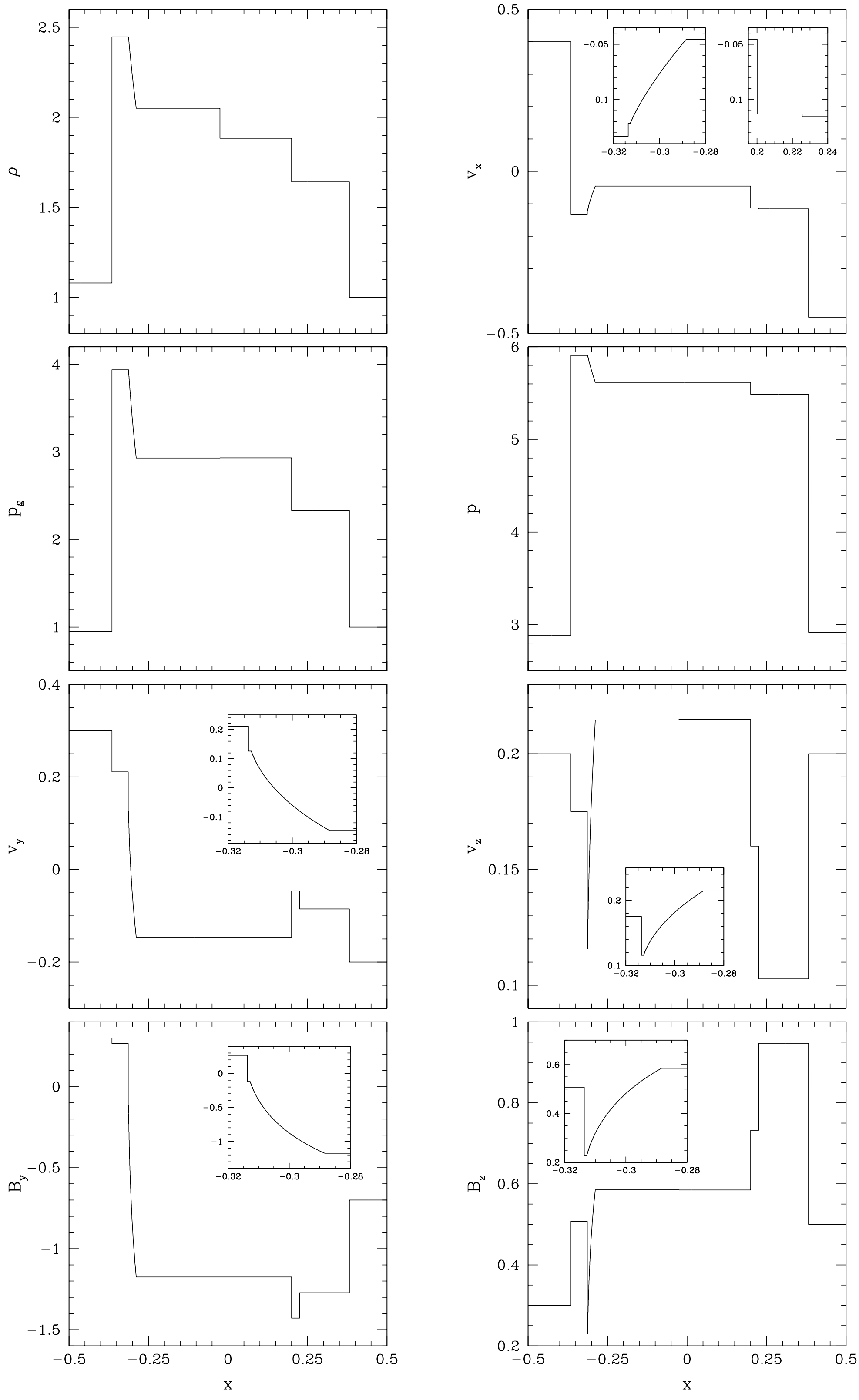

Figure 5.11 Exact solution of the test number 5 of Balsara [20] at time $t = 0.55$. The solution is composed of a left-going fast shock, of a left-going Alfvèn discontinuity, of a left-going slow rarefaction, of a contact discontinuity, of a right-going slow shock, of a right-going Alfvèn discontinuity and of a right-going fast shock. Note that the accuracy in this test is only rather low: 3×10^{-4}.

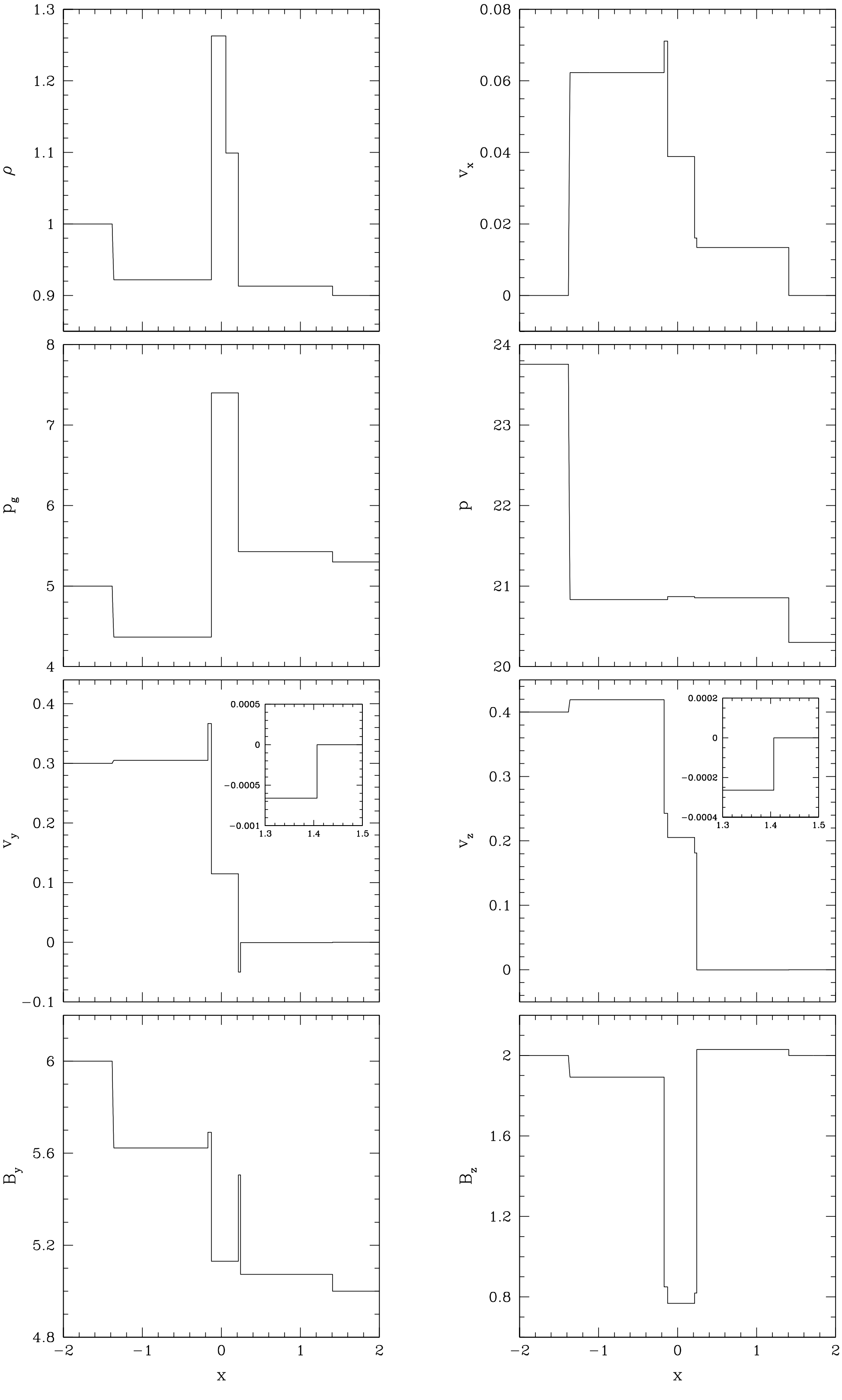

Figure 5.12 Exact solution of the generic Alfvèn test at time $t = 1.5$. The solution is composed of a left-going fast rarefaction, of a left-going Alfvèn discontinuity, of a left-going slow shock, of a contact discontinuity, of a right-going slow shock, of a right-going Alfvèn discontinuity and of a right-going fast shock.

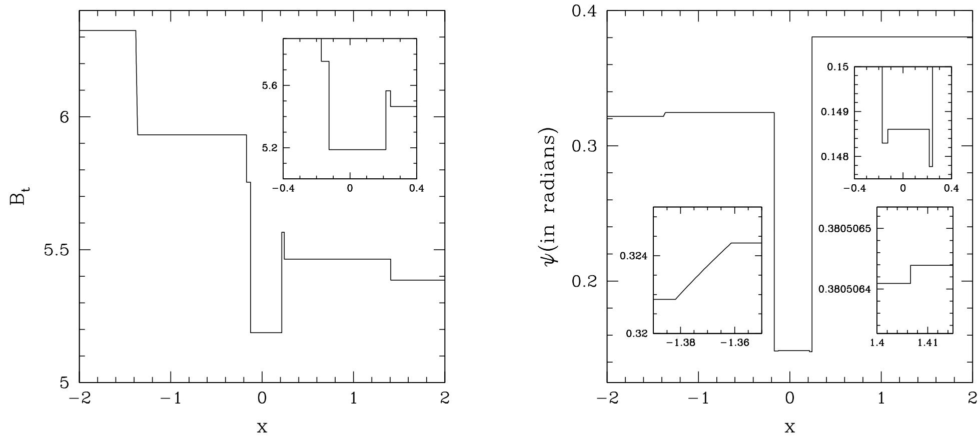

Figure 5.13 Exact solution of the generic Alfvèn test at time $t = 1.5$. The left panel shows the norm of the tangential magnetic field B_t, while the right panel the angle $\psi \equiv \arctan(B^z/B^y)$. Note that both quantities vary across all the fast, slow and Alfvèn waves as a result of a relativistic effect.

Table 5.7. The same as Table 5.5 but for the exact solution of the test number 1 of Balsara [20] computed with an accuracy of 10^{-10}. This test represents the relativistic version of the test proposed by Brio & Wu [31]

	ρ	p	v^x	v^y	v^z	B^y	B^z
R1	0.1000E+01	0.1625E+01	0.0000	0.0000	0.0000	0.1000E+01	0.0000
R2	0.6257	0.6989	0.3742	-0.3561E-01	0.0000	0.6594	0.0000
R3	0.6257	0.6989	0.3742	-0.3561E-01	0.0000	0.6594	0.0000
R4	0.7092	0.7062	0.2555	-0.6804	0.0000	-0.4285	0.0000
R5	0.2695	0.7062	0.2555	-0.6804	0.0000	-0.4285	0.0000
R6	0.1223	0.6976	-0.2080E-01	-0.3460E-02	0.0000	-0.9769	0.0000
R7	0.1223	0.6976	-0.2080E-01	-0.3460E-02	0.0000	-0.9769	0.0000
R8	0.1250	0.7250	0.0000	0.0000	0.0000	-0.1000E+01	0.0000

Table 5.8. The same as Table 5.5 but for the exact solution of the test number 2 of Balsara [20] computed with an accuracy of 10^{-10}.

	ρ	p	v^x	v^y	v^z	B^y	B^z
R1	0.1000E+01	0.7850E+02	0.0000	0.0000	0.0000	0.6000E+01	0.6000E+01
R2	0.4300	0.2321E+02	0.6344	-0.9981E-01	-0.9981E-01	0.3045E+01	0.3045E+01
R3	0.4300	0.2321E+02	0.6344	-0.9981E-01	-0.9981E-01	0.3045E+01	0.3045E+01
R4	0.3830	0.2284E+02	0.6770	-0.5566E-01	-0.5566E-01	0.3205E+01	0.3205E+01
R5	0.2828E+01	0.2284E+02	0.6770	-0.5566E-01	-0.5566E-01	0.3205E+01	0.3205E+01
R6	0.1582E+01	0.2072E+02	0.4688	-0.2538	-0.2538	0.3971E+01	0.3971E+01
R7	0.1582E+01	0.2072E+02	0.4688	-0.2538	-0.2538	0.3971E+01	0.3971E+01
R8	0.1000E+01	0.1399E+02	0.0000	0.0000	0.0000	0.7000	0.7000

Table 5.9. The same as Table 5.5 but for the exact solution of the test number 3 of Balsara [20] computed with an accuracy of 10^{-10}.

	ρ	p	v^x	v^y	v^z	B^y	B^z
R1	0.1000E+01	0.1099E+04	0.0000	0.0000	0.0000	0.7000E+01	0.7000E+01
R2	0.1381	0.8604E+02	0.9246	-0.3513E-01	-0.3513E-01	0.2238E+01	0.2238E+01
R3	0.1381	0.8604E+02	0.9246	-0.3513E-01	-0.3513E-01	0.2238E+01	0.2238E+01
R4	0.9798E-01	0.7653E+02	0.9529	0.4366E-01	0.4366E-01	0.4670E+01	0.4670E+01
R5	0.1010E+02	0.7653E+02	0.9529	0.4366E-01	0.4366E-01	0.4670E+01	0.4670E+01
R6	0.1218E+01	0.6363E+02	0.4670	-0.4270	-0.4270	0.9408E+01	0.9408E+01
R7	0.1218E+01	0.6363E+02	0.4670	-0.4270	-0.4270	0.9408E+01	0.9408E+01
R8	0.1000E+01	0.5059E+02	0.0000	0.0000	0.0000	0.7000	0.7000

Table 5.10. The same as Table 5.5 but for the exact solution of the test number 4 of Balsara [20] computed with an accuracy of 10^{-7}.

	ρ	p	v^x	v^y	v^z	B^y	B^z
R1	0.1000E+01	0.5020E+02	0.9990	0.0000	0.0000	0.7000E+01	0.7000E+01
R2	0.5175E+02	0.1184E+04	0.4408E-01	0.3263E-01	0.3263E-01	0.1668E+02	0.1668E+02
R3	0.5175E+02	0.1184E+04	0.4408E-01	0.3263E-01	0.3263E-01	0.1668E+02	0.1668E+02
R4	0.6148E+02	0.1188E+04	0.1086E-07	-0.2877	-0.2877	0.8042E-09	0.8036E-09
R5	0.6148E+02	0.1188E+04	-0.1089E-07	-0.2877	-0.2877	0.8042E-09	0.8036E-09
R6	0.5175E+02	0.1184E+04	-0.4408E-01	0.3263E-01	0.3263E-01	-0.1668E+02	-0.1668E+02
R7	0.5175E+02	0.1184E+04	-0.4408E-01	0.3263E-01	0.3263E-01	-0.1668E+02	-0.1668E+02
R8	0.1000E+01	0.5020E+02	-0.9990	0.0000	0.0000	-0.7000E+01	-0.7000E+01

Table 5.11. The same as Table 5.5 but for the exact solution of the test number 5 of Balsara [20] computed with an accuracy of 3×10^{-4}.

	ρ	p	v^x	v^y	v^z	B^y	B^z
R1	0.1080E+01	0.2885E+01	0.4000	0.3000	0.2000	0.3000	0.3000
R2	0.2447E+01	0.5908E+01	-0.1331	0.2111	0.1751	0.2662	0.5076
R3	0.2447E+01	0.5908E+01	-0.1215	0.1264	0.1158	-0.1182	0.2302
R4	0.2050E+01	0.5616E+01	-0.4547E-01	-0.1463	0.2146	-0.1175E+01	0.5852
R5	0.1884E+01	0.5616E+01	-0.4543E-01	-0.1462	0.2149	-0.1175E+01	0.5850
R6	0.1642E+01	0.5488E+01	-0.1129	-0.4606E-01	0.1601	-0.1429E+01	0.7320
R7	0.1642E+01	0.5488E+01	-0.1155	-0.8536E-01	0.1027	-0.1272E+01	0.9468
R8	0.1000E+01	0.2918E+01	-0.4500	-0.2000	0.2000	-0.7000	0.5000

Table 5.12. The same as Table 5.5 but for the exact solution of the generic Alfvèn test computed with an accuracy of 10^{-10}.

	ρ	p	v^x	v^y	v^z	B^y	B^z
R1	0.1000E+01	0.2376E+02	0.0000	0.3000	0.4000	0.6000E+01	0.2000E+01
R2	0.9219	0.2083E+02	0.6232E-01	0.3050	0.4193	0.5622E+01	0.1892E+01
R3	0.9219	0.2083E+02	0.7109E-01	0.3669	0.2429	0.5691E+01	0.8502
R4	0.1263E+01	0.2087E+02	0.3886E-01	0.1147	0.2054	0.5130E+01	0.7680
R5	0.1099E+01	0.2087E+02	0.3886E-01	0.1147	0.2054	0.5130E+01	0.7680
R6	0.9130	0.2085E+02	0.1607E-01	-0.5009E-01	0.1813	0.5505E+01	0.8195
R7	0.9130	0.2085E+02	0.1341E-01	-0.6599E-03	-0.2640E-03	0.5073E+01	0.2029E+01
R8	0.9000	0.2030E+02	0.0000	0.0000	0.0000	0.5000E+01	0.2000E+01

5.8 Summary

In this chapter we have presented the procedure for the solution of the exact Riemann problem in special relativistic MHD. Special care has been paid in treating both degenerate initial states (*i.e.* with zero normal magnetic field) leading to a set of only three waves analogous to the ones in relativistic hydrodynamics, as well as generic initial states (*i.e.* with nonzero normal magnetic field) leading to the full set of seven MHD waves.

The approach discussed for the numerical solution of the exact Riemann problem reflects this distinction and different sets of equations are used according to the values of the normal magnetic field. In particular, when $B^x = 0$, all of the equations needed for the solution of the Riemann problem are written as a function of the total pressure, thus following a procedure which is logically equivalent to the one adopted in relativistic hydrodynamics (we have referred to this as to the p-method). When $B^x \neq 0$, on the other hand, an hybrid approach is adopted in which the solution across fast-waves and Alfvèn discontinuities is still computed using the p-method, but the one across slow-waves and the contact discontinuity is computed using equations which are written in terms of the tangential components of the magnetic field (we have referred to this as to the B_t-method). The use of a combined approach for the general case of $B^x \neq 0$ has turned out to be crucial for a successful solution of the problem.

Because of its generality, the solution presented here could serve as a useful if not indispensable test for those numerical codes that solve the MHD equations in relativistic regimes. As the astronomical observations become increasingly more accurate, such numerical codes will become increasingly more important to explain and describe in detail the complex physics of astrophysical compact objects.

As a final remark we note that despite the considerable improvements in the performance of modern computers, the exact solution of the Riemann problem at each grid interface is still computationally too expensive to be used routinely in sophisticated multidimensional numerical codes solving the equations of relativistic hydrodynamics or MHD in either stationary or dynamical spacetimes (see, for instance, Baiotti *et al.* 2005 [16], Duez *et al.* 2005 [47]). While a numerical code based on exact Riemann solvers may represent at least in principle the most accurate approach to the solution of the hydrodynamics and MHD equations, considerable work it still required to make it competitive with less accurate but more computationally efficient methods. A first step in this direction would be, for instance, the search for an analytic solution for the shock velocity and this will be the subject of future work. Another important problem deserving equal attention is that of the uniqueness of the solution. While a global consensus on this issue still needs to be reached, it will remain essential in order to construct a complete and consistent picture of the exact solution of the Riemann problem in relativistic MHD.

Chapter 6

The equations of General Relativistic MHD

6.1 Introduction

As already pointed out in Chapter 1 magnetic fields play a very important role in many astrophysical scenario, such as γ-ray bursts. Most of these involve also very compact objects, such as neutron stars and black holes, and strong gravitational fields making necessary the solution of the equations of general relativistic magnetohydrodynamics (GRMHD). As done in the hydrodynamical case, in order to solve numerically these equations and to have long and stable simulations, it is necessary to recast them in a conservative form adopting a suitable formulation.

Before starting with the description of the formulation used to solve the set of equations implemented in our numerical code, we will summarize the work done so far in the formulation of the equations of general relativistic magnetohydrodynamics in the $3+1$ formalism.

After the pioneering work by May & White [101] with the development of the first numerical code for the solution of general relativistic hydrodynamics equations in spherical symmetry and Lagrangian coordinates, several groups in the world started the development of new numerical codes. In ref. [57] one can find an overview of all the different approaches that have been introduced to solve numerically GRHD equations.

On the other hand, the inclusion of magnetic fields in the simulations is still in a development phase and only recently full GRMHD codes have been built after the first attempt made in ref [156] more than 30 years ago. That work made use of the so called "Wilson formulation" already used in the first general relativistic hydrodynamic simulations [155, 157] and which is based on the use of an Eulerian system of coordinates and on the extension of the equations of Bardeen & Wagoner [23] to include a perfect conducting fluid with a magnetic field. In this formulation the equations for the fluid motion were simply written as:

$$\partial_t S_\mu + \frac{1}{\sqrt{-g}}\partial_i(\sqrt{-g}V^i S_\mu) = \frac{1}{2}\left(\partial_\mu g^{\alpha\beta}\right)\frac{S_\alpha S_\beta}{S^0} + J^\alpha F_{\alpha\mu} \; , \tag{6.1}$$

with

$$
\begin{aligned}
S_\mu &\equiv (\rho + p + \rho\epsilon)u_\mu u^0 \ , && (6.2)\\
V^i &\equiv u^i/u^0 \ , && (6.3)\\
J^\mu &\equiv \frac{\partial}{\partial x^\alpha}(\sqrt{-g}F^{\alpha\mu}) \ , && (6.4)
\end{aligned}
$$

and where p is the gas pressure, ρ the rest-mass density, ϵ the specific internal energy, u^μ the four-velocity of the fluid, g the determinant of the four-metric $g^{\alpha\beta}$ and $F^{\mu\nu}$ is the Faraday electromagnetic tensor field. The magnetic field was described by the two functions H_ϕ and A_ϕ where axisymmetry was assumed. The magnetic field equations of motions were then simply given by:

$$
\begin{aligned}
\partial_t H_\phi &= -(H_\phi V^z)_{,z} - (H_\phi V^r)_{,r} + \Omega_{,z} A_{\phi,r} - \Omega_{,r} A_{\phi,z} \ , && (6.5)\\
\partial_t A_\phi &= -A_{\phi,r} V^r - A_{\phi,z} V^z \ , && (6.6)
\end{aligned}
$$

where Ω is the angular velocity.

This approach, however, sidestepped an important guideline for the formulation of nonlinear hyperbolic systems of equations, namely the preservation of their conservation form. This is a necessary condition to guarantee a correct evolution when shocks are present. Furthermore, some amount of numerical dissipation must be used to stabilize the solution across discontinuities. The first GRMHD numerical code based on this formulation [156] implemented indeed a finite difference scheme with an artificial viscosity to handle the formations of discontinuities, such as shocks. After this first attempt several codes followed based on the same kind of formulation but most of them were built to solve the GRMHD equations on a fixed background, limiting their applications to accretion disks around black holes. In ref. [160, 161] the effects of a Kerr black hole on magnetohydrodynamical accretion were studied with particular attention to the transfer laws of the energy and angular momentum. Koide *et al.* [82] developed a new numerical code based on the use of an artificial viscosity based scheme proposed by Davis [36]. The code was then used to perform the first simulations of jet formation in general relativity [81] and to study the validity of the so-called MHD Penrose process to extract rotational energy from a Kerr black hole [83, 80]. De Villiers and Hawley [39] built another code based on the same formulation adopted in refs [70, 71] to carry a series of studies on accretion flows around Kerr black-holes [40, 72, 41].

Only very recently different groups started to recast the system of GRMHD equations in a conservative form in order to benefit of the use of high-resolution shock-capturing schemes. However the first codes [64, 86, 12] developed using HRSC methods in GRMHD were still used on fixed spacetime backgrounds and their application was again limited to the study of accretion processes around Schwarzschild and Kerr black holes. The first codes able to solve the full set of GRMHD equations on a dynamical background were developed recently by [47, 131] and they were used to perform the first study, still in axisymmetry, of the collapse of magnetized differentially rotating neutron stars [45, 129, 46] which are thought to be good candidates for short γ-ray bursts.

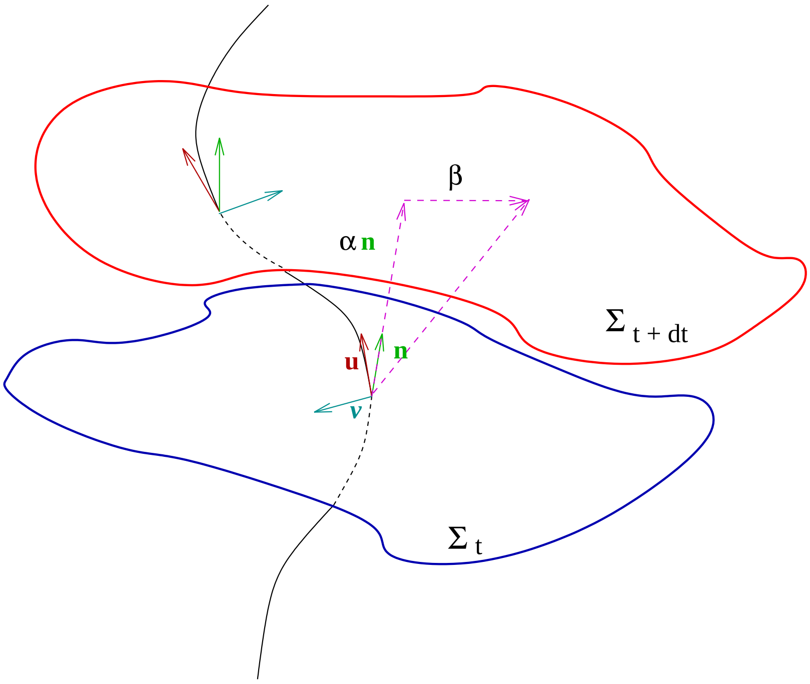

Figure 6.1 The "Valencia formulation". The three-velocity of the fluid $\vec{v}$ is obtained from the projection of its four-velocity $\boldsymbol{u}$ on the space-like hypersurface Σ_t orthogonal to the four-velocity $\boldsymbol{n}$ of the Eulerian observer. (Figure courtesy of L. Rezzolla)

6.2 Formulation of the equations

In our code we make use of the so-called "Valencia formulation" [99, 22] which was originally developed as a $3 + 1$ conservative Eulerian formulation of the general relativistic hydrodynamic equations but it has been recently extended to the case of GRMHD [12]. Following ref. [12] we define the Eulerian observer as the one moving with four velocity **n** perpendicular to the hypersurfaces of constant t at each event in the spacetime (see fig. 6.1). This observer measures the following three-velocity of the fluid:

$$v^i = \frac{h^i_\mu u^\mu}{-u^\mu n_\mu} = \frac{u^i}{W} + \frac{\beta^i}{\alpha} \ , \tag{6.7}$$

where $h_{\mu\nu} \equiv g_{\mu\nu} + n_\mu n_\nu$ is the projector orthogonal to $\boldsymbol{n}$, $\boldsymbol{u}$ is the four-velocity of the fluid and $-u^\mu n_\mu = \alpha u^0 = W$ is the Lorentz factor which satisfies the usual relation $W = 1/\sqrt{1 - v^2}$, where $v^2 \equiv \gamma_{ij} v^i v^j$. The covariant components of the three-velocity are simply given by $v_i = u_i/W$.

6.2.1 Maxwell equations

The electromagnetic field is completely described by the Faraday electromagnetic tensor field $F^{\mu\nu}$ obeying Maxwell equations (cfr ref. [11]):

$$\begin{aligned} \nabla_\nu {}^*F^{\mu\nu} &= 0 \ , & (6.8) \\ \nabla_\nu F^{\mu\nu} &= 4\pi J^\mu \ , & (6.9) \end{aligned}$$

where ∇ is the covariant derivative with respect to the four-metric $g_{\mu\nu}$, J^μ is the charge current four-vector and ${}^*F^{\mu\nu}$ is the dual of the electromagnetic tensor defined as

$${}^*F^{\mu\nu} = \frac{1}{2}\eta^{\mu\nu\lambda\delta}F_{\lambda\delta} \ , \tag{6.10}$$

$\eta^{\mu\nu\lambda\delta}$ being the Levi-Civita pseudo tensor. We can also introduce the magnetic induction field B^α and electric field E^α as measured by a generic observer with four-velocity $\mathbf{U}$

$$\begin{aligned} E^\alpha &\equiv F^{\alpha\beta}U_\beta \ , & (6.11) \\ B^\alpha &\equiv {}^*F^{\alpha\beta}U_\beta \ . & (6.12) \end{aligned}$$

The charge current four-vector J^α can be in general expressed as

$$J^\mu = qu^\mu + \sigma F^{\mu\nu}u_\nu \ , \tag{6.13}$$

where q is the proper charge density and σ is the electric conductivity. We will assume that our fluid is a perfect conductor (ideal MHD condition) and so that $\sigma \rightarrow \infty$. In order to keep the current finite we need to impose $F^{\mu\nu}u_\nu = 0$, i.e. that the electric field measured by the comoving observer is zero.

In this case the electromagnetic tensor can be written in terms of the magnetic field b^μ measured in the comoving frame:

$$F^{\nu\sigma} = \eta^{\alpha\mu\nu\sigma}b_\alpha u_\mu \ , \tag{6.14}$$

and taking the dual of this expression we obtain

$${}^*F^{\mu\nu} = b^\mu u^\nu - b^\nu u^\mu \ . \tag{6.15}$$

As a results, the Maxwell equations become:

$$\nabla_\nu {}^*F^{\mu\nu} = \frac{1}{\sqrt{-g}}\partial_\nu\left(\sqrt{-g}\left(b^\mu u^\nu - b^\nu u^\mu\right)\right) = 0 \ . \tag{6.16}$$

In order to express these equations in terms of quantities measured by an Eulerian observer, we need to compute the relation between the magnetic field measured by the comoving and by the Eulerian observers, respectively $\mathbf{b}$ and $\mathbf{B}$. To do that we introduce the projection operator $P_{\mu\nu} \equiv g_{\mu\nu} + u_\mu u_\nu$ orthogonal to $\boldsymbol{u}$. If we apply this operator to the definition of the magnetic field **B** measured by an Eulerian observer, we can easily derive the following relations:

$$b^0 = \frac{WB^i v_i}{\alpha} , \tag{6.17}$$

$$b^i = \frac{B^i + \alpha b^0 u^i}{W} , \tag{6.18}$$

$$b^2 = b^\mu b_\mu = \frac{B^2 + \alpha^2 (b^0)^2}{W^2} , \tag{6.19}$$

where $B^2 \equiv B^i B_i$. The time component of equation (6.16) gives the divergence-free condition:

$$\partial_i \tilde{B}^i = 0 , \tag{6.20}$$

where $\tilde{B}^i \equiv \sqrt{\gamma} B^i$. The spatial components of equation (6.16) give instead the induction equations for the evolution of the magnetic field:

$$\partial_t(\tilde{B}^i) = \partial_j(\tilde{v}^i \tilde{B}^j - \tilde{v}^j \tilde{B}^i) , \tag{6.21}$$

where $\tilde{v}^i \equiv \alpha v^i - \beta^i$. Note that $\tilde{v}^i$ is equivalent to the definition of the three-velocity used in the Wilson formulation [155, 157] and also used by other GRMHD codes [64, 131, 47].

6.2.2 Conservation equations

We need now to determine the evolution equations for the rest mass density ρ, the specific internal energy ϵ and for the three-velocity v^i. These equations can be computed, as done in relativistic hydrodynamics, from the conservation of the barion number

$$\nabla_\nu(\rho u^\nu) = 0 , \tag{6.22}$$

from the conservation of the energy-momentum

$$\nabla_\nu T^{\mu\nu} = 0 , \tag{6.23}$$

and from an equation of state relating the pressure p to the rest mass density ρ and to the specific internal energy ϵ. The energy-momentum tensor $T^{\mu\nu}$ can be splitted in two parts: one for the fluid $T^{\mu\nu}_{\text{fluid}}$ and one for the electromagnetic field $T^{\mu\nu}_{\text{em}}$: $T^{\mu\nu} = T^{\mu\nu}_{\text{fluid}} + T^{\mu\nu}_{\text{em}}$. We also assume that the fluid is perfect and so we recall that the first part is simply given by:

$$T^{\mu\nu}_{\text{fluid}} = \rho h u^\mu u^\nu + p g^{\mu\nu} , \tag{6.24}$$

where $h = 1 + \epsilon + p/\rho$ is the specific relativistic enthalpy.

The electromagnetic field $T^{\mu\nu}_{\text{em}}$ can be computed directly from the electromagnetic tensor **F** as:

$$T^{\mu\nu}_{\text{em}} = \frac{1}{4\pi}\left(F^{\mu\lambda}F^{\nu}_{\ \lambda} - \frac{1}{4} g^{\mu\nu} F^{\lambda\delta} F_{\lambda\delta}\right) , \tag{6.25}$$

and using the definition of the magnetic field **b** measured by a comoving observer we obtain

$$T^{\mu\nu}_{\text{em}} = \left(u^\mu u^\nu + \frac{1}{2} g^{\mu\nu}\right) b^2 - b^\mu b^\nu . \tag{6.26}$$

Overall, the total energy-momentum tensor is given by

$$T^{\mu\nu} = \left(\rho h + b^2\right) u^\mu u^\nu + \left(p + \frac{b^2}{2}\right) g^{\mu\nu} - b^\mu b^\nu \ . \tag{6.27}$$

Following ref. [12] and to benefit of the use of High Resolution Shock Capturing methods we rewrite equations (6.22), (6.23) and (6.21) in the following conservative form:

$$\frac{1}{\sqrt{-g}} \left[\partial_t(\sqrt{\gamma}\mathbf{F}^0) + \partial_i(\sqrt{-g}\mathbf{F}^i\right] = \mathbf{S} \ , \tag{6.28}$$

where $\mathbf{F}^0$ is the vector of the conserved variable measured by the Eulerian observer

$$\mathbf{F}^0 = \begin{pmatrix} D \\ S_j \\ \tau \\ B^k \end{pmatrix} \ , \tag{6.29}$$

$\mathbf{F}^i$ are the fluxes

$$\mathbf{F}^i = \begin{pmatrix} D\tilde{v}^i/\alpha \\ \\ S_j\tilde{v}^i/\alpha + \left(p + b^2/2\right)\delta^i_j - b_j B^i/W \\ \\ \tau\tilde{v}^i/\alpha + \left(p + b^2/2\right) v^i - \alpha b^0 B^i/W \\ \\ B^k\tilde{v}^i/\alpha - B^i\tilde{v}^k/\alpha \end{pmatrix} \ , \tag{6.30}$$

and $\mathbf{S}$ are the source terms:

$$\mathbf{S} = \begin{pmatrix} 0 \\ \\ T^{\mu\nu}\left(\partial_\mu g_{\nu j} - \Gamma^\delta_{\nu\mu} g_{\delta j}\right) \\ \\ \alpha\left(T^{\mu 0}\partial_\mu \ln\alpha - T^{\mu\nu}\Gamma^0_{\nu\mu}\right) \\ \\ 0^k \end{pmatrix} \ , \tag{6.31}$$

where

$$D \equiv \rho W \ , \tag{6.32}$$

$$S_j \equiv (\rho h + b^2) W^2 v_j - \alpha b^0 b_j \ , \tag{6.33}$$

$$\tau \equiv (\rho h + b^2) W^2 - (p + \frac{b^2}{2}) - \alpha^2 (b^0)^2 - D \ , \tag{6.34}$$

and $0^k = (0, 0, 0)^{\mathrm{T}}$. The system is then closed by an equation of state relating the pressure to the rest-mass density and to the specific internal energy $p = p(\rho, \epsilon)$.

The hyperbolic character of relativistic magneto-hydrodynamics was exhaustively studied by Anile and collaborators (see ref. [11] and references therein) by applying Friedrichs' definition of hyperbolicity [63] which is the extension to a covariant framework of the definition given in Section 3.2.

Chapter 7

The `WhiskyMHD` code

7.1 Introduction

The `Whisky` code was built to be an astrophysical laboratory to study the physics of compact objects in order to predict the dynamics and the gravitational signal emitted. As already mentioned, this code has been applied to the study of the collapse of uniformly and differentially rotating neutron star, head-on collisions of NSs, mixed binary systems composed by a NS and a BH, barmode instability and many others. In all these astrophysical scenarios, magnetic field can play an important role modifying both the dynamics both the gravitational waves signal. In order to investigate these effects and to extend the range of possible applications, including for example phenomena like γ-ray bursts, we have developed `WhiskyMHD`, a new general relativistic MHD code which is the "natural" extension of the `Whisky` code to GRMHD.

7.2 Numerical methods

The `WhiskyMHD` code benefits as `Whisky` of the use of the `Cactus` framework [32] which provides the drivers used for the parallelization of the code, several routines for the output in different formats and collect several useful routines for numerical relativity codes. It especially provides several methods for the solution of the Einstein equations so that our code has to solve the MHD equations while Cactus provides the evolution of the metric quantities at each timestep.

First of all, as done in the `Whisky` code, the evolution equations are integrated in time using the method of line, as described in Section 3.4.4. We recall that the equations are reduced to a set of ODEs that can be evolved using standard numerical methods, such as second-order TVD Runge-Kutta or iterative Cranck-Nicholson schemes [141, 91].

The Einstein equations for the metric variables are written using the conformal traceless formulation described in Section 2.3 (see also refs. [130, 24]); details about the numerical implementation used in our code can be found in refs. [5, 16].

7.2.1 Approximate Riemann solver

The `WhiskyMHD` code makes use as `Whisky` of the High-Resolution Shock-Capturing schemes based on the use of Riemann solvers to compute the fluxes between the numerical cells as already described in Section 3.4.3. It would have been interesting to try to use our exact solver, but its computational cost is still too high to be implemented efficiently in a numerical code. So we opted for an approximate Riemann solver. There are several possible choices and we decided to implement the Harten-Lax-van Leer-Einfeldt (HLLE) approximate Riemann solver [68] because it is simply based on the knowledge of the eigenvalues and it does not require the computation of a basis of eigenvectors. Anton *et al.* [12] have claimed that the accuracy of HLLE is similar to other methods based on the use of the eigenvectors, such as the Roe solver, but they did not provide any quantitative measurement of this statement, also because at that time an exact solution was not available. It would be then interesting to compare in a more precise way the different approximate Riemann solvers used in numerical relativistic MHD codes and our exact solvers could be particular useful, if not necessary, for that purpose.

In the HLLE formulation the flux at the interface between two numerical cells is computed in the following way

$$\mathbf{F}^i = \frac{c_{min}\mathbf{F}^i_r + c_{max}\mathbf{F}^i_l - c_{max}c_{min}\left(\mathbf{F^0}{}_r - \mathbf{F^0}{}_l\right)}{c_{max} + c_{min}}\ , \tag{7.1}$$

where $\mathbf{F}^{\mu}{}_r$ and $\mathbf{F}^{\mu}{}_l$ are computed from the values of the primitive variables reconstructed at the right and left side of the interface, respectively $\mathbf{P}_r$ and $\mathbf{P}_l$, $c_{max} \equiv \max(0, c_{+,r}, c_{+,l})$, $c_{min} \equiv -\min(0, c_{-,r}, c_{-,l})$ and $c_{\pm,r}$ and $c_{\pm,l}$ are the maximum left- and right-going wave speeds computed from $\mathbf{P}_r$ and $\mathbf{P}_l$. If $c_{max} = c_{min}$ the flux becomes the so-called Lax-Friedrichs flux:

$$\mathbf{F}^i = \frac{\mathbf{F}^i_r + \mathbf{F}^i_l - c_{max}\left(\mathbf{F}^0_r - \mathbf{F}^0_l\right)}{2}\ . \tag{7.2}$$

Computation of the eigenvalues

One of the difference with relativistic hydrodynamic codes is the computation of the eigenvalues required by HLLE which is complicated by the presence of a quartic equation. The characteristic structure of GRMHD equations is analyzed in detail in ref. [11] and we simply report here the expression for the computation of the seven wave speeds associated with the entropic, Alfvén, fast and slow magnetosonic waves. The characteristic speed λ of the entropic waves is simply given by $\tilde{v} \equiv \alpha v^i - \beta^i$, while for the Alfvén wave we get the two following possible values for the left- and right-going waves

$$\lambda^i_{1,2} = \frac{b^i \pm \sqrt{(\rho h + b^2)}u^i}{b^0 \pm \sqrt{(\rho h + b^2)}u^0}\ . \tag{7.3}$$

The four speeds that are associated with the fast and slow magnetosonic waves and that are required in the computation of the fluxes can be obtained by the solution of the following quartic equation in each direction i for the unknown λ

$$\rho h\left(\frac{1}{c_s^2} - 1\right)a^4 - \left(\rho h + \frac{b^2}{c_s^2}\right)a^2 G + \mathcal{B}^2 G = 0\ , \tag{7.4}$$

where

$$
\begin{aligned}
a &\equiv \frac{W}{\alpha}\left(-\lambda + \alpha v^i - \beta^i\right) , &(7.5)\\
\mathcal{B} &\equiv b^i - b^0\lambda , &(7.6)\\
G &\equiv \frac{1}{\alpha^2}\left[-(\lambda+\beta^i)^2 + \alpha^2\gamma^{ii}\right] , &(7.7)
\end{aligned}
$$

and c_s is the sound speed. Note that in the last term of the expression for G, i.e. γ^{ii}, the Einstein summation convention must not be used. In the degenerate case in which $B^i = 0$ equation (7.4) can be reduced to a simple quadratic equation that is solved analytically. In the more general case equation (7.4) cannot be reduced to the product of two quadratic equations as in Newtonian MHD and different methods are implemented in the code in order to solve it: an analytic one based on the scheme described in ref. [1], a Newton-Raphson method and the numerical routine `zrhqr` [118] which implements an eigenvalue method. The Newton-Raphson method has shown to be the most accurate and it is the one used by default in our code. We have also implemented an approximate method for the computation of the eigenvalues associated with the fast magnetosonic waves (which are the only two roots needed by HLLE) which was introduced in ref. [92] and which reduces the original quartic to a quadratic equation, that can be solved analytically, by imposing $B^i = 0$ and $B^j v_j = 0$ in eq. (7.4). The values computed in this way differ by less than 1% with respect to the exact values. This method is used in those situations in which the exact solution of the original quartic can be complicated by the presence of degeneracies or when in general two of the roots are close to each other.

7.2.2 Reconstruction methods

A second order TVD slope-limited method is used to obtain $\mathbf{P}_r$ and $\mathbf{P}_l$ from the values of the primitives at the zone center:

$$
\begin{aligned}
\mathbf{P}_l(x_{i+1/2}) &= \mathbf{P}_i + \frac{1}{2}\sigma_i , &(7.8)\\
\mathbf{P}_r(x_{i-1/2}) &= \mathbf{P}_i - \frac{1}{2}\sigma_i . &(7.9)
\end{aligned}
$$

The use of a slope limiter is necessary in order to avoid oscillations in regions of large variation (for example where shocks are present) and at the same time to guarantee second order convergence where the functions are smooth. In `WhiskyMHD` one can choose one of the following limiters:

- **minmod**

  $$\sigma_i = \text{minmod}(P_i - P_{i-1}, P_{i+1} - P_i) , \qquad (7.10)$$

  where $\text{minmod}(a,b) \equiv \frac{1}{2}(\text{sign}(a) + \text{sign}(b))\min(|a|,|b|)$

- **MC**

  $$\sigma_i = \text{minmod}\left(P_{i+1} - P_{i-1}, 2(P_i - P_{i-1}), 2(P_{i+1} - P_i)\right) \qquad (7.11)$$

- **Van Leer**

$$\begin{cases} \sigma_i = 2ab/(a+b) & \text{if } \mathrm{sign}(a) = \mathrm{sign}(b) \text{ and } a+b \neq 0 \\ 0 & \text{otherwise} \end{cases} \tag{7.12}$$

where $a = P_i - P_{i-1}$ and $b = P_{i+1} - P_i$.

7.2.3 Constrained Transport Scheme

Although the analytic solution of equations (6.21) exactly guarantees the constraint (6.20), this may not be true for the numerical solution of these equations. The violation of this constraint may lead to unphysical results and to the development of instabilities in the codes as firstly illustrated by Brackbill & Barnes [30]. To avoid this problem several numerical methods were developed in the past starting from the so-called "staggered mesh magnetic field transport algorithm" first proposed by Yee [158] and then implemented in an artificial viscosity based scheme with the name of "constrained transport" scheme (CT) by Evans & Hawley [51]. In the following years the development on new MHD codes based on Godunov schemes required a new implementation of this method. A version of the CT scheme based on the use of the fluxes computed with the base conservative scheme was introduced by Balsara & Spicer [21]. This algorithm is known as "flux-CT" and it is the one implemented in our code; other possible choices can be found in ref. [147]. We decided to implement the "flux-CT" because of its simplicity and computational efficiency.

This method is based on the relation that exists in ideal MHD between the fluxes of the magnetic field $\vec{B}$ and the value of the electric field $\vec{E} \equiv -\vec{\tilde{v}} \times \vec{\tilde{B}}$. If we define $\tilde{\mathbf{F}}^i \equiv \alpha\sqrt{\gamma}\mathbf{F}^i$ then the following relations hold:

$$E^x = \tilde{F}^z\left(\tilde{B}^y\right) = -\tilde{F}^y\left(\tilde{B}^z\right) , \tag{7.13}$$

$$E^y = -\tilde{F}^z\left(\tilde{B}^x\right) = \tilde{F}^x\left(\tilde{B}^z\right) , \tag{7.14}$$

$$E^z = \tilde{F}^y\left(\tilde{B}^x\right) = -\tilde{F}^x\left(\tilde{B}^y\right) , \tag{7.15}$$

where $\tilde{F}^i\left(\tilde{B}^j\right) \equiv \tilde{v}^i\tilde{B}^j - \tilde{v}^j\tilde{B}^i$. The induction equation (6.21) can then be written as:

$$\partial_t\vec{\tilde{B}} + \vec{\nabla} \times \vec{E} = 0 \, . \tag{7.16}$$

If we take now the integral of this equation across a surface Σ between two numerical cells and apply Stokes theorem we obtain:

$$\partial_t \int_\Sigma \vec{\tilde{B}} \cdot \mathrm{d}\vec{\Sigma} + \int_{\partial\Sigma} \vec{E} \cdot \vec{l} = 0 \, , \tag{7.17}$$

where $\vec{l}$ is the normal vector parallel to $\partial\Sigma$, i.e. the boundary of Σ. Let us now consider the x direction for simplicity and the surface Σ located at $(i+\frac{1}{2}, j, k)$; we denote by (i,j,k) the cell centers on our discrete grid (see fig. 7.1). If we define

$$\tilde{B}^x_{i+\frac{1}{2},j,k} \equiv \frac{1}{\Delta y \Delta z}\int_\Sigma \vec{\tilde{B}} \cdot \mathrm{d}\vec{\Sigma} \, , \tag{7.18}$$

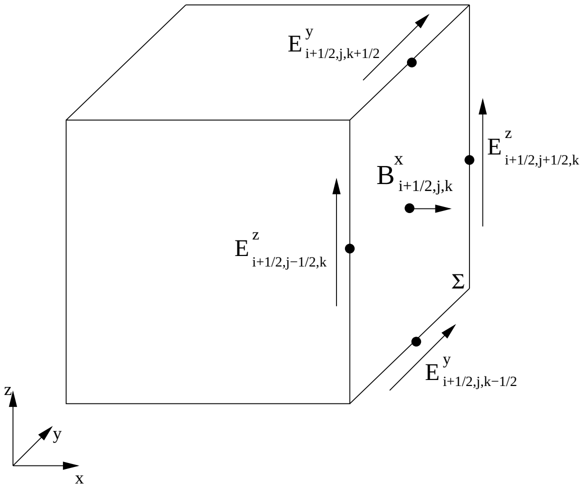

Figure 7.1 The evolution of $\tilde{B}^x_{i+1/2,j,k}$ is determined by the values of the electric field $\vec{E}$ at the edges of the surface Σ located at $(i+1/2,j,k)$.

and take the discrete version of equation (7.17) we obtain:

$$\begin{aligned}\partial_t \tilde{B}^x_{i+\frac{1}{2},j,k} &= -\frac{E^y_{i+\frac{1}{2},j,k-\frac{1}{2}} - E^y_{i+\frac{1}{2},j,k+\frac{1}{2}}}{\Delta z} \\ &\quad -\frac{E^z_{i+\frac{1}{2},j+\frac{1}{2},k} - E^z_{i+\frac{1}{2},j-\frac{1}{2},k}}{\Delta y}\,, \end{aligned} \tag{7.19}$$

where the values of the electric field on the edges of the surface are simply computed taking the arithmetic mean of the fluxes across the surfaces that have that edge in common (cf (7.13)-(7.15)), *e.g.*:

$$\begin{aligned} E^y_{i+\frac{1}{2},j,k+\frac{1}{2}} &= \frac{1}{4}\left(\tilde{F}^x\left(\tilde{B}^z\right)_{i+\frac{1}{2},j,k} + \tilde{F}^x\left(\tilde{B}^z\right)_{i+\frac{1}{2},j,k+1}\right. \\ &\quad \left. -\tilde{F}^z\left(\tilde{B}^x\right)_{i,j,k+\frac{1}{2}} - \tilde{F}^z\left(\tilde{B}^x\right)_{i+1,j,k+\frac{1}{2}}\right) \end{aligned} \tag{7.20}$$

where the fluxes $\tilde{F}^i\left(\tilde{B}^j\right)$ are the ones computed with the approximate Riemann solver described in Sec. 7.2.1.

Since we are using an HRSC method, all the quantities are located at cells centers but in equation (7.19) we are evolving the magnetic field at the surfaces between the cells. The relation between these two different values of the magnetic field is given by a simple average:

$$\tilde{B}^x_{i,j,k} = \frac{1}{2}\left(\tilde{B}^x_{i+\frac{1}{2},j,k} + \tilde{B}^x_{i-\frac{1}{2},j,k}\right) , \tag{7.21}$$

$$\tilde{B}^y_{i,j,k} = \frac{1}{2}\left(\tilde{B}^y_{i,j+\frac{1}{2},k} + \tilde{B}^y_{i,j-\frac{1}{2},k}\right) , \tag{7.22}$$

$$\tilde{B}^z_{i,j,k} = \frac{1}{2}\left(\tilde{B}^z_{i,j,k+\frac{1}{2}} + \tilde{B}^z_{i,j,k-\frac{1}{2}}\right) . \tag{7.23}$$

It is easy to demonstrate that this method guarantees that $\nabla \cdot \vec{\tilde{B}}$ will not grow in time. If we integrate over the volume of a numerical cell this constraint and then use the Gauss theorem we obtain

$$\int_{\Delta V} \nabla \cdot \vec{\tilde{B}} \mathrm{d}V = \sum_{i=1}^{6} \int_{\Sigma_i} \vec{\tilde{B}} \cdot \mathrm{d}\vec{\Sigma} \, , \tag{7.24}$$

where the sum is taken over all the six faces Σ_i that surround the cell.

If we take now the time derivative of this expression and make use of equation (7.17) we have

$$\partial_t \int_{\Delta V} \nabla \cdot \vec{\tilde{B}} \mathrm{d}V = - \sum_{i=1}^{6} \int_{\partial\Sigma_i} \vec{E} \cdot \vec{l} \, , \tag{7.25}$$

and the sum on the right-hand side gives exactly zero since the value of $\vec{E} \cdot \vec{l}$ for the common edge of two adjacent faces has a different sign.

Note that this method preserves the divergence of $\vec{\tilde{B}}$ when the magnetic field is located at the cell surfaces. Anyway there is no need to use a staggered magnetic field, also because in HRSC all the variables are located at cell centers, and so the problem now is how to check the divergence-free property of the cell centered $\vec{\tilde{B}}$. The CT approach indeed does not conserve the usual centered difference definition of $\nabla \cdot \vec{\tilde{B}}$:

$$\left(\nabla \cdot \vec{\tilde{B}}\right)\Big|_{i,j,k} = \frac{\tilde{B}^x_{i+1,j,k} - \tilde{B}^x_{i-1,j,k}}{2\Delta x} + \frac{\tilde{B}^y_{i,j+1,k} - \tilde{B}^y_{i,j-1,k}}{2\Delta y} + \frac{\tilde{B}^z_{i,j,k+1} - \tilde{B}^z_{i,j,k-1}}{2\Delta z} . \tag{7.26}$$

It turns out, however, that the following *cell corner-centered definition* of the divergence

$$\begin{aligned}
&\left(\nabla \cdot \vec{\tilde{B}}\right)\Big|_{i+\frac{1}{2},j+\frac{1}{2},k+\frac{1}{2}} = \\
&\frac{\tilde{B}^x_{i+1,j,k} - \tilde{B}^x_{i,j,k} + \tilde{B}^x_{i+1,j+1,k} - \tilde{B}^x_{i,j+1,k} + \tilde{B}^x_{i+1,j,k+1} - \tilde{B}^x_{i,j,k+1} + \tilde{B}^x_{i+1,j+1,k+1} - \tilde{B}^x_{i,j+1,k+1}}{4\Delta x} + \\
&\frac{\tilde{B}^y_{i,j+1,k} - \tilde{B}^y_{i,j,k} + \tilde{B}^y_{i+1,j+1,k} - \tilde{B}^x_{i+1,j,k} + \tilde{B}^y_{i,j+1,k+1} - \tilde{B}^y_{i,j,k+1} + \tilde{B}^y_{i+1,j+1,k+1} - \tilde{B}^x_{i+1,j,k+1}}{4\Delta y} + \\
&\frac{\tilde{B}^z_{i,j,k+1} - \tilde{B}^z_{i,j,k} + \tilde{B}^z_{i+1,j,k+1} - \tilde{B}^z_{i+1,j,k} + \tilde{B}^z_{i,j+1,k+1} - \tilde{B}^z_{i,j+1,k} + \tilde{B}^z_{i+1,j+1,k+1} - \tilde{B}^z_{i+1,j+1,k}}{4\Delta z}
\end{aligned} \tag{7.27}$$

is conserved from the flux-CT scheme implemented here. Our code checks the divergence of $\vec{\tilde{B}}$ at the end of each iteration using both the expressions above and it has been verified that (7.27) is constant in time while (7.26) is in general not conserved.

7.2.4 Primitive variables recovering

Because the fluxes $\mathbf{F}^i$ depend on the primitive variables $\mathbf{P}$ and not on the evolved conservative variables $\mathbf{F}^0$, one needs to recover after each timestep the primitive variables. Due to the complexity of the system there is no analytic expression that relates the primitive to the conservative (with the exception of the magnetic field variables B^i) and one has to solve numerically the system of equation. There are several methods: one can simply try to solve the full set of 5 equations given by the expressions for (D, S_j, τ) in the 5 unknowns (ρ, v^i, ϵ), we call this the 5D method, or one can try to reduce this system to a smaller set of equations. In our case we implemented two methods: in the first one we reduce the system to a couple of non-linear equations (2D method), while in the second one we need to solve only 1 equation (1D method). A review of other possible methods can be found in ref. [115].

2D method

The following procedure is the same used in ref. [12] and it is an extension to full general relativity of the method developed in ref. [84] in special relativity. The idea is to take the modulus $S^2 = S^j S_j$ of the momentum instead of the expression for its three components reducing the total number of equations that one has to solve. Using the relations (6.17)-(6.19) it is possible to write S^2 as

$$S^2 = (Z + B^2)^2 \frac{W^2 - 1}{W^2} - (2Z + B^2) \frac{(B^i S_i)^2}{Z^2} \,, \tag{7.28}$$

where $Z \equiv \rho h W^2$. It is also possible to rewrite the equation for the total energy in a similar way

$$\tau = Z + B^2 - p - \frac{B^2}{2W^2} - \frac{(B^i S_i)^2}{2Z^2} - D \,. \tag{7.29}$$

Using then the definition of $D = \rho W$, equations (7.28) and (7.29) form a closed system for the two unknowns p and W, assuming the function $h = h(\rho, p)$ is provided, which means that this method does not assume the use of a particular equation of state. For a polytropic EoS the integration of the total energy equation can be avoided and the system reduce to the numerical solution of the equation (7.28). Once the roots for W, p and $\rho = D/W$ are found, it is possible to compute the values of v_i using the definition of the momentum S_j

$$v_i = \frac{B_i (B^j S_j) + S_i Z}{Z(B^2 + Z)} \,. \tag{7.30}$$

1D method

The basic idea of this method is to consider also the gas pressure p as a function of W reducing the total number of equations that must be solved numerically. Assuming that we are using an ideal equation of state, Z can in fact be rewritten as

$$Z = DW + \frac{\Gamma}{\Gamma - 1} p(W) W^2 \,. \tag{7.31}$$

Using equation (7.31) it is possible to rewrite (7.29) as a cubic equation for $p(W)$ which admits only one physical solution. So at the end we need only to solve equation (7.28) for the only unknown W. Having obtained W, we can then compute $p = p(W)$ and the other quantities in the same way as done in the 2D method.

7.2.5 Excision

As mentioned in 3.4.6 many interesting astrophysical scenarios involve the presence of black hole and so of regions of space-time where singularity are present. These regions are causally disconnected from the rest of the physical domain and the values of the fields inside should not affect the zone outside the event horizon. This is not true in numerical codes where it can happen that some information from inside the event horizon is used to compute the values of the variables outside. In order to avoid this, excision algorithms were developed in general relativistic hydrodynamics and they are based on the use of some kind of boundary condition applied to the boundary between the excised zone, where the equations are no more solved, and the domain outside. As already done in the `Whisky` code we apply a zeroth-order extrapolation to all the variables at the boundary, i.e. a simple copy of the MHD variables across the excision boundary. Authors in [47] have instead implemented a different method based on the use of a linear extrapolation. In Section 7.3 we will show that even if this condition give better and more accurate results in some particular tests, it can produce wrong results when shocks are present. For completeness we have decided to include both the algorithms in our code.

It is important also to note that also other methods, not based on excision techniques, are being developed to improve the stability of numerical codes when black hole are present in the domain. One of these is based on the use of a Kreiss-Oliger dissipation inside the excision region avoiding the formation of steep gradients in the metric components [18]. Our code is already able to use this new technique but it has not been tested yet.

7.3 Tests

Here we report the results for a series of test done to check all the different algorithms implemented. Validation indeed represents an important aspect of the development of any numerical code because it is necessary to be sure that all the algorithms are implemented correctly before starting to do real simulations, especially if one wants to trust the results.

7.3.1 Riemann problems

It is important to stress the fact that the exact solution of the Riemann problem in relativistic MHD is becoming a standard tool for those groups that are developing new special and general relativistic MHD codes. As our code is based on the use of approximate Riemann solvers we first tested the code against a set of Riemann problems in Minkowsky space-time proposed by Balsara [20]. All these tests were run on a grid of unit length with 1600 grid points with the initial discontinuity located at the center of the grid. An ideal equation of state with $\Gamma = 5/3$ were used with the exception of the first test with $\Gamma = 2$.

Table 7.1. Initial conditions for the Riemann problems used to test the code.

Test type	ρ	p	v^x	v^y	v^z	B^x	B^y	B^z
Balsara Test 1 (Brio & Wu) $(\Gamma = 2)$								
left state	1.000	1.0	0.0	0.0	0.0	0.5	1.0	0.0
right state	0.125	0.1	0.0	0.0	0.0	0.5	-1.0	0.0
Balsara Test 2 $(\Gamma = 5/3)$								
left state	1.0	30.0	0.0	0.0	0.0	5.0	6.0	6.0
right state	1.0	1.0	0.0	0.0	0.0	5.0	0.7	0.7
Balsara Test 3 $(\Gamma = 5/3)$								
left state	1.0	1000.0	0.0	0.0	0.0	10.0	7.0	7.0
right state	1.0	0.1	0.0	0.0	0.0	10.0	0.7	0.7
Balsara Test 4 $(\Gamma = 5/3)$								
left state	1.0	0.1	0.999	0.0	0.0	10.0	7.0	7.0
right state	1.0	0.1	-0.999	0.0	0.0	10.0	-7.0	-7.0
Balsara Test 5 $(\Gamma = 5/3)$								
left state	1.08	0.95	0.40	0.3	0.2	2.0	0.3	0.3
right state	1.00	1.0	-0.45	-0.2	0.2	2.0	-0.7	0.5

The initial conditions for all the tests are reported in table 7.1. For the first time we have also compared the numerical solution with the exact one computed with our exact Riemann solver [66]. The use of exact solution is particularly useful because it allows to check in a quantitative way the ability of our code to solve all the different waves that can form in relativistic MHD and especially shocks. In all the figures the exact solution is represented with a solid line, while the numerical one with points.

The first test is the relativistic analog of the classical Brio-Wu shock tube problem [31] as adapted to the relativistic MHD case by Van Putten [150]. The initial discontinuity develops a left-going fast rarefaction, a left-going slow compound wave, a contact discontinuity, a right-going slow shock and fast rarefaction. In analogy with what Anton *et al.* [12] did we have also repeated the test with a value of the lapse different from unity, i.e. $\alpha = 2$ and also with a different value for the x component of the shift, $\beta^x = 0.4$. The numerical results are showed in figure 7.2 with the exact solution (solid line). The difference between the numerical code and the exact solution at the compound wave is due to the fact that our exact solver, as already pointed out in Chapter 5, is based on the *working assumption* that compound waves never forms.

All the other four Riemann problems proposed by Balsara were solved in the standard Minkowsky space-time, i.e. $\alpha = 1$ and $\vec{\beta} = 0$. As shown in figures 7.3-7.6 our code is able to resolve all the different waves present in MHD with a very high agreement with the exact solutions. In figure 7.7 we also show for the test number 2 of Balsara the

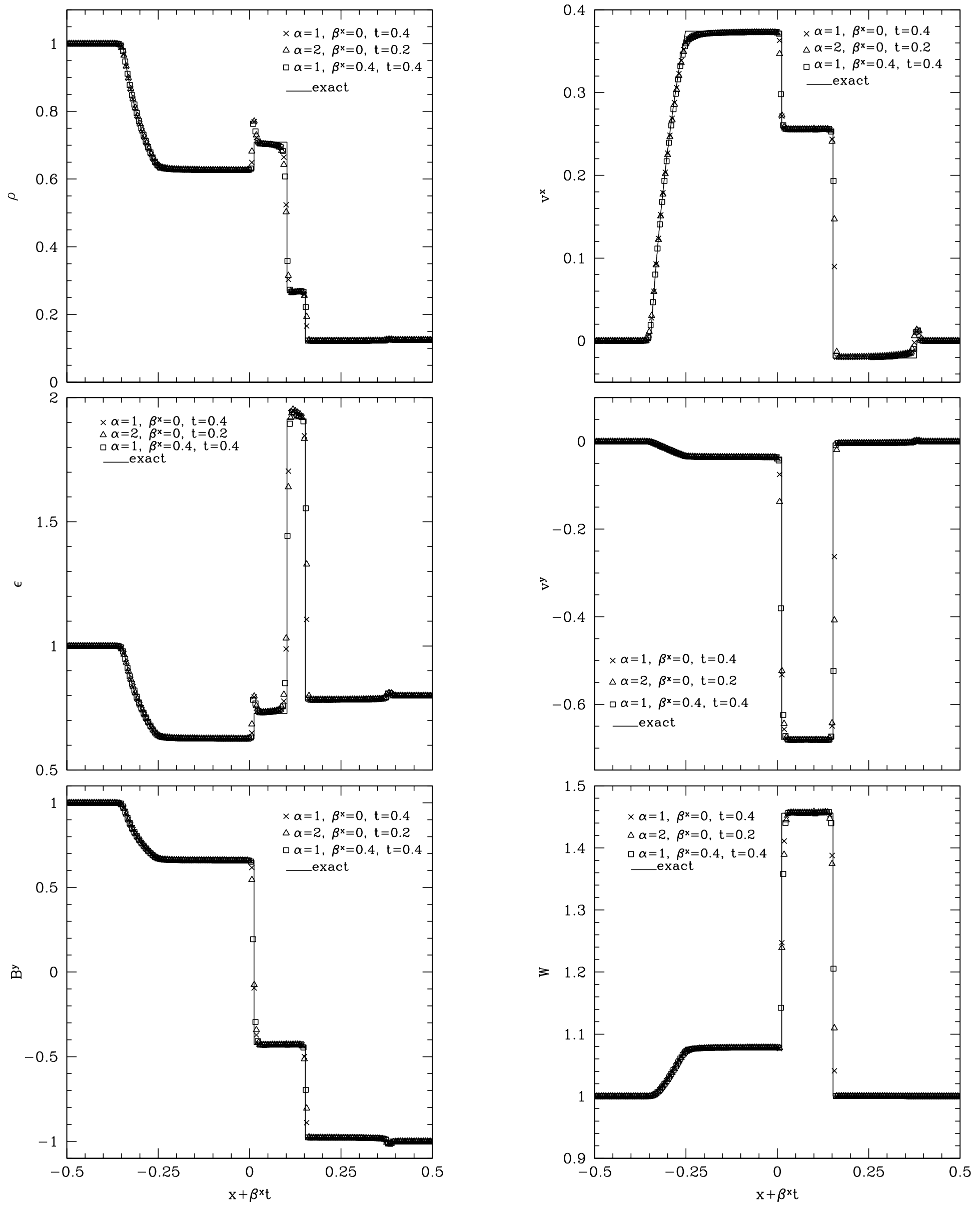

Figure 7.2 Numerical solution of the test number 1 of Balsara with different values for the lapse α and the shift β. The solid line represents the exact solution, the crosses the numerical one at time $t = 0.4$, the open triangle at time $t = 0.2$ but with $\alpha = 2$ and the open squares at $t = 0.4$ but with $\beta^x = 0.4$, in this last case the solution is shifted on the x-axis by the amount $\beta^x t$. Note that the exact solution was computed with our exact solver which does not assume the presence of compound waves in the wave pattern, so it shows a slow shock instead of the compound wave. (Only 160 of the 1600 data points used in the simulation are drawn)

L_1-norm of the relative error on the rest mass density ρ

$$\frac{\delta\rho}{\rho} \equiv \frac{\sum_{i,j,k} |\rho_{i,j,k} - \rho_{\mathrm{exact}}(x_i, y_j, z_k)|}{\sum_{i,j,k} \rho_{\mathrm{exact}}(x_i, y_j, z_k)} \,, \tag{7.32}$$

as a function of the number of point N and for the three different slope limiters implemented in our code.

7.3.2 Excision tests on a flat background

We next show our code's ability to accurately solve shocks also when an excision region is present in the domain. To this scope, we have used the test number 2 of Balsara excising the region $[0.25, 0.5]$ and using the zeroth-order extrapolation scheme. In this case the fast and slow shocks moving to the right go inside the excised region and the solution outside is not affected at all (see figure 7.8).

We have also tried the scheme implemented in ref. [47], i.e. a linear extrapolation, but we have discovered that it can produce wrong results when shock waves are present (see figure 7.9). This happens because this type of boundary conditions is not adequate with non-smooth flows. Indeed before the fast right-going shock hits the excision boundary the two different methods give the same results but the solution is clearly incorrect after the shock has crossed the excision boundary when an extrapolation is used.

7.3.3 Magnetized spherical accretion

This second test proves the ability of the code to maintain a static solution in a curved space-time. We consider the spherical accretion of a perfect fluid with a radial magnetic field onto a Schwarzschild black hole. The solution to this problem is already known for the unmagnetized case but it can be demonstrated that the solution is not affected if one adds a radial magnetic field [39]. The initial setup is the same used in refs. [39, 64, 47, 12] and consists of a perfect fluid obeying a polytropic EOS with $\Gamma = 4/3$. The critical radius of the solution is located at $r_c = 8.0$ and the rest mass density at r_c is $\rho_c = 6.25 \cdot 10^{-2}$. These parameters are sufficient to provide the full description of the accretion onto a solar mass Schwarzschild black hole as described in ref. [104]. We solve the problem on a cartesian grid going from $x^i = 0$ to $x^i = 11$. To avoid problems at the horizon, located at $r = 2$, we write the metric in ingoing Eddington-Finkelstein coordinates. The excision boundary has the shape of a cubical box of length 1 so that the domain $[0, 1] \times [0, 1] \times [0, 1]$ is excluded from the evolution. In this case we use the same boundary condition adopted by Duez *et al.* [47], i.e. a linear extrapolation, which in this case gives better results than the zeroth-order extrapolation; e.g for a run with $b^2/\rho \approx 25$ the latter gives an error $\approx 3\%$ larger. The order of accuracy of the code is measured using the L_1-norm of the relative error on the rest mass density (7.32).

In figure 7.10 we plot $\delta\rho/\rho$ computed at time $t = 100M$ for two different resolutions, 100^3 and 150^3; the error form the latter is multiplied by 1.5^2 so that if the code were second order convergent the two curves should overlap. From this figure one can easy see that the code is not perfectly second-order convergent especially for values of b^2/ρ greater than 4, as already found by Duez *et al.* [47]. We have investigated the origin of this problem

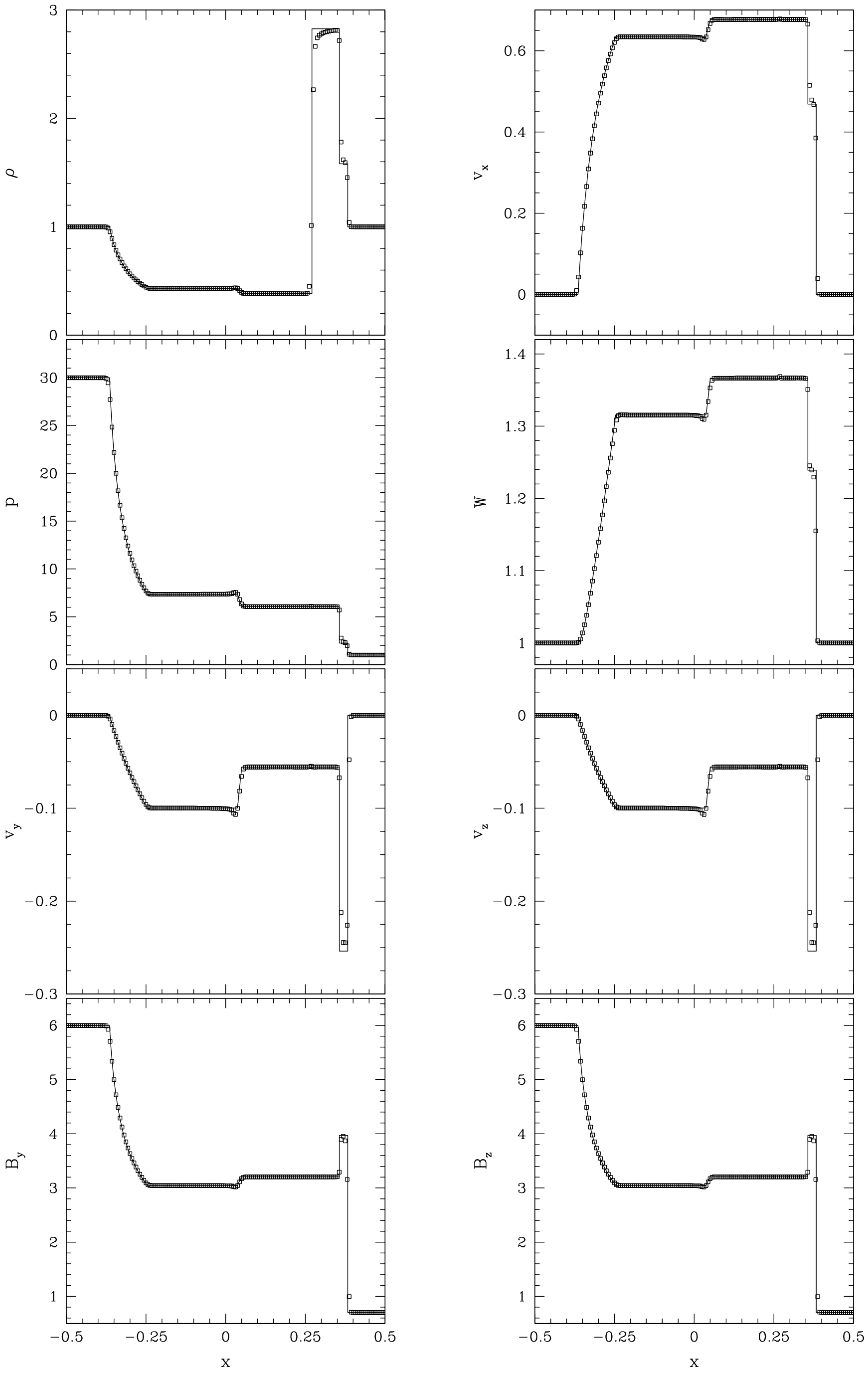

Figure 7.3 Numerical solution of the test number 2 of Balsara at a time $t = 0.4$. The solid line represent the exact solution while the open squares the numerical one. The solution is composed of two left-going fast and slow rarefactions, of a contact discontinuity and of two right-going fast and slow shocks. (Only 160 of the 1600 data points used in the simulation are drawn)

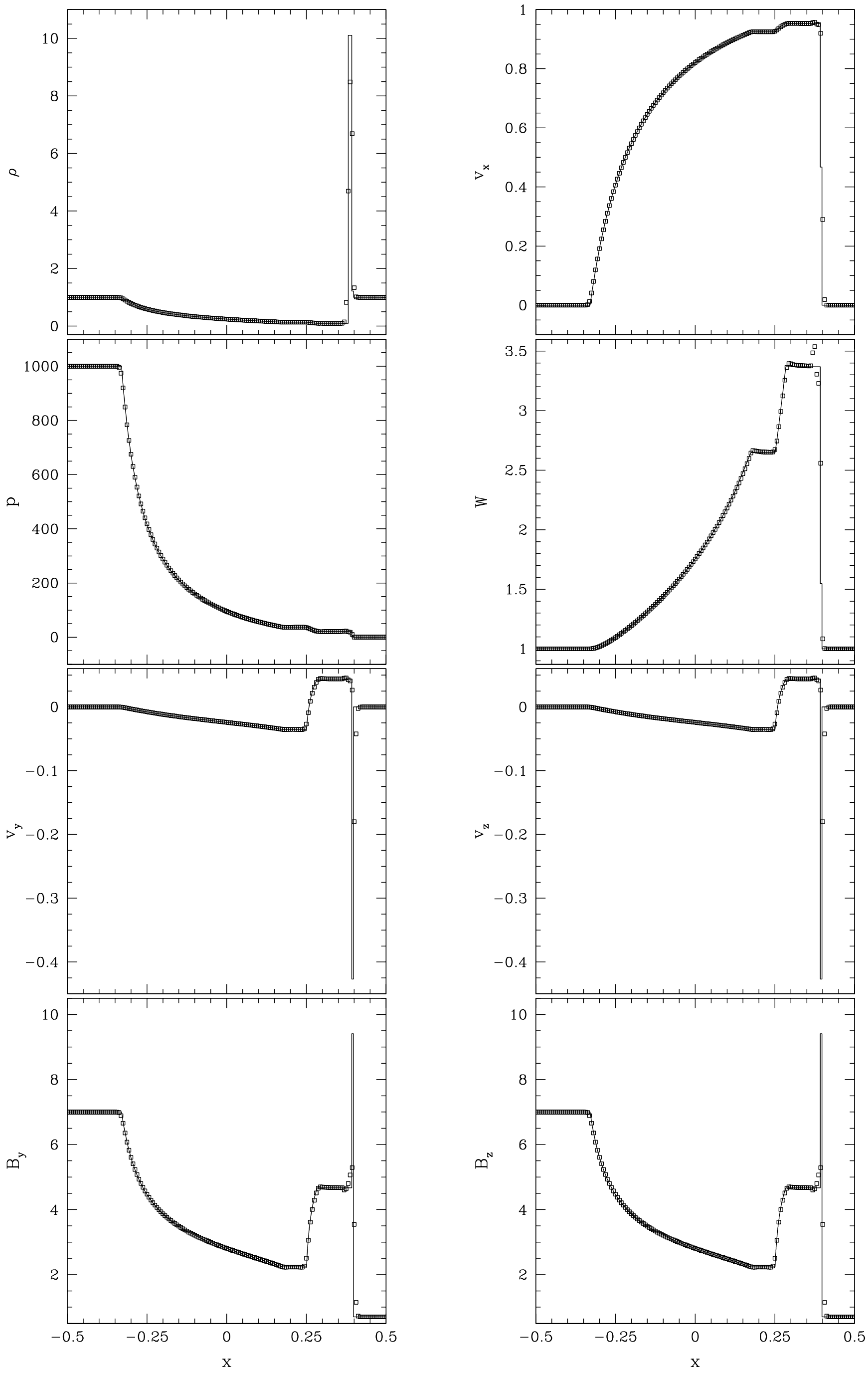

Figure 7.4 Numerical solution of the test number 3 of Balsara at a time $t = 0.4$. The solid line represent the exact solution while the open squares the numerical one. The solution is composed of two left-going fast and slow rarefactions, of a contact discontinuity and of two right-going fast and slow shocks. (Only 160 of the 1600 data points used in the simulation are drawn)

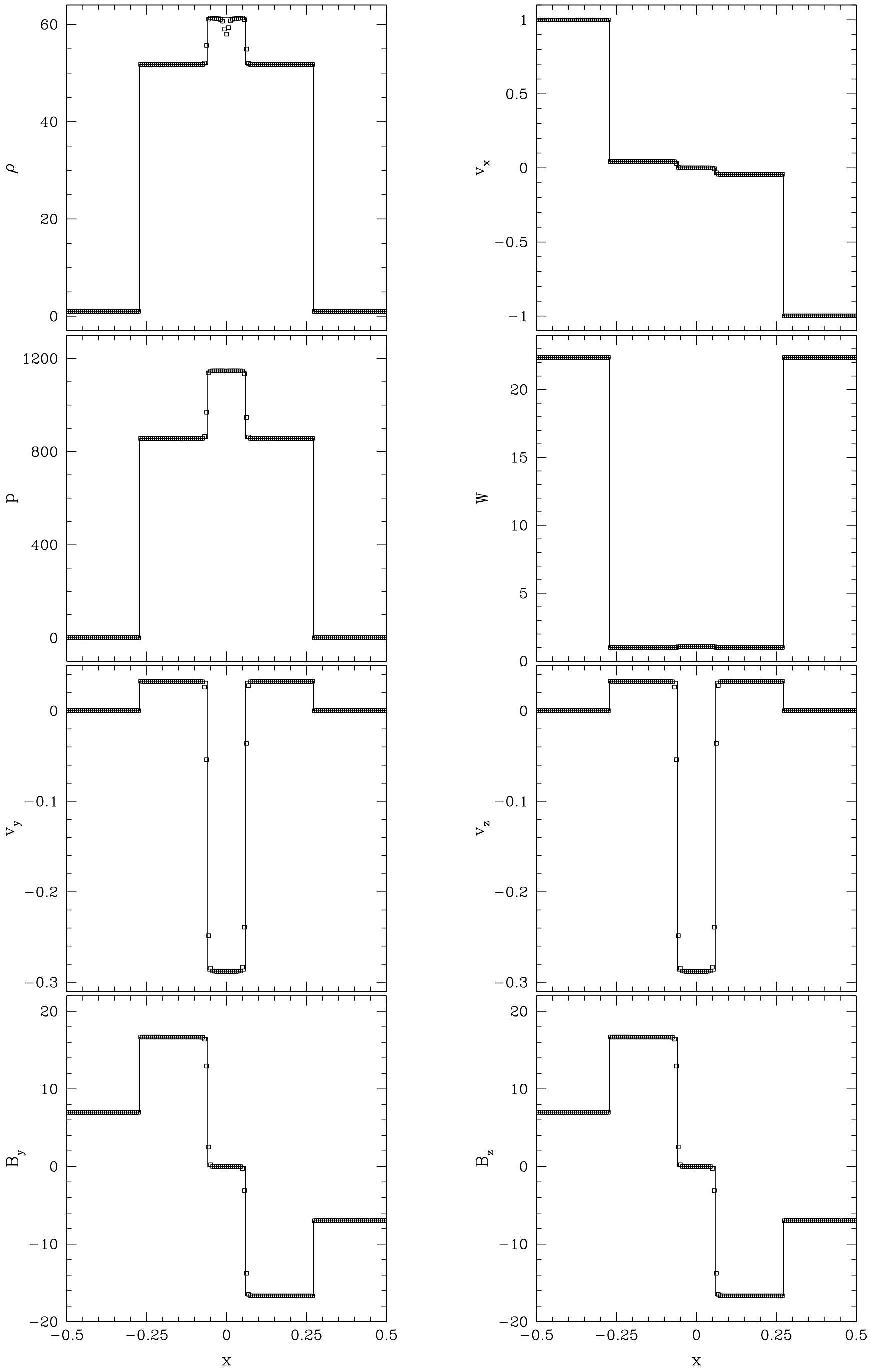

Figure 7.5 Numerical solution of the test number 4 of Balsara at a time $t = 0.4$. The solid line represent the exact solution while the open squares the numerical one. The solution is composed of two left-going fast and slow shocks and of two right-going fast and slow shocks. (Only 160 of the 1600 data points used in the simulation are drawn)

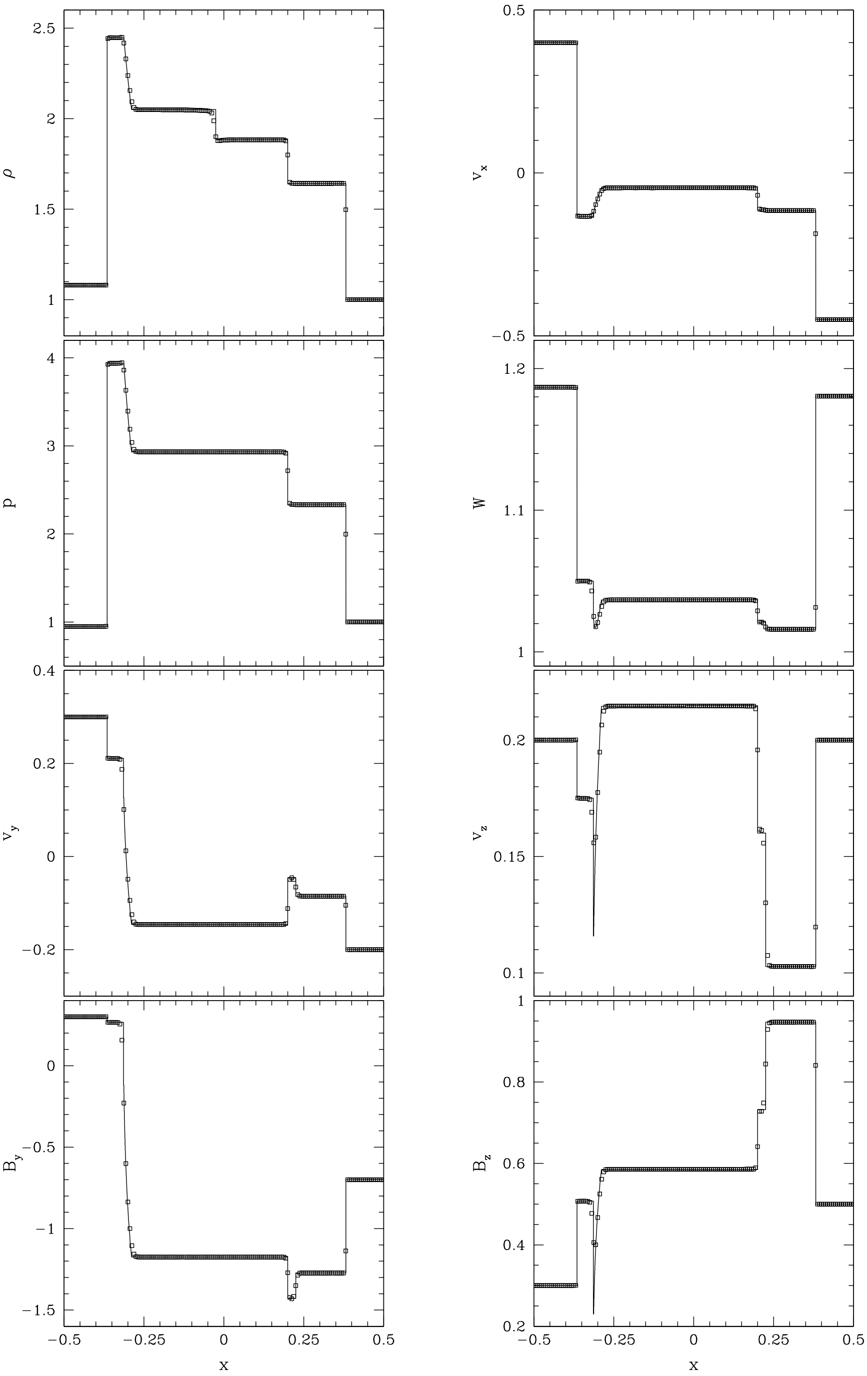

Figure 7.6 Numerical solution of the test number 5 of Balsara at a time $t = 0.55$. The solid line represent the exact solution while the open squares the numerical one. The solution is composed of a left-going fast shock, of a left-going Alfvèn discontinuity, of a left-going slow rarefaction, of a contact discontinuity, of a right-going slow shock, of a right-going Alfvèn discontinuity and of a right-going fast shock. (Only 160 of the 1600 data points used in the simulation are drawn)

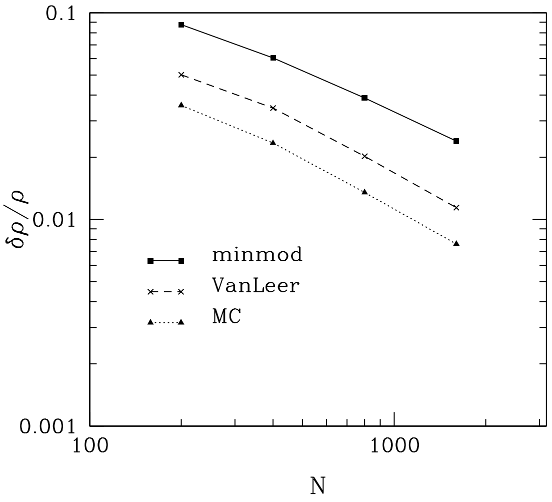

Figure 7.7 L_1-norm of the relative error on the rest mass density ρ for test number 2 of Balsara as a function of the number of points N and for the three different slope limiters implemented in our code.

and we discovered that most of the deviation from the second order convergence is present in the gridpoints near the excision boundary, i.e. for $x^i \in [1,2]$, while in the rest of the domain the code is second order convergent as expected (see figure 7.11).

7.3.4 Evolution of a stable magnetized Neutron Star

We now consider the evolution of a stable magnetized neutron star. As this is a static solution, no evolution is expected; however small truncation errors can perturb the initial data producing small oscillations as already shown in ref. [16] for the unmagnetized case.

The initial conditions are computed using the code developed by Bocquet *et al.* [27] which exactly solves the full set of Einstein and Maxwell equations assuming that the model is axisymmetric and with a poloidal magnetic field with the dipole moment aligned along the rotation axis. This code is used to build initial configurations for uniformly rotating magnetized neutron stars with different angular velocities and magnetic field strengths. Figures 7.12 and 7.13 show the magnetic field lines for the two non-rotating models described in table 7.2. In the case of star C2, where the magnetic field is more intense with $p_{mag}/p_{gas} = 0.1$, the structure of the star deviates from spherical symmetry.

In this test we consider star C1 which is a non rotating magnetized neutron star with mass $M = 1.3M_\odot$ and with a central value of the magnetic field $B_c = 2.4 \times 10^{14}G$, corresponding to $\beta = p_{\rm mag}/p_{\rm gas} = 10^{-6}$. A polytropic equation of state with $\Gamma = 2$ and $K = 372$ was used both for the computation of the initial model both during the evolution. We performed two series of runs, in the first one we did not evolve the metric using the

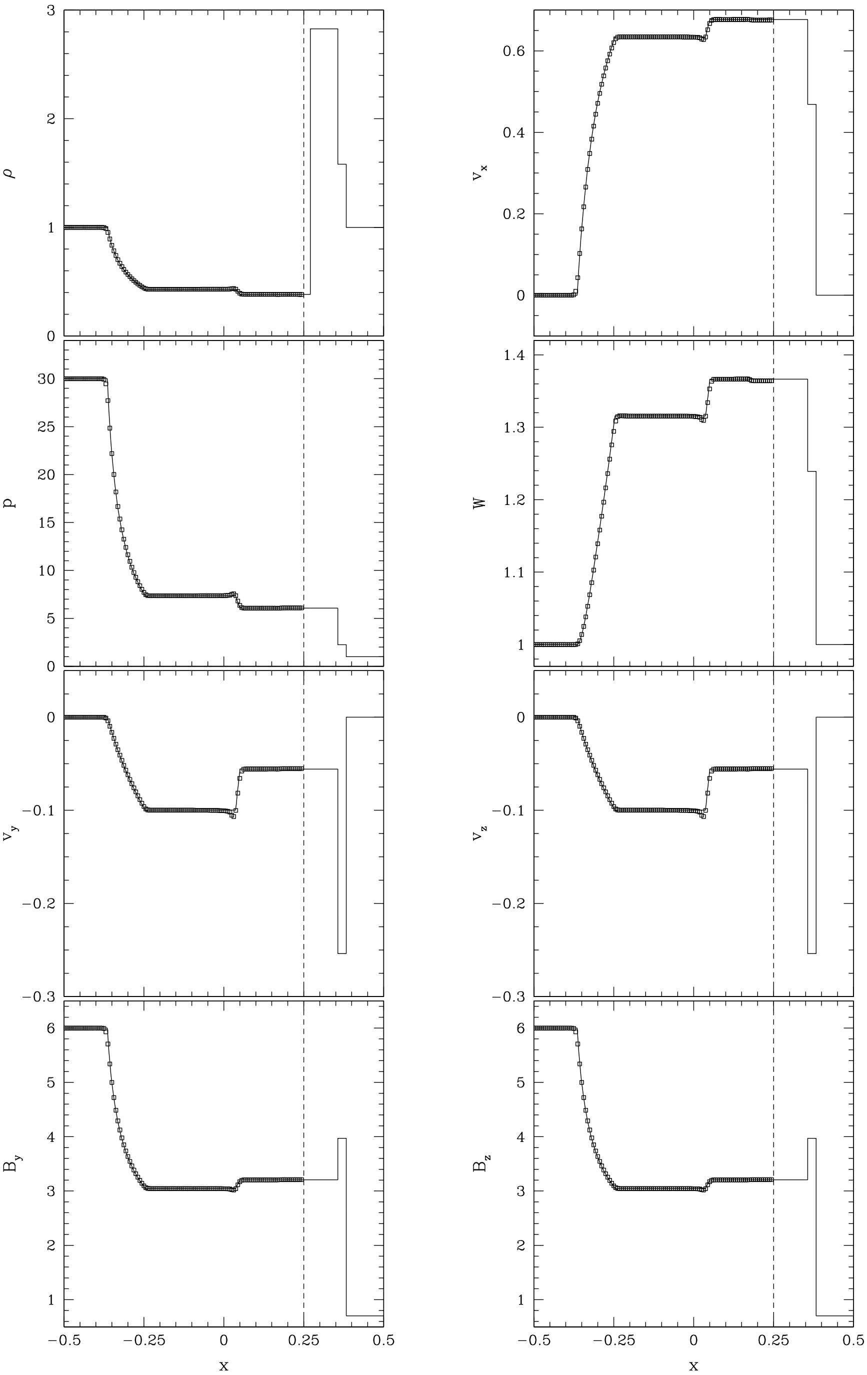

Figure 7.8 Numerical solution of the test number 2 of Balsara at a time $t = 0.4$ with an excision boundary (dashed vertical line) located at $x = 0.25$; the region at the right of this boundary is not evolved. The solid line represent the exact solution while the open squares the numerical one. The solution is composed of two left-going fast and slow rarefactions, of a contact discontinuity and of two right-going fast and slow shocks. (Only 160 of the 1600 data points used in the simulation are drawn)

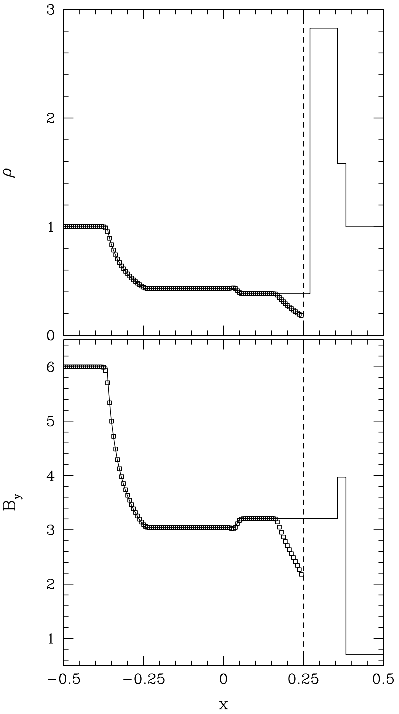

Figure 7.9 Numerical solution of the test number 2 of Balsara at a time $t = 0.4$ with an excision boundary (dashed vertical line) located at $x = 0.25$; the region at the right of this boundary is not evolved. In this case the values of the different variables at the excision boundary were obtained with a linear extrapolation. The solid line represents the exact solution while the open squares the numerical one. The solution is composed of two left-going fast and slow rarefactions, of a contact discontinuity and of two right-going fast and slow shocks. (Only 160 of the 1600 data points used in the simulation are drawn)

Table 7.2. Initial data for the different magnetized stars

Model	ρ_c	r_p/r_e	M	R_e	B_c (GT)	β
C1	9.74×10^{-5}	1.00	1.33	20.7	23.7	1.14×10^{-6}
C2	9.74×10^{-5}	0.87	1.44	21.5	7534	1.15×10^{-1}

Note. — The different columns refer, respectively, to: the central rest mass density ρ_c, the ratio of the polar to the equatorial coordinate radii r_p/r_e, the total mass M, the equatorial radius R_e, the value of the magnetic field at the center B_c (in GT), the value of $\beta = p_{mag}/p_{gas}$ computed at the center of the star. All thee initial models have been computed with a polytropic EOS with $K = 372$ and $N = 1$.

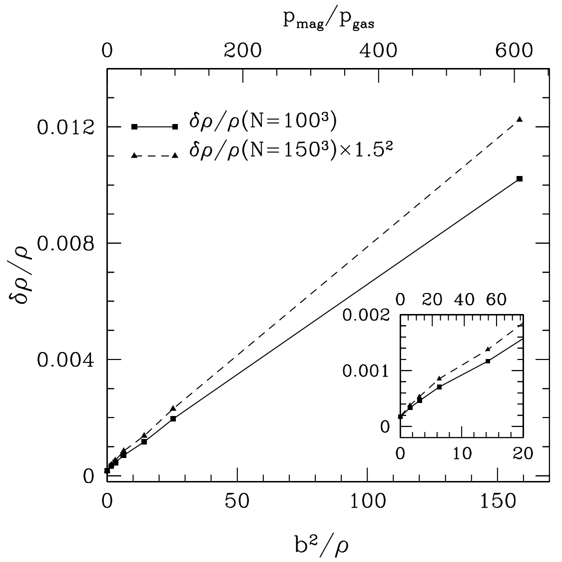

Figure 7.10 Relative error of the rest mass density for the magnetized spherical accretion test with different values for the magnetic field. Results from 100^3 and 150^3 grid runs are compared at time $t = 100M$. The $\delta\rho/\rho$ computed with 150^3 is multiplied by 1.5^2 so that in the second order convergence regime the two line should overlap.

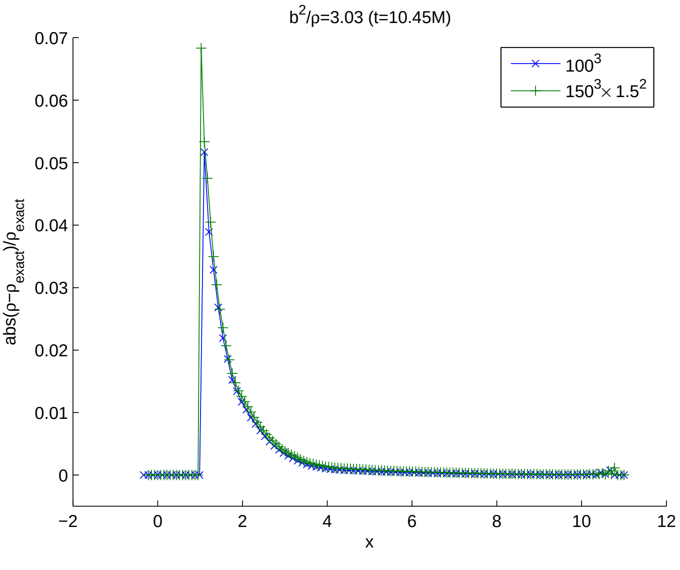

Figure 7.11 Values on the x axis of the relative error on ρ for $b^2/\rho = 3$. From this plot it is possible to see that the code is not second-order convergent only in the first few points outside the excision zone located at $x = 1$.

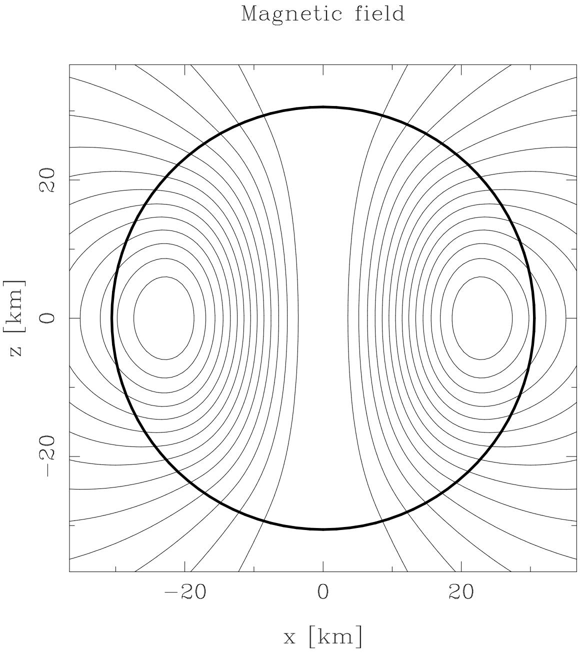

Figure 7.12 Magnetic field lines of star C1. The solid thick line represents the star surface.

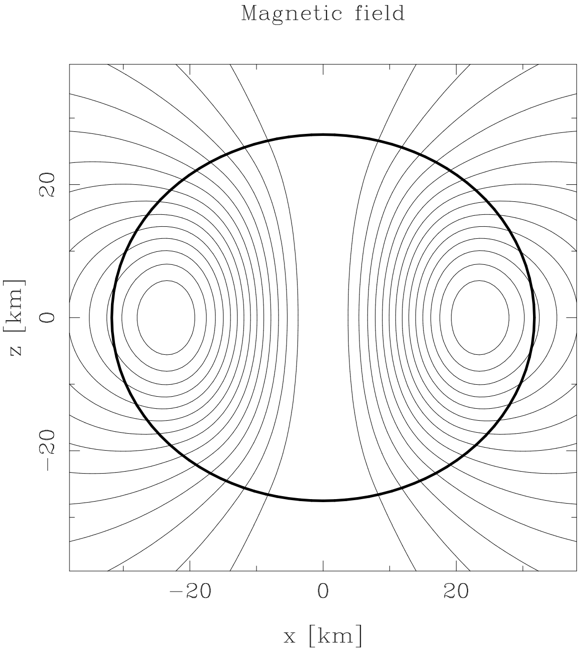

Figure 7.13 Magnetic field lines of star C2. The solid thick line represents the star surface; note the effect of the intense magnetic field, $p_{mag}/p_{gas} = 0.1$, on the star surface. Even if the star is not rotating, its shape is far from being spherical.

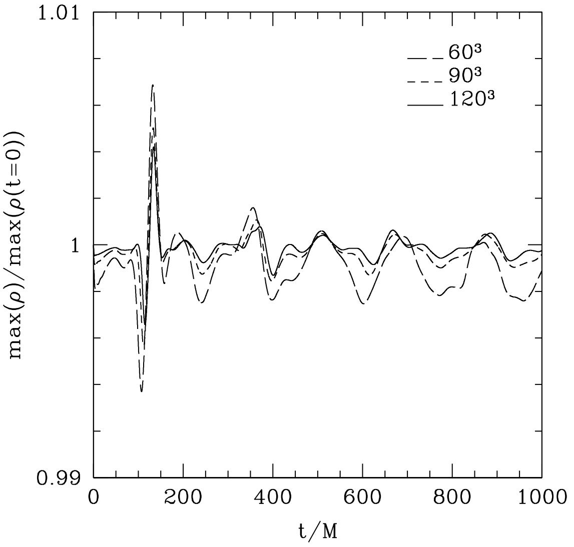

Figure 7.14 Maximum of the rest-mass density ρ normalized at $t = 0$ as a function of time for star C1. The different lines refer to different resolutions: $N = 60^3$ (long dashed line), $N = 90^3$ (dashed line), $N = 120^3$ (solid line). The Cowling approximation was used.

Cowling approximation, *i.e.* we hold the metric fixed to its initial value. In the second one we solved also the Einstein equations for the spacetime and we compared the results between the two runs.

In figure 7.14 we show the maximum of the rest-mass density ρ normalized at $t = 0$ for three different resolutions, $N = 60^3$, 90^3, 120^3 in the Cowling approximation. Because the oscillations are triggered by truncation errors one expects that these should be lower as the resolution increases and indeed we observe that the amplitude decrease increasing the resolution. The three different resolutions show also a similar behavior with the same location of the first oscillations indicating that we are in a convergent regime. In fig. 7.15 we plot the result for a longer run with a resolution of $N = 90^3$.

We performed also another series of run with the same model C1 and the same resolutions in the case in which also the Einstein equations for the metric are solved. The maximum of the rest-mass density for the three different resolutions is showed in figure 7.16, while in figure 7.17 we show only the result obtained with $N = 90^3$. To give a better view of the convergence of our code we also show in figure 7.18 the L_2 norm of the Hamiltonian constraint as a function of time for the three resolutions used. As expected it decreases for higher resolutions.

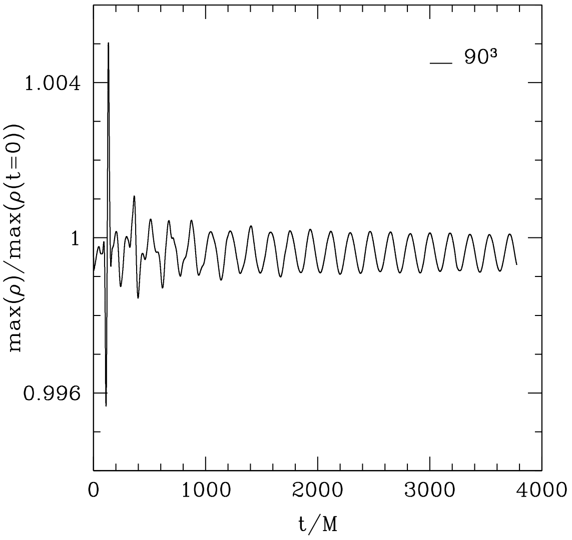

Figure 7.15 Evolution of the maximum of the rest-mass density ρ normalized at $t = 0$ for star C1 with a resolution of $N = 90^3$ points. The Cowling approximation was used.

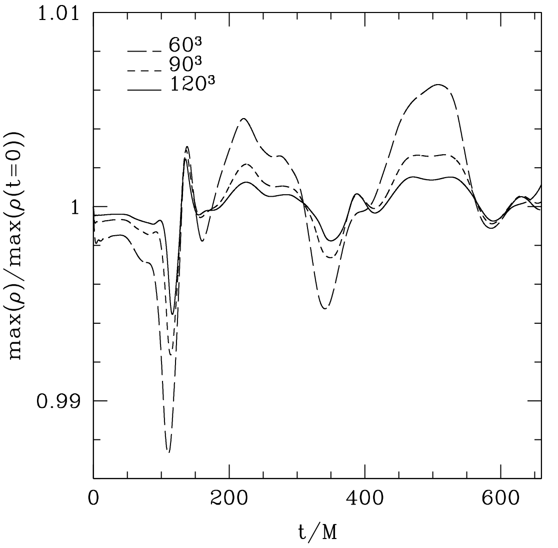

Figure 7.16 Maximum of the rest-mass density ρ normalized at $t = 0$ as a function of time for star C1. The different lines refer to different resolutions: $N = 60^3$ (long dashed line), $N = 90^3$ (dashed line), $N = 120^3$ (solid line). In this case also the spacetime was evolved.

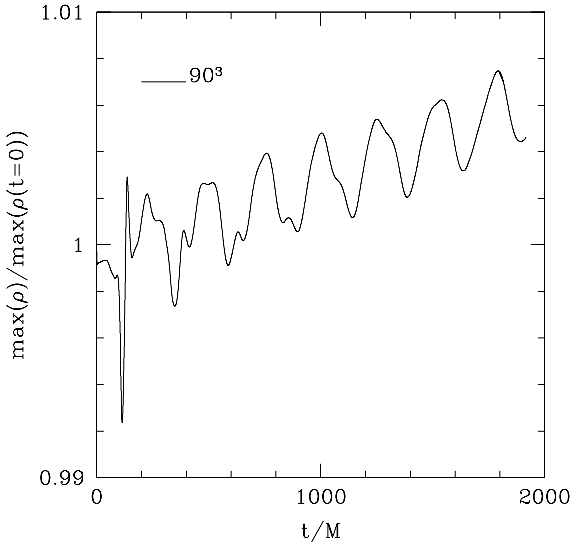

Figure 7.17 Evolution of the maximum of the rest-mass density ρ normalized at $t = 0$ for star C1 with a resolution of $N = 90^3$ points. In this case also the spacetime was evolved.

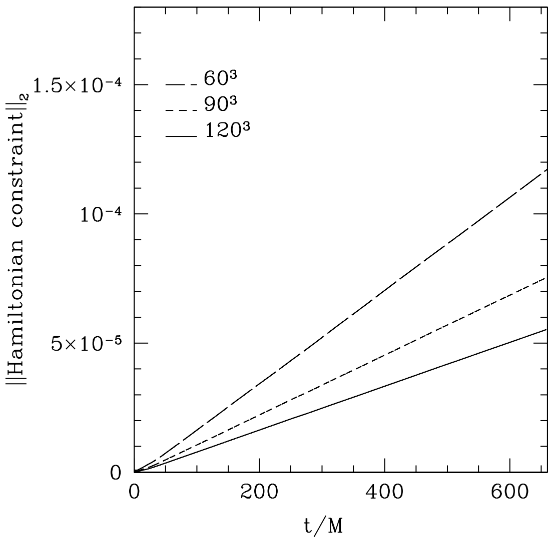

Figure 7.18 The L_2 norm of the Hamiltonian constraint for star C1 with three different resolutions: $N = 60^3$ (long dashed line), $N = 90^3$ (dashed line), $N = 120^3$ (solid line).

Chapter 8

Conclusions

The last years have seen a number of breakthroughs in numerical relativity both in vacuum and non-vacuum spacetimes and the progress in this field has never been as promising as it is now. This is related to the strong effort made by several groups in the world with the aim of obtaining a more realistic description of the dynamics of a large set of astrophysical objects and of predicting the gravitational-wave signal emitted by them.

In general relativistic hydrodynamics several improvements in our understanding of different astrophysical scenario were made possible by the development and use of the `Whisky` code which is now a well known numerical code used by different groups (among them AEI, SISSA, Universities of Parma, Thessaloniki and Valencia). As already mentioned in the Introduction, it has been applied to the study of the collapse of uniformly rotating neutron stars [16, 17], of head-on collision of two neutron stars or of a neutron star with a black hole [98] and of dynamical barmode instability [14].

In this Thesis we have extended the results obtained in refs. [16, 17] for the gravitational collapse of uniformly rotating neutron stars to the case in which differential rotation is included in the initial models. We have performed a study of the unstable configurations and we discovered that supra-Kerr models, *i.e.* with $J/M^2 > 1$, seem to exist only in dynamically stable configurations; conversely, all configurations that are dynamically unstable have been found to be sub-Kerr, *i.e.* with $J/M^2 < 1$. We have performed numerical simulations of the collapse of unstable sub-Kerr models to black-holes and extracted for the first time the gravitational-wave signal emitted by them. Interestingly, it has been found to be at least one order of magnitude larger than the one generated by the collapse of uniformly rotating neutron stars. We consider this a very important and promising result as it proposes these sources as detectable also at larger distances and thus with larger event rates. These objects are indeed thought to be formed by the merging of binary NS systems and the event rate for this kind of events is considerably low, *i.e.* $\approx 10^{-5}$ per year, if we limit to observations in our Galaxy but it can grow to up ≈ 1 event per year if we include a region of space within a distance of about 100Mpc (see for example refs. [117, 152, 37]).

Future investigations will be also dedicated to a more detailed study of the relation between the energy $\Delta E/M$ carried away from gravitational waves and the degree of differential rotation $\hat{A}$ and angular momentum J/M^2. We have also studied the final fate of the collapse of a supra-Kerr model when its pressure is artificially reduced by 99%, observing a different dynamics with the formation of strong shocks and non-axisymmetric instabilities, eventually leading to a stable and differentially rotating neutron star. We have also confirmed that black holes are formed only in the gravitational collapse of sub-Kerr models and not for supra-Kerr ones.

With the aim of extending all the work done so far in general relativistic hydrodynamics with the `Whisky` code to the case in which magnetic fields are present, we have developed `WhiskyMHD`, a new full general relativistic magnetohydrodynamical code based on the conservative formulation of GRMHD equations and on the use of HRSC methods. As already pointed out in the Introduction magnetic fields play a very important role in many astrophysical scenarios, such as γ-ray bursts, and this code will then extend the range of possible astrophysical applications that were already possible with the `Whisky` code.

Being code validation an important aspect of the development of any numerical code, we grew concerned about the fact that most of the numerical codes solving the GRMHD equations were not tested in a quantitative way. This was essentially due to the lack of a general exact solution of the Riemann problem in relativistic MHD. This was to be contrasted with the corresponding situation in GRHD, where a number of different approaches to the exact solution of the Riemann problem were known and they were of great importance, for example, in testing `Whisky`.

The exact solution of the Riemann problem in relativistic MHD was searched by different groups for a long time and only recently it was possible to obtain an exact solution but in a very special case only [125]. The work presented in this Thesis provides for the first time a procedure for the exact and general solution of the Riemann problem in relativistic MHD. Our method is based on the important idea of using a mixed approach in the search for the solution, using not only the total pressure, as done in the relativistic hydrodynamical case, but also the tangential components of the magnetic field as the set of unknowns that determines the solution. With this method we were able to compute the exact solutions of most of the Riemann problems already used as standard tests in relativistic MHD. The version of the code used to compute the exact solution is public available and it is now used by several groups in the world to test both special and general relativistic MHD codes (for the first applications see for example refs. [105, 10]).

The exact Riemann solver has been a valuable tool also to test our `WhiskyMHD` code which has proved to be able to solve the full set of Riemann problems with a good agreement with our exact solution for all the type of waves present in MHD. One of these solutions was also used to test our excision algorithm which has proved to work also in curved spacetime in the case of spherical accretion onto a Schwarzschild black hole.

Because one of the main future applications of `WhiskyMHD` will be the study of the dynamics of magnetized neutron stars, we have also coupled `WhiskyMHD` with the code developed in ref. [27] and which exactly solves the full set of Einstein and Maxwell equations for axisymmetric models with a poloidal magnetic field with the dipole moment aligned along the rotation axis. With this code we were able to compute several initial data for uniformly rotating neutron stars with different magnetic field strengths. As a last test of our code, which can be also considered as a first astrophysical application, we have started a study of the oscillation of a stable magnetized NS. This test was performed both in a fixed spacetime, *i.e.* using the so called Cowling approximation, and evolving also the Einstein equations for the field variables. We have shown that in both cases our code is convergent and able to evolve magnetized NS with a magnetic field not confined only to the interior of the star.

In future we plan to extend the study on the oscillations of rotating and non-rotating neutron stars with a detailed analysis of the effect of magnetic fields on the frequency of oscillations. It is important to note that only recently some results were obtained with perturbative studies [137], even if with the use of the Cowling approximation, and so our code may provide the first full general relativistic computation of these frequencies. The comparison between the numerical results and the frequencies observed in objects such as the soft gamma repeaters can provide useful information on the mass and magnetic field intensity of magnetars.

We will concentrate also on the study of the collapse of uniformly rotating magnetized neutron stars with the aim of extending further the work done in refs. [16, 17] and highlight the role that this process may have in the phenomenology of short GRBs. We will especially provide the gravitational-wave signal emitted by these sources and we will investigate the influence the magnetic field may have on it.

Another important application will be the extension of the study, presented in this thesis, of the collapse of differentially rotating neutron stars to include the effects of magnetic fields. These objects are particularly interesting not only because they are very good candidates for short γ-ray bursts but also because, as we have shown in this thesis, they are very powerful sources of gravitational waves. It is then important to study the effects that magnetic field can have both on the frequencies and on the amplitudes of GW and also to relate them with γ-ray bursts signals.

Overall, we expect that the `WhiskyMHD` code, just like the `Whisky` code, will be an useful *"astrophysical laboratory"*, increasing significantly our current knowledge among the most fascinating objects in the Universe.

Bibliography

[1] M. Abramowitz and A. Stegun. *Handbook of Mathematical Functions.* Dover, 1965.

[2] M. Alcubierre. The appearance of coordinate shocks in hyperbolic formulations of general relativity. *Phys. Rev. D*, 55:5981–5991, 1997.

[3] M. Alcubierre, G. Allen, B. Brügmann, E. Seidel, and W. Suen. Towards an understanding of the stability properties of the 3+1 evolution equations in general relativity. *Phys. Rev. D*, 62:124011, 2000.

[4] M. Alcubierre, B. Brügmann, P. Diener, M. Koppitz, D. Pollney, E. Seidel, and R. Takahashi. Gauge conditions for long-term numerical black hole evolutions without excision. *Phys. Rev. D*, 67:084023, 2003.

[5] M. Alcubierre, B. Brügmann, T. Dramlitsch, J. Font, P. Papadopoulos, E. Seidel, N. Stergiuolas, and R. Takahashi. Towards a stable numerical evolution of strongly gravitating systems in general relativity: The conformal treatments. *Phys. Rev. D*, 62:044034, 2000.

[6] M. Alcubierre, B. Brügmann, T. Dramlitsch, J.A. Font, P. Papadopoulos, E. Seidel, N. Stergioulas, and R. Takahashi. Towards a stable numerical evolution of strongly gravitating systems in general relativity: The conformal treatments. *Phys. Rev. D*, 62:044034, 2000.

[7] M. Alcubierre, B. Brügmann, D. Pollney, E. Seidel, and R. Takahashi. Black hole excision for dynamic black holes. *Phys. Rev. D*, 64:61501 (R), 2001.

[8] M. Alcubierre and J. Massó. Pathologies of hyperbolic gauges in general relativity and other field theories. *Phys. Rev. D*, 57(8):4511–4515, 1998.

[9] M. A. Aloy, J. M. Ibáñez, J. M. Martí, and E. Müller. Genesis: A high-resolution code for three-dimensional relativistic hydrodynamics. *ApJS*, 122:151, 1999.

[10] M. Anderson, E. Hirschmann, S. L. Liebling, and D. Neilsen. Relativistic MHD with Adaptive Mesh Refinement. 2006.

[11] A. M. Anile. *Relativistic Fluid and Magneto-Fluids.* Cambridge University Press, 1989.

[12] L. Anton, O. Zanotti, J. A. Miralles, J. M. Martí, J. M. Ibánez, J. A. Font, and J. A. Pons. Numerical 3+1 general relativistic magnetohydrodynamics: A local characteristic approach. *Astrophys. J.*, 637:296–312, 2006.

[13] R. Arnowitt, S. Deser, and C. W. Misner. The dynamics of general relativity. In L. Witten, editor, *Gravitation: An Introduction to Current Research*, pages 227–265. John Wiley, New York, 1962.

[14] L. Baiotti, R. De Pietri, G. M. Manca, and L. Rezzolla. Accurate simulations of the dynamical barmode instability in full general relativity. *submitted to Phys. Rev. D*, 2006.

[15] L. Baiotti, I. Hawke, P. Montero, and L. Rezzolla. A new three-dimensional general-relativistic hydrodynamics code. In R. Capuzzo-Dolcetta, editor, *Computational Astrophysics in Italy: Methods and Tools*, volume 1, page 327, Trieste, 2003. Mem. Soc. Astron. It. Suppl.

[16] L. Baiotti, I. Hawke, P. J. Montero, F. Löffler, L. Rezzolla, N. Stergioulas, J. A. Font, and E. Seidel. Three-dimensional relativistic simulations of rotating neutron-star collapse to a kerr black hole. *Phys. Rev. D*, 71:024035, 2005.

[17] L. Baiotti, I. Hawke, L. Rezzolla, and E. Schnetter. Gravitational-Wave Emission from Rotating Gravitational Collapse in Three Dimensions. *Physical Review Letters*, 94:131101, 2005.

[18] L. Baiotti and L. Rezzolla. Challenging the paradigm of singularity excision in gravitational collapse. *Physical Review Letters*, 97:141101, 2006.

[19] J. Balakrishna, G. Daues, E. Seidel, W.-M. Suen, M. Tobias, and E. Wang. Coordinate conditions in three-dimensional numerical relativity. *Class. Quantum Grav.*, 13:L135–L142, 1996.

[20] D. S. Balsara. Total variation diminishing scheme for relativistic magnetohydrodynamics. *ApJS*, 132:83–101, 2001.

[21] D. S. Balsara and D. S. Spicer. A staggered mesh algorithm using high order godunov fluxes to ensure solenoidal magnetic fields in magnetohydrodynamic simulations. *J. Comp. Phys.*, 149:270–292, 1999.

[22] F. Banyuls, J. A. Font, J. M. Ibánez, J. M. Martí, and J. A. Miralles. Numerical 3+1 general relativistic hydrodynamics: A local characteristic approach. *Astrophys. J.*, 476:221–231, 1997.

[23] J. M. Bardeen and R. V. Wagoner. Relativistic disks. i. uniform rotation. *Astrophys. J.*, 167:359, 1971.

[24] T. W. Baumgarte and S. L. Shapiro. Numerical integration of einstein's field equations. *Phys. Rev. D*, 59:024007, 1999.

[25] T. W. Baumgarte, S. L. Shapiro, and M. Shibata. On the Maximum Mass of Differentially Rotating Neutron Stars. *Astrophys. J.*, 528:L29–L32, 2000.

[26] K. Belczynski, T. Bulik, and B. Rudak. Study of Gamma-Ray Burst Binary Progenitors. *Astrophys. J.*, 571:394–412, 2002.

[27] M. Bocquet, S. Bonazzola, E. Gourgoulhon, and J. Novak. Rotating neutron star models with a magnetic field. *A&A*, 301:757–775, 1995.

[28] C. Bona, T. Ledvinka, C. Palenzuela, and M. Zacek. A symmetry-breaking mechanism for the z4 general-covariant evolution system. *Phys. Rev. D*, 69:064036, 2003.

[29] C. Bona, J. Massó, E. Seidel, and J. Stela. New Formalism for Numerical Relativity. *Phys. Rev. Lett.*, 75:600–603, 1995.

[30] J. U. Brackbill and D. C. Barnes. The effect of nonzero $\nabla \cdot B$ on the numerical solution of the magnetohydrodynamic equations. *J. Comp. Phys.*, 35:426–430, 1980.

[31] M. Brio and C.-C. Wu. An upwind differencing scheme for the equations of ideal magnetohydrodynamics. *J. Comp. Phys.*, 75:400, 1988.

[32] `Cactus`. `www.cactuscode.org`.

[33] K. Camarda and E. Seidel. Three-dimensional simulations of distorted black holes: Comparison with axisymmetric results. *Phys. Rev. D*, 59:064019, 1999.

[34] P. Colella and P. R. Woodward. The piecewise parabolic method (ppm) for gas-dynamical simulations. *J. Comput. Phys.*, 54:174–201, 1984.

[35] G. B. Cook, S. L. Shapiro, and S. A. Teukolsky. Spin-up of a rapidly rotating star by angular momentum loss: effects of general relativity. *Astrophys. J.*, 398:203–223, 1992.

[36] S. F. Davis. A simplified tvd finite difference scheme via artificial viscosity. *SIAM J. Sci. Stat. Comput.*, 8:1–18, 1987.

[37] J. A. de Freitas Pacheco, T. Regimbau, S. Vincent, and A. Spallicci. Expected Coalescence Rates of Ns-Ns Binaries for Laser Beam Interferometers. *Intern. Journal of Modern Physics D*, 15:235–249, 2006.

[38] J.-P. De Villiers and J. F. Hawley. Three-dimensional Hydrodynamic Simulations of Accretion Tori in Kerr Spacetimes. *Astrophys. J.*, 577:866–879, 2002.

[39] J.-P. De Villiers and J. F. Hawley. A numerical method for general relativistic magnetohydrodynamics. *Astrophys. J.*, 589:458–480, 2003.

[40] J.-P. De Villiers, J. F. Hawley, and J. H. Krolik. Magnetically driven accretion flows in the kerr metric. i. models and overall structure. *Astrophys. J.*, 599:1238–1253, 2003.

[41] J.-P. De Villiers, J. F. Hawley, J. H. Krolik, and S. Hirose. Magnetically driven accretion in the kerr metric. iii. unbound outflows. *Astrophys. J.*, 620:878–888, 2005.

[42] L. Del Zanna, N. Bucciantini, and P. Londrillo. An efficient shock-capturing central-type scheme for multidimensional relativistic flows. ii. magnetohydrodynamics. *A&A*, 400:397, 2003.

[43] R. Donat, J. A. Font, J. M. Ibánez, and A. Marquina. A flux-split algorithm applied to relativistic flows. *Journ. Comput. Phys.*, 146:58–81, 1998.

[44] R. Donat and A. Marquina. Capturing shock reflections: an improved flux formula. *Journ. Comput. Phys.*, 125:42, 1996.

[45] M. D. Duez, Y. T. Liu, S. L. Shapiro, M. Shibata, and B. C. Stephens. Collapse of Magnetized Hypermassive Neutron Stars in General Relativity. *Physical Review Letters*, 96:031101, 2006.

[46] M. D. Duez, Y. T. Liu, S. L. Shapiro, M. Shibata, and B. C. Stephens. Evolution of magnetized, differentially rotating neutron stars: Simulations in full general relativity. *Phys. Rev. D*, 73:104015, 2006.

[47] M. D. Duez, Y. T. Liu, S. L. Shapiro, and B. C. Stephens. Relativistic magnetohydrodynamics in dynamical spacetimes: Numerical methods and tests. *Phys. Rev. D*, 72:024028, 2005.

[48] M. D. Duez, S. L. Shapiro, and H. J Yo. Relativistic hydrodynamic evolutions with black hole excision. *Phys. Rev. D*, 69:104106, 2004.

[49] D. Eichler, M. Livio, T. Piran, and D. N. Schramm. Nucleosynthesis, neutrino bursts and gamma-rays from coalescing neutron stars. *Nature*, 340:126–128, 1989.

[50] B. Einfeldt. On godunov-type methods for gas dynamics. *SIAM J. Numer. Anal.*, 25(2):294, 1988.

[51] C. R. Evans and J. F. Hawley. Simulation of magnetohydrodynamic flows: A constrained transport method. *Astrophys. J.*, 332:659, 1988.

[52] S. A. E. G. Falle and S. S. Komissarov. On the inadmissibility of non-evolutionary shocks. *J. Plasma Physics*, 65:29, 2001.

[53] S. A. E. G. Falle, S. S. Komissarov, and P. Joarder. A multidimensional upwind scheme for magnetohydrodynamics. *MNRAS*, 297:265, 1998.

[54] L. S. Finn, S. D. Mohanty, and J. D. Romano. Detecting an association between gamma ray and gravitational wave bursts. *Phys. Rev. D*, 60:121101, 1999.

[55] É. É. Flanagan and S. A. Hughes. Measuring gravitational waves from binary black hole coalescences. i. signal to noise for inspiral, merger, and ringdown. *Phys. Rev. D*, 57:4535–4565, 1998.

[56] É. É. Flanagan and S. A. Hughes. Measuring gravitational waves from binary black hole coalescences. ii. the waves' information and its extraction, with and without templates. *Phys. Rev. D*, 57:4566–4587, 1998.

[57] J. A. Font. Numerical hydrodynamics in general relativity. *Living Rev. Relativity*, 6:4, 2003. URL (cited on August 16th 2006): http://www.livingreviews.org/lrr-2003-4.

[58] J. A. Font and F. Daigne. The runaway instability of thick discs around black holes - i. the constant angular momentum case. *MNRAS*, 334:383, 2002.

[59] J. A. Font, M. Miller, W. M. Suen, and M. Tobias. Three-dimensional numerical general relativistic hydrodynamics: Formulations, methods, and code tests. *Phys. Rev. D*, 61:044011, 2000.

[60] J. A. Font, N. Stergioulas, and K. D. Kokkotas. Nonlinear hydrodynamical evolution of rotating relativistic stars: Numerical methods and code tests. *Mon. Not. R. Astron. Soc.*, 313:678, 2000.

[61] P. C. Fragile. Quasi-periodic oscillations in relativistic tori. In *Proceedings of the 22nd Texas Meeting on Relativistic Astrophysics*. Stanford University, 2005.

[62] J. L. Friedman, J. R. Ipser, and R. D. Sorkin. Turning-point method for axisymmetric stability of rotating relativistic stars. *Astrophys. J.*, 325:722–724, 1988.

[63] K. O. Friedrichs. Laws of relativistic electromagneto-fluid dynamics. *Commun. Pure Appl. Math.*, 27:749–808, 1974.

[64] C. F. Gammie, J. C. McKinney, and G. Toth. Harm: A numerical scheme for general relativistic magnetohydrodynamics. *Astrophys. J.*, 589:444–457, 2003.

[65] `GEO600`. `http://www.geo600.uni-hannover.de/`.

[66] B. Giacomazzo and L. Rezzolla. The exact solution of the riemann problem in relativistic magnetohydrodynamics. *J. Fluid Mech.*, 562:223–259, 2006.

[67] A. Harten, B. Engquist, S. Osher, and S. R. Chakrabarty. Uniformly high-order accurate essentially nonoscillatory schemes .3. *J. Comput. Phys.*, 71:231–303, 1987.

[68] A. Harten, P. D. Lax, and B. van Leer. On upstream differencing and godunov-type schemes for hyperbolic conservation laws. *SIAM Rev.*, 25:35–61, 1983.

[69] I. Hawke, F. Löffler, and A. Nerozzi. Excision methods for high resolution shock capturing schemes appplied to general relativistic hydrodynamics. *Phys. Rev. D*, 71:104006, 2005.

[70] J. F. Hawley, J. R. Wilson, and L. L. Smarr. A numerical study of nonspherical black hole accretion. i equations and test problems. *Astrophys. J.*, 277:296–311, 1984.

[71] J. F. Hawley, J. R. Wilson, and L. L. Smarr. A numerical study of nonspherical black hole accretion. ii - finite differencing and code calibration. *Astrophys. J.*, 55:211–246, 1984.

[72] S. Hirose, J. H. Krolik, J.-P. De Villiers, and J. F. Hawley. Magnetically driven accretion flows in the kerr metric. ii. structure of the magnetic field. *Astrophys. J.*, 606:1083–1097, 2004.

[73] J. Hjorth, J. Sollerman, P. Møller, J. P. U. Fynbo, S. E. Woosley, C. Kouveliotou, N. R. Tanvir, J. Greiner, M. I. Andersen, A. J. Castro-Tirado, J. M. Castro Cerón, A. S. Fruchter, J. Gorosabel, P. Jakobsson, L. Kaper, S. Klose, N. Masetti, H. Pedersen, K. Pedersen, E. Pian, E. Palazzi, J. E. Rhoads, E. Rol, E. P. J. van den Heuvel, P. M. Vreeswijk, D. Watson, and R. A. M. J. Wijers. A very energetic supernova associated with the γ-ray burst of 29 March 2003. *Nature*, 423:847–850, 2003.

[74] T. Y. Hou and P. G. LeFloch. Why Nonconservative Schemes Cconverge to Wrong Solutions: Error Analysis. *Math. of Comp.*, 62:497–530, 1994.

[75] R. A. Hulse. The discovery of the binary pulsar (PSR 1913+16). *Rev. Mod. Phys.*, 66:699, 1994.

[76] J. M. Ibánez, M. A. Aloy, J. A. Font, J. M. Martí, J. A. Miralles, and J. A. Pons. *Godunov methods: theory and applications.* Kluwer Academic/Plenum Publishers, 2001.

[77] A. Jeffrey. *Magnetohydrodynamics.* Oliver & Boyd, 1966.

[78] A. Jeffrey and T. Taniuti. *Non-linear wave propagation.* Academic Press, New York, 1964.

[79] C. S. Kochanek and T. Piran. Gravitational Waves and gamma -Ray Bursts. *Astrophys. J.*, 417:L17, 1993.

[80] S. Koide. Magnetic extraction of black hole rotational energy: Method and results of general relativistic magnetohydrodynamic simulations in kerr space-time. *Phys. Rev. D*, 67:104010, 2003.

[81] S. Koide, D. L. Meier, Shibata K., and Kudoh T. General relativistic simulations of early jet formation in a rapidly rotating black hole magnetosphere. *Astrophys J.*, 536:668–674, 2000.

[82] S. Koide, K. Shibata, and T. Kudoh. Relativistic jet formation from black hole magnetized accretion disks: Method, tests, and applications of a general relativistic-magnetohydrodynamic numerical code. *Astrophys J.*, 522:727–752, 1999.

[83] S. Koide, K. Shibata, T. Kudoh, and D. L. Meier. Extraction of black hole rotational energy by a magnetic field and the formation of relativistic jets. *Science*, 295:1688–1691, 2002.

[84] S. S. Komissarov. A godunov-type scheme for relativistic magnetohydrodynamics. *MNRAS*, 303:343–366, 1999.

[85] S. S. Komissarov. Limit shocks of relativistic magnetohydrodynamics. *MNRAS*, 341:717, 2003.

[86] S. S. Komissarov. General relativistic magnetohydrodynamic simulations of monopole magnetospheres of black holes. *MNRAS*, 350:1431–1436, 2004.

[87] K. Kotake, S. Yamada, K. Sato, K. Sumiyoshi, H. Ono, and H. Suzuki. Gravitational radiation from rotational core collapse: Effects of magnetic fields and realistic equations of state. *Phys. Rev. D*, 69:124004, 2004.

[88] H.-O. Kreiss and J. Oliger. Methods for the approximate solution of time dependent problems. *GARP Pub. Series*, 10, 1973.

[89] C. B. Laney. *Computational Gasdynamics.* Cambridge University Press, 1998.

[90] P. D. Lax and B. Wendroff. Systems of conservation laws. *Comm. Pure Appl. Math.*, 13:217–237, 1960.

[91] G. Leiler and L. Rezzolla. Iterated crank-nicolson method for hyperbolic and parabolic equations in numerical relativity. *Phys. Rev. D*, 73:044001, 2006.

[92] T. Leismann, L. Antón, M. A. Aloy, E. Müller, J. M. Martí, J. A. Miralles, and J. M. Ibáñez. Relativistic MHD simulations of extragalactic jets. *A&A*, 436:503–526, 2005.

[93] R. J. LeVeque. *Numerical Methods for Conservation Laws.* Birkhäuser-Verlag, 1992.

[94] R. J. Leveque. *Computational Methods for Astrophysical Fluid Flow.* Springer-Verlag, 1998.

[95] A. Lichnerowicz. *Relativistic Hydrodynamics and Magnetohydrodynamics.* W. A. Benjamin INC, 1967.

[96] `LIGO`. `http://www.ligo.caltech.edu/`.

[97] `LISA`. `http://lisa.jpl.nasa.gov/`.

[98] F. Löffler, L. Rezzolla, and M. Ansorg. Numerical evolutions of a black hole-neutron star system in full General Relativity. 2006.

[99] J. M. Martí, J. M. Ibánez, and J. A. Miralles. Numerical relativistic hydrodynamics: local characteristic approach. *Phys. Rev. D*, 43:3794, 1991.

[100] J. M. Martí and E. Müller. The analytical solution of the riemann problem in relativistic hydrodynamics. *J. Fluid. Mech.*, 258:317, 1994.

[101] M. M. May and R. H. White. Hydrodynamic calculations of general relativistic collapse. *Phys. Rev. D*, 141:1232–1241, 1966.

[102] G. Mendell. Magnetic effects on the viscous boundary layer damping of the r-modes in neutron stars. *Phys. Rev. D*, 64:044009, 2001.

[103] P. Mészáros. Gamma-ray bursts. *Reports on Progress in Physics*, 69:2259–2321, 2006.

[104] F. C. Michel. Accretion of matter by condensed objects. *Astrophys. Spa. Sci.*, 15:153, 1972.

[105] A. Mignone and G. Bodo. An hllc solver for relativistic flows – ii. magnetohydrodynamics. *MNRAS*, 368:1040–1054, 2006.

[106] C. W. Misner, K. S. Thorne, and J. A. Wheeler. *Gravitation.* W. H. Freeman, San Francisco, 1973.

[107] Y. Mizuno, S. Yamada, S. Koide, and K. Shibata. General relativistic magnetohydrodynamic simulations of collapsars: Rotating black hole cases. *Astrophys. J.*, 606:395, 2004.

[108] V. Moncrief. Gravitational perturbations of spherically symmetric systems. i. the exterior problem. *Annals of Physics*, 88:323–342, 1974.

[109] R. S. Myong and P. L. Roe. Shock waves and rarefaction waves in magnetohydrodynamics. part 1. a model system. *J. Plasma Phys.*, 58:485, 1997.

[110] R. S. Myong and P. L. Roe. Shock waves and rarefaction waves in magnetohydrodynamics. part 2. the mhd system. *J. Plasma Phys.*, 58:521, 1997.

[111] A. Nagar and L. Rezzolla. TOPICAL REVIEW: Gauge-invariant non-spherical metric perturbations of Schwarzschild black-hole spacetimes. *Classical and Quantum Gravity*, 22:167, 2005.

[112] A. Nagar and L. Rezzolla. Corrigendum: Gauge-invariant non-spherical metric perturbations of Schwarzschild black-hole spacetimes. *Classical and Quantum Gravity*, 23:4297, 2006.

[113] G. Nagy, O. E. Ortiz, and O. A. Reula. Strongly hyperbolic second order einstein's evolution equations. *Phys. Rev. D*, 70:044012, 2004.

[114] T. Nakamura, K.-I. Oohara, and Y. Kojima. General relativistic collapse to black holes and gravitational waves from black holes. *Prog. Theor. Phys. Suppl.*, 90:1–218, 1987.

[115] S. C. Noble, C. F. Gammie, J. C. McKinney, and L. Del Zanna. Primitive variable solvers for conservative general relativistic magnetohydrodynamics. *Astrophys. J.*, 641:626–637, 2006.

[116] J. A. Pons, J. M. Martí, and E. Müller. The exact solution of the riemann problem with non-zero tangential velocities in relativistic hydrodynamics. *J. Fluid. Mech.*, 422:125, 2000.

[117] S. F. Portegies Zwart and H. N. Spreeuw. The galactic merger-rate of (ns, ns) binaries. I. Perspective for gravity-wave detectors. *A&A*, 312:670–674, 1996.

[118] W. H. Press, S. A. Teukolsky, W. T. Vetterling, B. P. Flannery, and M. Metcalf. *Numerical Recipes in Fortran 90.* Cambridge University Press, 2nd edition, 2002.

[119] L. Rezzolla, F. K. Lamb, D. Marković, and S. L. Shapiro. Properties of r modes in rotating magnetic neutron stars. I. Kinematic secular effects and magnetic evolution equations. *Phys. Rev. D*, 64:104013, 2001.

[120] L. Rezzolla, F. K. Lamb, D. Marković, and S. L. Shapiro. Properties of r modes in rotating magnetic neutron stars. II. Evolution of the r modes and stellar magnetic field. *Phys. Rev. D*, 64:104014, 2001.

[121] L. Rezzolla, F. K. Lamb, and S. L. Shapiro. R-Mode Oscillations in Rotating Magnetic Neutron Stars. *Astrophys. J.*, 531:L139–L142, 2000.

[122] L. Rezzolla and O. Zanotti. An improved exact riemann solver for relativistic hydrodynamics. *J. Fluid. Mech.*, 449:395, 2001.

[123] L. Rezzolla, O. Zanotti, and J. A. Pons. An improved exact riemann solver for multidimensional relativistic flows. *J. Fluid. Mech.*, 479:199, 2003.

[124] R. D. Richtmyer and K. W. Morton. *Difference Methods for Initial Value Problems.* Interscience Publishers, New York, 1967.

[125] R. Romero, J. M. Martí, J. A. Pons, J. M$^{\underline{a}}$. Ibáñez, and J. A. Miralles. The exact solution of the riemann problem in relativistic mhd with tangential magnetic fields. *J. Fluid. Mech.*, 544:323, 2005.

[126] M. E. Rupright, A. M. Abrahams, and L. Rezzolla. Cauchy-perturbative matching and outer boundary conditions: Methods and tests. *Phys. Rev. D*, 58:044005, 1998.

[127] D. Ryu and T. W. Jones. Numerical magnetohydrodynamics in astrophysics: Algorithm and tests for one-dimensional flow. *Astrophys. J.*, 442:228, 1995.

[128] O. Sarbach, G. Calabrese, J. Pullin, and M. Tiglio. Hyperbolicity of the BSSN system of Einstein evolution equations. *Phys. Rev. D*, 66:064002, 2002.

[129] M. Shibata, M. D. Duez, Y. T. Liu, S. L. Shapiro, and B. C. Stephens. Magnetized Hypermassive Neutron-Star Collapse: A Central Engine for Short Gamma-Ray Bursts. *Physical Review Letters*, 96:031102, 2006.

[130] M. Shibata and T. Nakamura. Evolution of 3-dimensional gravitational-waves - harmonic slicing case. *Phys. Rev. D*, 52:5428, 1995.

[131] M. Shibata and Y. Sekiguchi. Magnetohydrodynamics in full general relativity: Formulation and tests. *Phys. Rev. D*, 72:044014, 2005.

[132] M. Shibata and Y. Sekiguchi. Three-dimensional simulations of stellar core collapse in full general relativity: Nonaxisymmetric dynamical instabilities. *Phys. Rev. D*, 71:024014, 2005.

[133] M. Shibata, K. Taniguchi, and K. Uryū. Merger of binary neutron stars of unequal mass in full general relativity. *Phys. Rev. D*, 68:084020, 2003.

[134] M. Shibata, K. Taniguchi, and K. Uryū. Merger of binary neutron stars with realistic equations of state in full general relativity. *Phys. Rev. D*, 71:084021, 2005.

[135] M. Shibata and K. ō. Uryū. Simulation of merging binary neutron stars in full general relativity: Γ=2 case. *Phys. Rev. D*, 61:064001, 2000.

[136] L. Smarr and J. York. Kinematical conditions in the construction of spacetime. *Phys. Rev. D*, 17:2529, 1978.

[137] H. Sotani, K. D. Kokkotas, and N. Stergioulas. Torsional Oscillations of Relativistic Stars with Dipole Magnetic Fields. *astro-ph/0608626*, 2006.

[138] K. Z. Stanek, T. Matheson, P. M. Garnavich, P. Martini, P. Berlind, N. Caldwell, P. Challis, W. R. Brown, R. Schild, K. Krisciunas, M. L. Calkins, J. C. Lee, N. Hathi, R. A. Jansen, R. Windhorst, L. Echevarria, D. J. Eisenstein, B. Pindor, E. W. Olszewski, P. Harding, S. T. Holland, and D. Bersier. Spectroscopic Discovery of the Supernova 2003dh Associated with GRB 030329. *Astrophys. J.*, 591:L17–L20, 2003.

[139] `TAMA300`. `http://tamago.mtk.nao.ac.jp/`.

[140] J. H. Taylor. Binary pulsars and relativistic gravity. *Rev. Mod. Phys.*, 66:711, 1994.

[141] S. A. Teukolsky. Stability of the iterated crank-nicholson method in numerical relativity. *Phys. Rev. D*, 61:087501, 2000.

[142] J. Thornburg. A fast apparent-horizon finder for 3-dimensional Cartesian grids in numerical relativity. *Classical and Quantum Gravity*, 21(2):743–766, 2004.

[143] E. F. Toro. *Riemann Solvers and Numerical Methods for Fluid Dynamics.* Springer-Verlag, 1999.

[144] M. Torrilhon. Non-uniform convergence of finite volume schemes for riemann problems of ideal magnetohydrodynamics. *J. Comput. Phys.*, 192:73, 2003.

[145] M. Torrilhon. Uniqueness conditions for riemann problems of ideal magnetohydrodynamics. *J. Plasma Physics*, 69:253, 2003.

[146] M. Torrilhon and D. S. Balsara. High order weno schemes: investigations on non-uniform convergence for mhd riemann problems. *J. Comput. Phys.*, 201:586, 2004.

[147] G. Tóth. The $\nabla \cdot b = 0$ constraint in shock-capturing magnetohydrodynamics codes. *J. Comp. Phys.*, 161:605–652, 2000.

[148] J. K. Truelove, R. I. Klein, C. F. McKee, J. H. Holliman, II, L. H. Howell, and J. A. Greenough. The Jeans Condition: A New Constraint on Spatial Resolution in Simulations of Isothermal Self-gravitational Hydrodynamics. *Astrophys. J.*, 489:L179, 1997.

[149] M. H. van Putten, A. Levinson, H. K. Lee, T. Regimbau, M. Punturo, and G. M. Harry. Gravitational radiation from gamma-ray burst-supernovae as observational opportunities for LIGO and VIRGO. *Phys. Rev. D*, 69:044007, 2004.

[150] M. H. P. M. Van Putten. A numerical implementation of mhd in divergence form. *J. Comp. Phys.*, 105:339, 1993.

[151] `VIRGO`. `http://www.virgo.infn.it/`.

[152] R. Voss and T. M. Tauris. Galactic distribution of merging neutron stars and black holes - prospects for short gamma-ray burst progenitors and LIGO/VIRGO. *MNRAS*, 342:1169–1184, 2003.

[153] C. M. Will. *Theory and experiment in gravitational physics.* Cambridge University Press, Cambridge, 1993. revised edition.

[154] C. M. Will. The confrontation between general relativity and experiment. *Living Rev. Relativity*, 9(3), 2006. URL (cited on August 3rd 2006): http://www.livingreviews.org/lrr-2006-3.

[155] J. R. Wilson. Numerical study of fluid flow in a kerr space. *Astrophys. J.*, 173:431, 1972.

[156] J. R. Wilson. Some magnetic effects in stellar collapse and accretion. *Ann. New York Acad. Sci.*, 262:123, 1975.

[157] J. R. Wilson. A numerical method for relativistic hydrodynamics. In L. L. Smarr, editor, *Sources of Gravitational Radiation*, pages 423–445. Cambridge University Press, 1979.

[158] K. S. Yee. Numerical solution of inital boundary value problems involving maxwell's equations in isotropic media. *IEEE Trans. Antenna Propagation*, AP-14:302–307, 1966.

[159] H.-J. Yo, T. W. Baumgarte, and S. Shapiro. Improved numerical stability of stationary black hole evolution calculations. *Phys. Rev. D*, 66:084026, 2002.

[160] M. Yokosawa. Energy and angular momentum transport in magnetohydrodynamical accretion onto a rotating black hole. *Publ. Astron. Soc. Japan*, 45:207–218, 1993.

[161] M. Yokosawa. Structure and Dynamics of an Accretion Disk around a Black Hole. *Publ. Astron. Soc. Japan*, 47:605–615, 1995.

[162] J. W. York. Kinematics and dynamics of general relativity. In Larry L. Smarr, editor, *Sources of Gravitational Radiation*, page 83. Cambridge University Press, Cambridge, UK, 1979.

[163] O. Zanotti, L. Rezzolla, and J. A. Font. Quasi-periodic accretion and gravitational waves from oscillating "toroidal neutron stars". *MNRAS*, 341:832, 2003.

Appendix A

We here report the expressions of the tangential components of the velocity behind the shock (*i.e.* v_b^y, v_b^z) when expressed as function of post-shock p and J. Firstly, we consider v_b^y as function of p_b, J and v_b^z.

$$
\begin{aligned}
v_b^y \;=\; & -\frac{1}{N_y}\Big\{J^3 W_a^4\Big[v_a^y(D_a + p_a + \tau_a - \eta_a^2 W_a^2)(D_a + p_b + \tau_a - B_x^2 - \eta_a^2 W_a^2) + \\
& B_a^y\Big(B_x(p_a + \tau_a)v_a^x + B_a^z(p_b + \tau_a)v_b^z - \eta_a(p_b + \tau_a) - \\
& D_a(\eta_a - B_x v_a^x - B_a^z v_b^z) + \eta_a^3 W_a^2 - \eta_a^2(B_x v_a^x + B_a^z v_b^z)W_a^2\Big)\Big] - \\
& J^2 D_a W_a^2\Big[\Big(2B_x^3\eta_a v_a^y + B_x^2 v_a^x[(D_a + p_a + \tau_a)v_a^y - 2B_a^y\eta_a] + \\
& v_a^x(p_a - p_b)[2(D_a + p_a + \tau_a)v_a^y + B_a^y(B_a^z v_b^z - 2\eta_a)] - B_x\{\eta_a(3D_a + 2p_a + p_b + 3\tau_a)v_a^y - \\
& B_a^z(p_a - p_b)v_a^y v_b^z + B_a^y[(p_a + \tau_a)(v_a^{x\,2} - 1) - 3\eta_a^2 + 2B_a^z\eta_a v_b^z + (p_b + \tau_a)v_a^z v_b^z - MD_a]\}\Big)W_a^2 - \\
& B_x B_a^y(D_a + p_b + \tau_a) + \eta_a^2[2(p_b - p_a)v_a^x v_a^y - B_x^2 v_a^x v_a^y + B_x(3\eta_a v_a^y - MB_a^y)]W_a^4\Big]W_s - \\
& JD_a^2 W_a^2\Big[B_x^3 v_a^x(B_a^y + 2\eta_a v_a^y W_a^2) - B_x^4 v_a^y + \\
& B_x v_a^x(p_a - p_b)[2B_a^y + (2\eta_a v_a^y + B_a^z v_a^y v_b^z + B_a^y v_a^z v_b^z)W_a^2] + \\
& Q[(D_a + p_a + \tau_a)v_a^y - \eta_a(B_a^y + \eta_a v_a^y W_a^2)] + \\
& B_x^2\Big(B_a^y(B_a^z v_b^z - 3\eta_a + 2M\eta_a W_a^2) + v_a^y[D_a + p_a + \tau_a - (3\eta_a^2 + (p_b - p_a)v_a^z v_b^z)W_a^2]\Big)\Big]W_s^2 + \\
& B_x D_a^3\Big(B_x^3 v_a^x v_a^y W_a^2 - B_x(p_a - p_b)v_a^x v_a^y v_a^z v_b^z W_a^4 - Q(B_a^y + \eta_a v_a^y W_a^2) - \\
& B_x^2[B_a^y + (\eta_a v_a^y - MB_a^y)W_a^2]\Big)W_s^3\Big\}\;,
\end{aligned}
$$

where we have defined $M \equiv (1 - v_a^{x2} - v_a^z v_b^z)$, $Q \equiv W_a^2(p_a - p_b)(v_a^{x2} - 1)$ and

$$
\begin{aligned}
N_y \equiv\ & W_a^2\Big\{B_x D_a W_a^2 W_s\Big(J^2[2B_a^{y2}\eta_a - \\
& 3\eta_a(D_a + p_b + \tau_a) + 3\eta_a^3 W_a^2 + B_a^y v_a^y(D_a - p_a + 2p_b + \tau_a - \eta_a^2 W_a^2)] + \\
& 2D_a J(p_a - p_b)v_a^x(2\eta_a - B_a^y v_a^y)W_s + D_a^2\eta_a(p_a - p_b)(v_a^{x2} - 1)W_s^2\Big) - \\
& B_x^4 D_a^2 W_s^2(J + D_a v_a^x W_s) - W_a^2[J(D_a + p_b + \tau_a - \eta_a^2 W_a^2) + \\
& D_a(p_b - p_a)v_a^x W_s][J^2(D_a + p_b + \tau_a - \eta_a^2 W_a^2) + 2D_a J(p_b - p_a)v_a^x W_s - \\
& B_a^{y2}J^2 + D_a^2(p_b - p_a)(v_a^{x2} - 1)W_s^2] + B_x^3 D_a W_s[2\eta_a J^2 W_a^2 + \\
& 2D_a\eta_a J v_a^x W_a^2 W_s + D_a^2(\eta_a - B_a^y v_a^y)W_s^2] + B_x^2\Big[J^3 W_a^2(D_a + p_b + \tau_a - \eta_a^2 W_a^2) + \\
& D_a J^2 v_a^x W_a^2(D_a - 2p_a + 3p_b + \tau_a - \eta_a^2 W_a^2)W_s + \\
& D_a^2 J\Big(D_a + p_b - B_a^{y2} + \tau_a + [2B_a^y\eta_a v_a^y - 3\eta_a^2 - (p_a - p_b)(3v_a^{x2} - 1 + v_a^{y2})]W_a^2\Big)W_s^2 - \\
& D_a^3 v_a^x v_a^{z2} W_a^2(p_b - p_a)W_s^3\Big]\Big\}\ .
\end{aligned}
$$

We next consider the expression of v_b^z as function of post-shock p and J

$$
\begin{aligned}
v_b^z =\ & -\frac{1}{N_z}\Big\{J^3 W_a^4\Big[v_a^z(D_a + p_a + \tau_a - \eta_a^2 W_a^2)(D_a - B^{x2} - B_a^{y2} + \\
& p_b + \tau_a - \eta_a^2 W_a^2) + B_a^z\Big((p_a + \tau_a)(B^x v_a^x + B_a^y v_a^y) - \eta_a(p_b + \tau_a) + \\
& D_a(B^x v_a^x + B_a^y v_a^y - \eta_a) + \eta_a^3 W_a^2 - \eta_a^2(B^x v_a^x + B_a^y v_a^y)W_a^2\Big)\Big] + \\
& D_a J^2 W_a^2\Big[B^x B_a^z(D_a + p_b + \tau_a) + \Big(B^x B_a^z[2B_a^y\eta_a v_a^y - 3\eta_a^2 + \\
& D_a(v_a^{x2} + v_a^{y2} - 1) + (p_a + \tau_a)(v_a^{x2} + v_a^{y2} - 1)] - \\
& 2B^{x3}\eta_a v_a^z - B^x[2B_a^{y2}\eta_a - \eta_a(3D_a + 2p_a + p_b + 3\tau_a) + \\
& B_a^y(D_a + p_a + \tau_a)v_a^y]v_a^z - B^{x2}v_a^x[(D_a + p_a + \tau_a)v_a^z - 2B_a^z\eta_a] - \\
& 2(p_a - p_b)v_a^x[(D_a + p_a + \tau_a)v_a^z - B_a^z\eta_a]\Big)W_a^2 + \\
& \eta_a^2\Big(B^x B_a^z(v_a^{x2} + v_a^{y2} - 1) - (B^{x2}v_a^x - 3B^x\eta_a + 2p_a v_a^x - 2p_b v_a^x + B^x B_a^y v_a^y)v_a^z\Big)W_a^4\Big]W_s - \\
& D_a^2 J W_a^2\Big(2B^x(p_a - p_b)v_a^x(B_a^z + \eta_a v_a^z W_a^2) - B^{x4}v_a^z + B^{x3}v_a^x(B_a^z + 2\eta_a v_a^z W_a^2) + \\
& B^{x2}\{v_a^z[D_a - B_a^{y2} + p_a + \tau_a - \eta_a(3\eta_a - 2B_a^y v_a^y)W_a^2] + \\
& B_a^z[B_a^y v_a^y - 3\eta_a - 2\eta_a(v_a^{x2} + v_a^{y2} - 1)W_a^2]\} + \\
& (p_a - p_b)(v_a^{x2} - 1)W_a^2[(D_a + p_a + \tau_a)v_a^z - \eta_a(B_a^z + \eta_a v_a^z W_a^2)]\Big)W_s^2 + \\
& B^x D_a^3\Big[B_x^3 v_a^x v_a^z W_a^2 - (p_a - p_b)(v_a^{x2} - 1)W_a^2(B_a^z + \eta_a v_a^z W_a^2) - \\
& B_x^2\Big(B_a^z + [B_a^z(v_a^{x2} + v_a^{y2} - 1) + (\eta_a - B_a^y v_a^y)v_a^z]W_a^2\Big)\Big]W_s^3\Big\}\ ,
\end{aligned}
$$

where

$$
\begin{aligned}
N_z \equiv\; & W_a^2 \Big\{ B^x D_a W_a^2 W_s \{ J^2 [2B_a^{y2}\eta_a + 2B_a^{z2}\eta_a - 3\eta_a(D_a + p_b + \tau_a) + 3\eta_a^3 W_a^2 + \\
& B_a^y v_a^y (D_a - p_a + 2p_b + \tau_a - \eta_a^2 W_a^2) + B_a^z v_a^z (D_a - p_a + 2p_b + \tau_a - \eta_a^2 W_a^2)] + \\
& 2D_a J (p_a - p_b) v_a^x (2\eta_a - B_a^y v_a^y - B_a^z v_a^z) W_s + D_a^2 \eta_a (p_a - p_b)(v_a^{x2} - 1) W_s^2 \} - \\
& B_x^4 D_a^2 W_s^2 (J + D_a v_a^x W_s) - W_a^2 [J(D_a + p_b + \tau_a - \eta_a^2 W_a^2) - \\
& D_a (p_a - p_b) v_a^x W_s][J^2 (D_a - B_a^{y2} - B_a^{z2} + p_b + \tau_a - \eta_a^2 W_a^2) - \\
& 2D_a J (p_a - p_b) v_a^x W_s - D_a^2 (p_a - p_b)(v_a^{x2} - 1) W_s^2] + \\
& B_x^3 D_a W_s [2\eta_a J^2 W_a^2 + 2D_a \eta_a J v_a^x W_a^2 W_s + D_a^2 (\eta_a - B_a^y v_a^y - B_a^z v_a^z) W_s^2] + \\
& B_x^2 \Big(J^3 W_a^2 (D_a + p_b + \tau_a - \eta_a^2 W_a^2) + D_a J^2 v_a^x W_a^2 (D_a - 2p_a + 3p_b + \tau_a - \eta_a^2 W_a^2) W_s + \\
& D_a^2 J \{ D_a - B_a^{y2} - B_a^{z2} + p_b + \tau_a + [2\eta_a (B_a^y v_a^y + B_a^z v_a^z) - 3\eta_a^2 - \\
& (p_a - p_b)(3v_a^{x2} + v_a^{y2} + v_a^{z2} - 1)] W_a^2 \} W_s^2 \Big) \Big\} \; .
\end{aligned}
$$

Appendix B

The explicit form for the system of ODEs to be solved numerically to determine the solution across a rarefaction wave within the p-method is given by the following set of equations in which the total pressure p plays the role of the self-similar variable

$$\frac{\mathrm{d}\rho}{\mathrm{d}p} = -\rho\left(W^2 v_x + \frac{1}{v_x - \xi}\right)\frac{\mathrm{d}v_x}{\mathrm{d}p} - \rho W^2 v_y \frac{\mathrm{d}v_y}{\mathrm{d}p} - \rho W^2 v_z \frac{\mathrm{d}v_z}{\mathrm{d}p}\ , \tag{B.1}$$

$$\begin{aligned}\frac{\mathrm{d}v_x}{\mathrm{d}p} = {} & R\Big\{(\rho h_g W^2 + B_x^2)(\xi - v_x)(v_x\xi - 1) + B_x^2\frac{\xi v_x - 1}{W^2(v_x - \xi)} + B_x^2\xi(v_y^2 + v_z^2) + \\ & B_x[\eta(\xi^2 - 1) - B_x v_x(1 - 2v_x\xi + \xi^2)]\Big\}\ ,\end{aligned} \tag{B.2}$$

$$\begin{aligned}\frac{\mathrm{d}v_y}{\mathrm{d}p} = {} & R\Bigg\{2B_x v_y(\eta - B_z v_z)\xi - B_x^2 v_y\xi(\xi + v_x) + \\ & v_y[B_z^2 + W^2(\eta^2 - w)](v_x - \xi)\xi + B_y^2 v_y(v_x\xi - 1) + B_y B_z v_z(\xi^2 - 1) + \\ & B_x B_y\frac{(v_y^2 + v_z^2 - 1) + (v_x - 2v_x v_y^2)\xi + (1 + v_y^2 - v_z^2)\xi^2 - v_x\xi^3}{(v_x - \xi)}\Bigg\}\ ,\end{aligned} \tag{B.3}$$

$$\begin{aligned}\frac{\mathrm{d}v_z}{\mathrm{d}p} = {} & R\Bigg\{2B_x(\eta - B_y v_y)v_z\xi - B_x^2 v_z\xi(v_x + \xi) + \\ & v_z[B_y^2 + W^2(\eta^2 - w)](v_x - \xi)\xi + B_y B_z v_y(\xi^2 - 1) + v_z B_z^2(v_x\xi - 1) + \\ & B_x B_z\frac{(v_y^2 + v_z^2 - 1) + (v_x - 2v_x v_z^2)\xi + (1 - v_y^2 + v_z^2)\xi^2 - v_x\xi^3}{(v_x - \xi)}\Bigg\}\ ,\end{aligned} \tag{B.4}$$

$$\frac{\mathrm{d}B_y}{\mathrm{d}p} = -\frac{W^2(B_y - B_y v_x\xi + B_x v_y\xi)}{B_x^2 + 2B_x\eta W^2(v_x - \xi) + W^4(\eta^2 - w)(v_x - \xi)^2}\ , \tag{B.5}$$

$$\frac{\mathrm{d}B_z}{\mathrm{d}p} = -\frac{W^2(B_z - B_z v_x\xi + B_x v_z\xi)}{B_x^2 + 2B_x\eta W^2(v_x - \xi) + W^4(\eta^2 - w)(v_x - \xi)^2}\ , \tag{B.6}$$

where we have defined

$$R \equiv \frac{1}{\rho h_g W^4(\eta^2 - w)(V_A^+ - \xi)(V_A^- - \xi)}\ , \tag{B.7}$$

with

$$V_A^{\pm} \equiv v_x + \frac{B_x}{W^2(\eta \pm \sqrt{w})} \ , \tag{B.8}$$

being the Alfvèn velocities in the two directions. Note that the set of ODEs has a singular point if the characteristic velocity of the slow or fast magnetosonic waves is equal to the Alfv́en velocity [*cf.* eq. (B.7)] and cannot be solved in this case without a proper regularization. This procedure is not included in the numerical code made available upon request.